

The logo of the University of Twente, featuring a stylized yellow and black geometric shape resembling a flower or a cluster of cells, with a grey line drawing of a pen nib pointing towards it.

UNIVERSITY OF TWENTE.

Department of Thermal and Fluid Engineering

Atmospheric sound propagation modeling with the Harmonoise model applied to wind turbine noise

Lennart Bouma
Master Thesis
02-2023

Supervisors:

Andrea Bresciani
Marijn Sanders
Leandro de Santana

Graduation number:

422

Preface

In front of you lies the thesis titled “Atmospheric sound propagation modeling with the Harmonoise model applied to wind turbine noise.” This thesis is written to fulfill the requirements of graduating the master Mechanical Engineering at the University of Twente.

This work explores the field of atmospheric acoustics, which is a branch in the field of acoustics that describes the transport of sound through the atmosphere. The fundamentals of atmospheric acoustics will be presented, with a focus on applying them to wind turbine noise.

My first spark of interest in acoustics was lit in the course on aeroacoustics, where the fundamentals of sound generation in aircraft were taught. After that, I chose to do my internship at Apollo to study the noise that car tires make. For me, this made me realize the impact of noise on people in the current world. Therefore, it was a no-brainer for me to apply for this master’s assignment about wind turbine noise.

The process has been fun for me. I did not know much about atmospheric acoustics and learned a great deal. It was interesting to me how fluid a master’s assignment can be. First, my focus was on studying and improving the Harmonoise model, but quickly the assignment shifted to applying the model to wind turbine noise. Overall, I am happy with the end result and was very content with all the guidance and nice discussions that I encountered.

First of all, I would like to thank my supervisor, Andrea Bresciani. Throughout the process of researching and writing this thesis, I felt free to explore all of my interests while knowing that I could always rely on his guidance to steer me in the right direction.

Secondly, I would like to thank Marijn Sanders and Leandro de Santana. Both of them are my supervisors from the University of Twente. Leandro de Santana helped me with the first half of my thesis and helped me explore some interesting acoustic concepts. Marijn Sanders helped me in the final and very important stage of my thesis, where I had to complete my work.

Finally, I would like to thank all my family and friends who had to listen to fun facts about acoustics for more than half a year. If I got stuck in a part of the process, I could always count on mental support and a different perspective.

I would also like to thank you, the reader. I wish you happy reading!

Lennart Bouma

Enschede, January 2023

Summary

The wind power industry is rapidly growing worldwide, thereby reducing our reliance on fossil fuels. However, as the number of wind turbines increases, so too does noise pollution. This causes annoyance and even health problems for residents living near a wind turbine or wind farm. Accurate wind turbine noise prediction methods are needed to minimize the amount of noise pollution by carefully considering the placement of wind turbines in the environment. However, wind turbine noise prediction is a complex task. This is mainly because of the noise propagation through the atmosphere and terrain, which is a time-dependent process with multiple mechanisms that can influence noise levels. Although physically accurate numerical models exist, they often require unfeasibly large computational times. To overcome this problem, analytical models with lower computational time but also lower accuracy are often used. One of these models is the Harmonoise model.

In this work, the Harmonoise model is evaluated for its use in predicting wind turbine noise propagation. The evaluation focuses on the influence of wind shear and temperature profiles in the atmospheric boundary layer on wind turbine noise propagation. The wind shear and temperature profiles influence the local sound speed, which leads to bending, i.e. refraction of the sound waves. Most analytical noise prediction models cannot accurately incorporate this effect.

Results from the Harmonoise model are compared to results generated by a numerical model for several benchmark cases. The numerical model solves the parabolic equation and is widely used in atmospheric acoustics. The Harmonoise model is then coupled with a semi-analytical wind turbine noise prediction model to simulate realistic noise levels around a single wind turbine under different atmospheric conditions. Noise maps around a wind turbine are then generated. These noise maps provide a representation of the noise pollution around a wind turbine for a certain set of conditions.

It was found that the Harmonoise model can accurately predict noise propagation if the sound speed in the atmosphere varies linearly with height. However, the Harmonoise results are less accurate if a logarithmic sound speed profile is present. The overall noise levels around a wind turbine were found to be negligibly influenced by the simulated atmospheric conditions for propagation distances up to a distance of 1500 meters from the turbine. However, the spectral noise levels were found to be strongly affected.

Additionally, a method is proposed to include horizontal sonic gradients with the Harmonoise model. It was found that improved accuracy for such cases is possible but the test cases were limited. Therefore, additional research on this concept is required.

Contents

Preface	2
Summary	4
1 Introduction	15
2 Basic acoustics	17
2.1 What is sound?	17
2.2 The wave equation	18
2.3 Speed of sound	18
2.3.1 Effective sound speed approximation	18
2.4 Sound pressure level	19
2.5 Sound velocity, -intensity, -power and -power level	19
2.5.1 Sound velocity	20
2.5.2 Sound intensity	20
2.5.3 Sound power	20
2.5.4 Sound power level	20
2.6 Point sources	20
2.6.1 Sound velocity of a point source	21
2.6.2 Sound intensity for harmonic point source	21
2.6.3 Sound pressure level for a harmonic point source	21
2.7 Non harmonic sources & Octave bands	22
2.7.1 Sound pressure level for a non harmonic point source	23
2.8 Free field pressure	23
3 Atmospheric sound propagation	25
3.1 Attenuation mechanics	25
3.1.1 Geometrical spreading	25
3.1.2 Atmospheric absorption	26
3.1.3 Reflection	26
3.1.4 Refraction	29
3.1.5 Diffraction	31
3.1.6 Turbulence	31
3.2 Models to calculate the sound propagation	32
3.2.1 Ray tracing	32
3.2.2 Parabolic equation method	33
3.2.3 Engineering models	34
4 The Harmonoise model	35
4.1 Geometrical spreading & Atmospheric absorption	35
4.2 Ground reflections	36
4.2.1 Ground segments	36
4.3 Concave model	38
4.3.1 Flat and deep-valley ground attenuation	39
4.3.2 Fresnel weights	40
4.3.3 Transition frequency	41

4.3.4	Coherence factor	42
4.4	Refraction	43
4.4.1	Curved ground analogy	43
4.4.2	Conformal mapping in the Harmonoise model	44
4.4.3	Linearization	45
4.5	Assumptions used in the Harmonoise model	46
5	Matlab implementation and validation	49
5.1	Validation	50
5.1.1	Validation of Matlab implementation	51
5.1.2	Evaluating the accuracy of ATMOS	51
5.1.3	Validation for low sources	53
5.1.4	Verification for high sources	57
5.2	The Harmonoise model for wind turbine noise	60
6	Wind turbine simulation	63
6.1	Source simulation	63
6.2	Test case	64
6.3	Source simulation results	65
6.4	Results	69
6.4.1	2D case	69
6.4.2	3D Case	69
7	Analyzing horizontal gradients with the Harmonoise model	77
7.1	Relevance of horizontal sonic gradients	77
7.2	Proposed method	77
7.3	Implementation	78
7.4	Results	80
	Bibliography	92
A	Atmospheric absorption	93
B	Analytical solution in a homogeneous atmosphere above a fully reflecting plane	95
C	Sound speed profiles in the atmosphere	97
C.1	Surface layer	97
C.2	Similarity theory	98
D	Ray paths	101
D.1	Tracing ray paths in a layered atmosphere	101
E	Parabolic equation method	103
E.1	Derivation of the narrow angle parabolic equation	103
E.2	What is a parabolic equation?	103
E.3	General approach of the parabolic equation method	104
E.3.1	Advantages and limitations of the parabolic equation method	104
E.4	Green functions parabolic equation(GFPE)	104
E.5	ATMOS	105
E.5.1	Parameters	105
F	Conformal mapping	107

List of Figures

1.1	Possible scenario that will be simulated in this work.	16
2.1	The black straight lines represent areas of high pressure, while the red lines represent areas of low pressure. The high pressure line is equal to the atmospheric pressure (p_{atm}) plus the sound pressure (p). The low pressure line is equal to the atmospheric pressure (p_{atm}) minus the sound pressure (p).	17
2.2	Gain of the dBA filter for 20-20000 Hz.	19
3.1	Spherical spreading from a point source in free space. The circular lines represent outgoing acoustical waves.	25
3.2	Effect of atmospheric absorption on the sound pressure level with respect to frequency for an ambient atmospheric temperature of 293 Kelvin.	27
3.3	Point source over a reflecting surface, where the dotted circular line depicts the reflective part of a wave.	27
3.4	Image source method, the path length of the reflected ray path is $r_s + r_r$. In the figure is θ the elevation angle.	28
3.5	Reflection attenuation for different frequencies. The results are presented as the averaged 1/3 octave center frequencies.	29
3.6	Refraction in the case of a discontinuous medium. Below the interface, the speed of sound is equal to c_1 and above the interface to c_2	30
3.7	Several rays visualized from a source for a linear sound speed gradient. In the figure three receivers are shown that are affected by the refraction. The speed of sound profile is $c_0 + u$. The corresponding sound speed profiles are shown for upwind propagation and for downwind propagation.	30
3.8	Ray visualization of sound diffracting around a barrier.	31
3.9	Illustration of small scale refraction due to turbulence.	32
3.10	Ray tracing in an atmosphere with sound speed profile $c_{eff}(z) = 340 + \log\left(\frac{z}{0.1} + 1\right)$. In the figure, 100 rays are illustrated with shooting angles between 0 and 5 °, where the angle is the angle between the ray and the horizontal.	33
4.1	A source and receiver placed above a randomly generated ground profile.	36
4.2	Segmentation of the ground profile in case of two straight line segments.	37
4.3	Segmentation of the ground profile in case of 10 straight line segments.	37
4.4	Local coordinate system of a ground segment.	38
4.5	This figure shows the Fresnel ellipse with the parameters that are used in the formulation. Figure taken from [1].	41
4.6	a) Sound rays between source and receiver in case of a downward-refracting atmosphere. b) Curved ground analogy that represents situation a. The curvature of the ground is chosen as the limiting ray.	44
4.7	Conformal mapping in the case of a downward refracting atmosphere. The conformal mapping of equation 4.44 is used.	45
4.8	Geometry used for linearization of a logarithmic sound profile for high source and receiver. Note that the distance between source and receiver is significantly different than the distance between the intersections of the ray with the ground.	47

4.9	Visualization of the linearization of a lin-log effective sound speed profile with parameters $A = 0.0191$ 1/s , $B = 1.1260$ m/s, $c_0 = 340$ m/s. The heights of the source and receiver are 80 and 1.5 meter in case of a high source. In case of the low source the height of the source and receiver are both 1.5 meter.	47
5.1	Calculation scheme of the Harmonoise model.	49
5.2	Geometry for validation of the Harmonoise code. The blue line depicts the effective speed of the sound profile that varies only with height.	50
5.3	Ground attenuation of case A_1 calculated with the implemented Matlab Harmonoise code and with the CSTB in-house code. The results are presented in the 1/3 octave band spectrum.	51
5.4	Ground attenuation of case A_2 calculated with the implemented Matlab Harmonoise code and with the CSTB in-house code. The results are presented in the 1/3 octave band spectrum.	52
5.5	The difference for case A_1 between the Harmonoise code implemented in Matlab and the in-house Harmonoise code of the CSTB.	52
5.6	The difference for case A_2 between the Harmonoise code implemented in Matlab and the in-house Harmonoise code of the CSTB.	53
5.7	Results of ATMOS (a GFPE solver) for different grid spacings compared to an analytical solutions for case B_1	54
5.8	Results of ATMOS (a GFPE solver) for different grid spacings compared to an analytical solutions for case B_2	54
5.9	The difference between the analytical solution and ATMOS with different grid spacings for case B_1	55
5.10	The difference between the analytical solution and ATMOS with different grid spacings for case B_2	55
5.11	Ground attenuation of case C_1 calculated with ATMOS (a GFPE solver) and the Harmonoise model. This case illustrates the difference between ATMOS and Harmonoise. The results are presented in the 1/3 octave band spectrum.	56
5.12	The difference between the ground attenuation obtained with ATMOS and the Harmonoise model for case C_1	56
5.13	Ground attenuation of case C_2 calculated with ATMOS (a GFPE solver) and the Harmonoise model. This case is a reference to illustrate the difference between ATMOS and Harmonoise. The results are presented in the 1/3 octave band spectrum.	57
5.14	Ground attenuation of case C_3 calculated with ATMOS (a GFPE solver) and the Harmonoise model. This case illustrates the difference between ATMOS and Harmonoise. The results are presented in the 1/3 octave band spectrum.	58
5.15	The ground attenuation of case D_1 for several 1/3 octave band frequencies computed by the Harmonoise model and ATMOS.	59
5.16	The difference between ATMOS and the Harmonoise model of case D_1	59
5.17	The ground attenuation of case D_2 for several 1/3 octave band frequencies computed by the Harmonoise model and ATMOS.	60
5.18	The ground attenuation of case D_3 for several 1/3 octave band frequencies computed by the Harmonoise model and ATMOS.	61
6.1	Calculation procedure of calculating the sound pressure level around a wind turbine with a source model and the Harmonoise model.	64
6.2	Representation of the general 2D case that is used to simulate wind turbine noise of a single turbine.	64
6.3	Representation of the 3D case, where the sound levels will be calculated somewhere in the xy -plane for a given receiver height.	65
6.4	Temperature, velocity and effective sound speed profiles for a stable, unstable and neutral atmosphere. Generated with $U = 8$ m/s at 80 m, $z_0 = 0.1$ m, $T_s = 290$ K and Obukhovs lengths of 145,-86 and infinity respectively (see appendix C.2 for the definition of the Obukov length).	66
6.5	Polar plot of the SPL for the parameters in table 6.2, representing the horizontal and vertical directivity.	67
6.6	Directional source of 63 Hz represented by a sphere with a radius of 1 meter.	67

6.7	Directional source of 1 kHz represented by a sphere with a radius of 1 meter.	67
6.8	Directional source of the overall sound pressure level represented by a sphere with a radius of 1 meter.	68
6.9	Sound power level of points source used to calculated values at 1200 m downwind from the SWT 2.3-93 wind turbine for different atmospheric conditions. The location on the 1 meter radius sphere is described by $\theta = -0.0077$ and $\phi = 0$	68
6.10	Comparison of the Harmonoise model with the source model, free field results of the source model + 6 dBA and on-site measurements for the SWT 2.3-93 wind turbine are presented.	69
6.11	Sound pressure level of receiver 2. All the attenuation effects and the source power level are shown as well. The actual sound pressure level is calculated with $L_p = L_w + A_{div} + A_{gr} + A_{atm}$	70
6.12	Ray tracing for a linear sound speed profile with a gradient of -0.0337; 100 rays leave the source at angles ranging from $-\pi/9$ to 0 radians. The start of the shadow zone can be identified around 1500 meter.	70
6.13	Simulation grid for the sound pressure level around a wind turbine. All black dots can be considered receivers with a height of 1.5 meter above the ground plane. The red square indicates the area that is used for post-processing of the results.	71
6.14	Sound pressure level around a wind turbine for the center frequency of 63 Hz in case of a stable atmosphere.	72
6.15	Sound pressure level around a wind turbine for the center frequency of 1000 Hz in case of a stable atmosphere.	72
6.16	Overall sound pressure level around a wind turbine in case of a stable atmosphere.	73
6.17	Sound pressure level against distance for different azimuth angles for the center frequency of 1000 Hz.	74
6.18	The overall sound pressure level plotted against radial distance from the wind turbine for different azimuth angles.	75
7.1	Effective sound speed profile with $U_0 = 8$ m/s over a grain field ($z_0 = 0.4$ m) and still water ($z_0 = 0.0002$ m).	78
7.2	A ray path with a sound speed discontinuity at the interface ($x = 37.5$ m). The ray path for a constant gradient of 0.2 in the whole domain is shown by the red dotted line for comparison.	79
7.3	A flat ground curved with the curvature of the rays represented in figure 7.2.	79
7.4	Ground attenuation for case E_1 computed with the GFPE solver ATMOS and the Harmonoise model using a variable conformal mapping. As a reference result the average vertical sonic gradient solution (REF_B) computed by the Harmonoise model is included.	81
7.5	The difference of the Harmonoise model with a variable conformal mapping and the GFPE solution for case E_1 . Also the difference between the GFPE solution and the average vertical sonic gradient solution is shown.	81
7.6	Ground attenuation for case E_2 computed with the GFPE solver ATMOS and the Harmonoise model using a variable conformal mapping. As a reference result the average vertical sonic gradient solution (REF_B) computed by the Harmonoise model is included.	82
7.7	The difference of the Harmonoise model with a variable conformal mapping and the GFPE solution for case E_2 . Also the difference between the GFPE solution and the average vertical sonic gradient solution is shown.	82
7.8	Ground attenuation for case E_3 computed with the GFPE solver ATMOS and the Harmonoise model using a variable conformal mapping. As a reference result, the average vertical sonic gradient solution (REF_B) computed by the Harmonoise model is included.	83
7.9	The difference of the Harmonoise model with a variable conformal mapping and the GFPE solution for case E_3 . Also the difference between the GFPE solution and the average vertical sonic gradient solution is shown.	83
B.1	Image source method used to calculate the ground attenuation for a non-refracting atmosphere.	96
C.1	Temperature, velocity and effective sound speed profiles for a stable, an unstable and neutral atmosphere. Generated with $U = 8$ m/s at 80 meter, $z_0 = 0.1$, $T_s = 290K$ and Obukhovs lengths of 145,-86 and infinity respectively	99
C.2	Effective sound speed profile in case of a stable atmosphere fitted for the equation $c_{eff} = c_0 + Az + B \log(1 + \frac{z}{z_0})$	100

D.1	Two wavefronts occurring at different times. The variable $\mathbf{x}_p(t)$ is a point that moves along with the wavefront. The path of the function $\mathbf{x}_p(t)$ is called a ray path.	102
D.2	Ray path through a single layer of the atmosphere under the assumption of piece-wise linear approximation of the sound speed profile.	102
F.1	Illustration of the conformal mapping of two curves. Figure taken from [2]	107

List of Tables

2.1	Preferred 1/3 octave band center frequencies.	23
5.1	Input parameters of the Harmonoise model.	50
5.2	Limitations for the considered cases for verification of high sources	58
6.1	Parameters used in the source model to generate source data.	65
6.2	The Harmonoise model's input values for lin-log sound speed profiles in a stable, unstable, and neutral atmosphere.	66

Nomenclature

Roman Symbols

f	$[\frac{1}{s}]$	Frequency in Hz
c	$[\frac{m}{s}]$	Speed of sound
r	$[m]$	Distance between source and receiver
h_s	$[m]$	Source height
h_r	$[m]$	Receiver height
\mathbf{u}	$[\frac{m}{s}]$	Acoustic velocity vector
u	$[\frac{m}{s}]$	Horizontal component of wind velocity
t	$[s]$	Time
i	$[-]$	Imaginary number
k	$[\frac{rad}{m}]$	Wavenumber
p	$[\frac{N}{m^2}]$	Acoustic pressure
\mathbf{I}	$[\frac{W}{m^2}]$	Acoustic intensity
W	$[W]$	Sound power
L_w	$[dB]$	Sound power level
L_p	$[dB]$	Sound pressure level per frequency/octave band
\mathbf{n}	$[-]$	Normal vector
R	$[\frac{J}{Kkg}]$	Gas constant
T	$[K]$	Temperature
A	$[\frac{1}{s}]$	linear part or attenuation
B	$[\frac{m}{s}]$	logarithmic part

Greek Symbols

ρ	$[\frac{kg}{m^3}]$	Air density
ω	$[\frac{rad}{s}]$	Angular frequency
λ	$[m]$	Wave length
α	$[\frac{dB}{m}]$	Atmospheric absorption coefficient
θ	$[Rad \text{ or degrees}]$	Elevation angle
γ	$[-]$	specific heat ratio
ϕ	$[Rad \text{ or degrees}]$	Azimuth angle

Acronyms

SPL	$[-]$	Overall sound pressure level
2D	$[-]$	Two Dimensional
3D	$[-]$	Three Dimensional
PE	$[-]$	Parabolic equation
GFPE	$[-]$	Green functions parabolic equation
lin	$[-]$	linear
log	$[-]$	logarithmic

Subscripts

c	[-]	complex number
k	[-]	segment number
valley	[-]	valley shaped terrain
flat	[-]	flat terrain
0	[-]	value at ground level
eff	[-]	effective
av	[-]	average over a sufficiently long period of time
c,m	[-]	center frequency number m

Chapter 1

Introduction

Atmospheric acoustics is a branch of acoustics that studies sound propagation through the atmosphere. This is useful for a wide variety of applications, such as highway traffic noise, airplane noise, and wind farm noise. The attention given to wind farm noise propagation has particularly increased during the last few years as more and more wind farms are being built. In the Netherlands, for example, 8000 MW of wind turbine power is currently installed, with 70 percent of that capacity installed on land [3]. Because of this, 55 000 homes are within a one-kilometer radius of a wind turbine, and with the future plans of the government to generate 70% of the electricity from wind and solar power, this number is likely to rise even more [4].

Living within a one-kilometer radius of a wind turbine increases the exposure to noise emitted by wind turbines [5]. The noise of wind turbines is a controversial topic. A reason for this is that many people believe that wind turbine-related noise is a non-issue and that people complain just to stop a wind farm from being built in their neighborhood [1]. Another argument is that wind farm noise is less common than road traffic noise and the general sound levels are drastically lower [6]. Still, some people experience annoyance from wind turbine noise [7]. The cause of this could be that the “swooshing” sound of a wind turbine is more annoying than other environmental noise sources [8]. Some studies show a strong link between wind turbine noise and symptoms such as dizziness, sleep disruption, and even an increase in cardiovascular disease [1, 9, 10, 11]. The cause of symptoms like this is hard to prove, and because of this, studies generally produce mixed results [6]. However, it is inevitable that residents living nearby wind turbines will be exposed to noise, and, for this reason, it is important to predict the noise levels before the construction of the wind farm.

Wind turbine noise has to be properly regulated to reduce harmful side effects for nearby residents. The World Health Organization (WHO) states that indoor sound should not exceed 30 dB(A) in a resident’s bedroom for good sleep quality [12]. Current noise regulations in the Netherlands are $L_{den} = 47$ dB and $L_{night} = 41$ dB, which are the averaged noise levels over day-evening-night and only night outside a resident’s house, respectively (the noise levels are averaged over a period of a year). The idea is that these numbers correspond to the numbers recommended by the WHO for inside because a noise reduction from outside to inside is expected (more information about the reduction of noise levels inside can be found in [1]). Although, at the time of this writing, there is a lot of criticism in the Netherlands about these rules [7]. To meet a noise guideline and still be able to install wind turbines to meet energy needs, it is important to have reliable ways to simulate wind turbine noise. However, the atmosphere as a sound propagation medium is complex and dependent on time. Sound levels are influenced by a wide variety of factors, such as the type of ground, temperature, humidity, wind, etc. Accurate atmospheric sound propagation models that can account for all these effects have been developed in the past 30 years [13]. Unfortunately, most models require large computation times, especially for long propagation distances and high sources (like wind turbines). This makes them impractical in a lot of cases related to wind turbine noise [14]. Therefore, the main type of propagation model used nowadays for wind farm noise is analytical. Analytical models have low computational times but they are not always able to include important propagation effects. In other words, analytical models reduce computation time by introducing simplifying assumptions but lose accuracy in the process. Because of this, it is always necessary to assess whether the accuracy of these models is still adequate for a given situation.

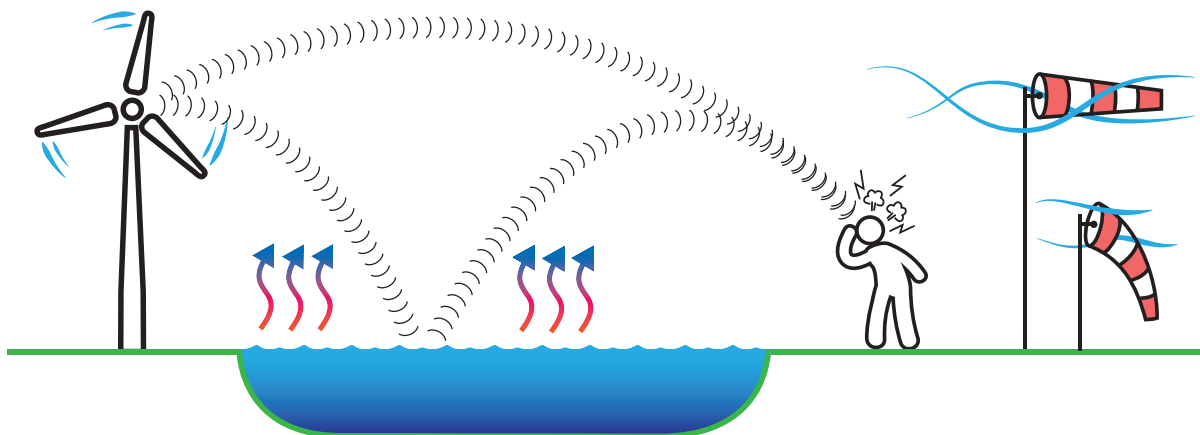


Figure 1.1: Possible scenario that will be simulated in this work.

There are numerous analytical models available, ranging from simple to very complex [15, 16, 17]. A model that is frequently used in the case of wind turbine noise is the ISO9613-2 model [18]. However, this model's accuracy (± 3 dB) is only validated up to a 1000 meter downwind in the absence of large wind gradients for a source height up to 30 meter [1]. A more recently developed analytical model is the Harmonoise model [19]. This model is more complex than the ISO9613-2 model and attempts to include several additional propagation effects.

One of the propagation effects that the ISO9613-2 model cannot accurately include is the bending (refraction) of sound waves. This happens because of variations in the speed of sound in the atmosphere (see section 3.1.4). These variations are caused by temperature and wind profiles in the Earth's boundary layer. At the Earth's surface, air molecules are slowed down by friction forces, which leads to a dependence of wind velocity on height. Local wind speeds can also be influenced by their surroundings. Temperature is also a function of height; most of the time, temperature decreases with height, but in some cases, temperature can increase with height (in chapter 6 more information is given). Because of the variation in sound speed, the sound wave is refracted, influencing the sound levels at a location.

This work focuses on the impact of sound speed gradients caused by temperature gradients and wind shear on sound propagation. A primary research goal is to evaluate the ability of the Harmonoise model to accurately predict these effects. The obtained conclusions are applied to the calculation of wind turbine noise. Additionally, a method is proposed to enable the Harmonoise model to include variations in horizontal sound speed, as it currently only considers sound speed as a function of height. Finally, a semi-analytical source model and the Harmonoise model will be used to simulate the noise of an existing wind turbine under various atmospheric conditions. This simulation illustrates how meteorological conditions can affect wind turbine noise propagation and provides an example of the expected sound levels around a wind turbine under simplified, but sometimes realistic, conditions. Figure 1.1 shows a scenario where a wind turbine is located near a small body of shallow water and a person is on the other side of the water. This picture serves as an analogy for the situation being considered: in this work, a fully reflecting ground in an open area is assumed, and water is a good reflecting surface. This situation is investigated at various times of day and night, as well as with and without strong winds.

The present work is divided into an introduction, six chapters, and closes with a discussion, conclusion, and recommendation. Chapter 2 provides an introduction to basic acoustic concepts necessary for the study of atmospheric acoustics. Chapter 3 introduces the various factors that influence sound propagation in the atmosphere. Chapter 4 describes the Harmonoise model. In chapter 5 the described model is implemented and validated to assess its suitability for use in wind turbine noise simulation. In chapter 6, the model presented in chapters 4 and 5 is combined with a source model to simulate a wind turbine. And at the end, in chapter 7 a method to include horizontal gradients in the Harmonoise model is proposed.

Chapter 2

Basic acoustics

This chapter is a brief introductory chapter about the basics of atmospheric acoustics. First, a definition of sound will be given, and afterward, several concepts that quantify the properties of sound will be introduced. In this chapter, these concepts will be used to calculate the amount of sound generated by a point source in free space. The wind turbine is modeled as a point source, and the analysis of a point source in free space can be seen as this work's starting point.

2.1 What is sound?

Sound is the result of local pressure fluctuations in the air that can, for example, be produced by vibrating objects. A source of local pressure fluctuations is referred to as a sound source. These changes in local pressure move away from the sound source and are perceived as sound. The pressure fluctuations are a small variation of pressure relative to the average atmospheric pressure and are referred to as sound pressure. A visualization of this explanation is shown in figure 2.1. The figure shows the locations of low and high pressures for a sound source and the corresponding graph.

Since the sound pressure oscillates from negative to positive in a certain amount of time, sound is best described in the form of a wave. The time it takes for the wave to complete one oscillation from a positive to a negative pressure difference and back is defined as the period, and the number of oscillations per second is the frequency. The frequency of a sound wave depicts the tone of the sound. A sound wave is termed a pure tone if it consists of only one frequency; however, sound usually consists of a wide range of frequencies. The amplitude of the sound wave is a quantity for the “loudness” and is described by the sound pressure level. More about the spectrum of frequencies and the sound pressure level is explained later in this chapter. First, a mathematical description of a wave is given.

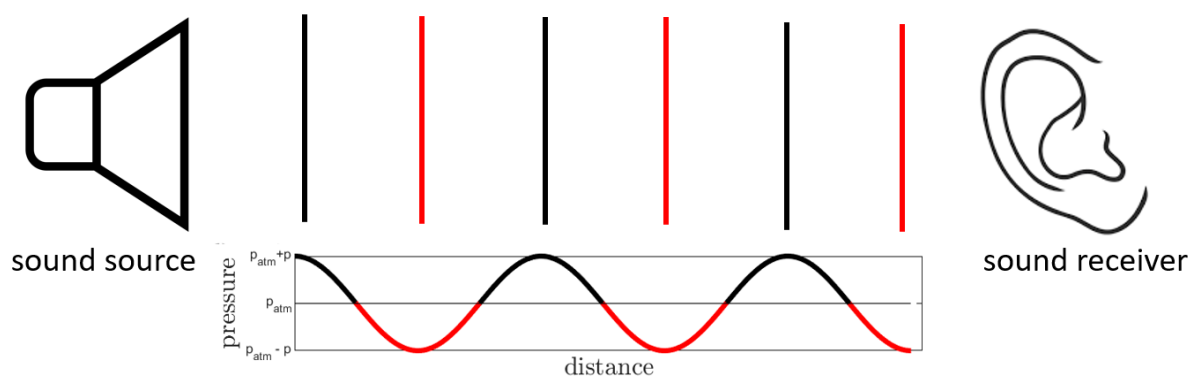


Figure 2.1: The black straight lines represent areas of high pressure, while the red lines represent areas of low pressure. The high pressure line is equal to the atmospheric pressure (p_{atm}) plus the sound pressure (p). The low pressure line is equal to the atmospheric pressure (p_{atm}) minus the sound pressure (p).

2.2 The wave equation

An idealization of many types of wave motion is mathematically described by the wave equation [20]

$$\nabla^2\phi - \frac{1}{c^2}\phi_{tt} = 0 \quad (2.1)$$

where c is the speed of sound [m/s], ϕ can be the sound pressure [Pa] and ϕ_{tt} is the second derivative with respect to time.

This equation is the starting point for most acoustic problems. Usually, some approximations can be made that simplify solving this equation.

A useful assumption can be that the wave is time-harmonic. Time-harmonic means that the wave repeats itself after a certain amount of time (an oscillation period). By assuming that the wave is time harmonic we can write [20]

$$\phi = \Phi(x, y, z)e^{-i\omega t}, \quad (2.2)$$

where ω is the radial frequency [$\frac{rad}{s}$] and Φ can be the (complex) pressure.

Substituting equation 2.2 in the wave equation leads to the wave equation in the frequency domain

$$\nabla^2\Phi + k^2\Phi = 0, \quad (2.3)$$

where k is the wave number defined as $k = \frac{\omega}{c}$.

Equation 2.3 is known as the Helmholtz equation. The advantage of the Helmholtz equation is that it is not dependent on time. This often makes the analysis of an acoustical problem much easier. A result of the transformation to the frequency domain is that the acoustic variables can now become complex numbers. An example of this is given in section 2.6, where the Helmholtz equation is used to describe a point source, while also addressing complex variables.

2.3 Speed of sound

Sound waves travel with finite speed. This speed depends on the type of medium and the temperature. By considering the fluctuations of sound as an adiabatic process, one can find the following relation for the speed of sound [13]

$$c = \sqrt{\gamma RT}, \quad (2.4)$$

where γ is the ratio of specific heats [-], R is a constant [J/(kg K)] and T is the temperature [K].

For dry air we have: $\gamma = 1.4$ and $R = 298$ J/(kg K). In that case equation 2.4 can be written as

$$c = c_0\sqrt{T/T_0} \quad (2.5)$$

with $T_0 = 273$ K and $c_0 = 331$ m/s (different combinations of values are also possible).

The sound speed discussed so far is known as the adiabatic sound speed. This is the speed at which a sound wave travels through a non-moving atmosphere. However, when wind is present, the atmosphere is in motion. Calculating the speed of sound in a moving atmosphere is more complex; a method to do this is the effective sound speed approximation [13].

2.3.1 Effective sound speed approximation

To bypass the complicated effects of a moving atmosphere, an approximation can be made that is called the effective sound speed approximation. This approximation simply adds the adiabatic sound speed and the wind velocity at a certain location to get the speed of sound at this location

$$c_{\text{eff}} = c + u, \quad (2.6)$$

where c is the adiabatic sound speed [m/s] and u is the horizontal component of the wind velocity [m/s] in the direction of sound propagation.

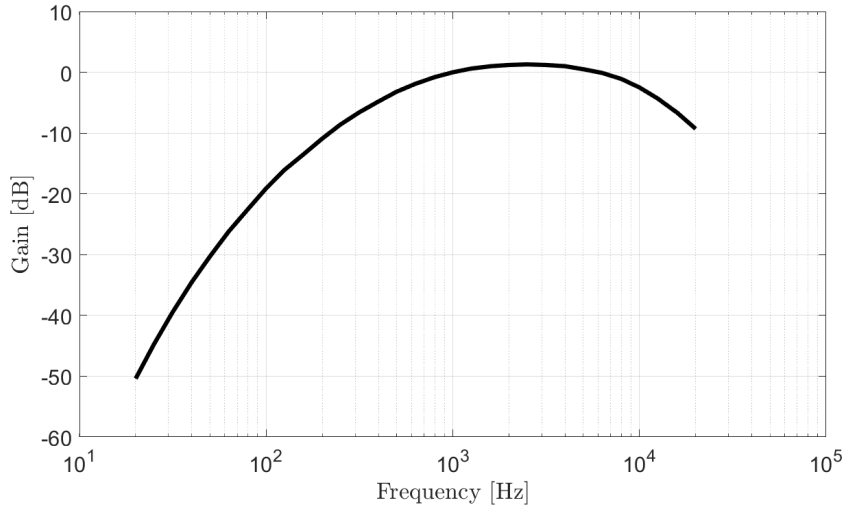


Figure 2.2: Gain of the dBA filter for 20-20000 Hz.

The idea behind this approximation is that when sound travels in a downwind direction ($u > 0$) the effective sound speed is faster relative to a stationary observer, and when it travels in an upwind direction ($u < 0$) the sound effectively travels slower due to the movement of the air. This approximation holds true only if sound travels at low elevation angles, where the elevation angle is the angle between the propagation direction of the sound wave and the (horizontal) x-axis. To ensure validity one should keep $|h_s - h_r| \ll d$, where h_s is the source height, h_r is the receiver height and d is the horizontal propagation distance [13]. For more information about the validity of the effective sound speed approximation see [21].

2.4 Sound pressure level

The sound pressure level describes how loud a sound wave is by considering the sound pressure. The average pressure of a harmonic sound wave over a full oscillation is zero (see figure 2.1). However, the average pressure squared over a full oscillation is not zero. Therefore the overall sound pressure level is defined as

$$\text{SPL} = 10 \log_{10} \frac{(p^2)_{\text{av}}}{p_{\text{ref}}^2}, \quad (2.7)$$

with $p_{\text{ref}} = 2 \cdot 10^{-5}$ Pa as the reference sound pressure and $(p^2)_{\text{av}}$ as the time average of the sound pressure squared over one oscillation period. The reference sound pressure value is near the absolute threshold for a human listener at a frequency of 1000 Hz [22]. Note that the sound pressure level is commonly represented on a logarithmic scale. A logarithmic scale is more convenient to use because a human ear can pick up a large range of sound pressure values. The unit for the logarithmic scale is dB.

Since the human ear is not as sensitive to every frequency, a commonly used unit is dBA. This unit corrects for the sensitivity of the human ear and is a better representation of the actual sound perceived. A result in dB can be transformed to dBA by adding the gain for the corresponding frequency. Visually the dBA filter is shown in figure 2.2. The figure shows that the human ear is most sensitive for frequencies between 1-5 kHz.

2.5 Sound velocity, -intensity, -power and -power level

In this section, four acoustic concepts will be introduced: sound velocity, sound intensity, sound power, and sound power level. These concepts are used often throughout the report and are also used to calculate the SPL around a point source.

2.5.1 Sound velocity

Sound velocity refers to the velocity of particles that comes along with the pressure wave. Air particles start to oscillate back and forth, and the corresponding velocity behaves like a wave. Note that since the air particles move back and forth, the net mass transport is zero in a sound wave. The sound velocity in combination with the pressure can give information about the energy of a wave.

2.5.2 Sound intensity

When a sound wave travels, energy is transported in the travel direction. The energy per unit area is defined as the sound intensity

$$\mathbf{I} = p\mathbf{u}, \quad (2.8)$$

where p is the sound pressure [Pa] and \mathbf{u} is the sound velocity [m/s]. The intensity is a function of time (t) and the time average (t_{av}) of the intensity is defined as

$$\mathbf{I}_{av} = \frac{1}{t_{av}} \int_0^{t_{av}} p\mathbf{u} dt, \quad (2.9)$$

where t_{av} depends on the type of waveform considered. For a periodic wave, this can be the time of a period, but for more irregular waves t_{av} should be larger.

2.5.3 Sound power

From the intensity we can define the sound power as

$$W_{av} = \iint_{S_a} \mathbf{I}_{av} \cdot \mathbf{n} dS_a, \quad (2.10)$$

where S_a is an arbitrary surface and \mathbf{n} is the normal vector on that surface. The sound power can be a measurement of source strength. In that case, the source needs to be within the surface S_a . The value of W_{av} does not depend on the choice of surface as long as the source is inside it. If no sources are present within the surface S_a , the flux will be zero everywhere and W_{av} will be zero.

2.5.4 Sound power level

The source power level is defined as

$$L_W = 10 \log_{10} \frac{W_{av}}{W_{ref}} \quad (2.11)$$

with reference sound power $W_{ref} = 1 \cdot 10^{-12} W$. The relation between the reference sound power and the reference pressure (equation 2.7) satisfies the relation

$$p_{ref}^2 \approx \rho c W_{ref}, \quad (2.12)$$

where ρ is the density [kg/m³].

2.6 Point sources

A point source is a sound source that sends an outgoing sound wave of equal amplitude in every direction. The solution of the pressure field induced by a point source can be obtained by assuming that the field has spherical symmetry. In that case, equation 2.3 becomes [13]

$$\frac{1}{r} \frac{\partial^2}{\partial r^2} (rp_c) + k^2 p_c = 0 \quad (2.13)$$

here p_c represents the complex pressure. The actual pressure can be retrieved by taking the real part of the the complex pressure, $p = \text{Re}[p_c]$.

The solution of equation 2.13 is

$$p_c = S \frac{\exp(ikr)}{r}, \quad (2.14)$$

where S is a constant and r is the radial distance from the observer to the source location. This result shows that the amplitude of the pressure wave is equal to S/r and thus decays with $1/r$.

2.6.1 Sound velocity of a point source

In this part, the sound velocity will be derived. Afterwards, the sound velocity and the sound pressure can be used to obtain the sound intensity of a point source.

The following equation serves as a starting point for our analysis. It is derived with the mass and momentum conservation equations. This is done under the assumption that the atmosphere is motionless, homogeneous, and that pressure changes are small in comparison to the overall atmospheric pressure [13]

$$\rho \frac{\partial \mathbf{u}}{\partial t} = -\nabla p. \quad (2.15)$$

This equation is one of the linear acoustic equations and can also be used in deriving the wave equation.

It is assumed that the source is time harmonic, meaning that \mathbf{u} depends only on time through the factor $e^{-i\omega t}$. Therefore the sound pressure and sound velocity are written as

$$p = \text{Re}(p_c e^{-i\omega t}) \quad (2.16)$$

and

$$\mathbf{u} = \text{Re}(\mathbf{u}_c e^{-i\omega t}). \quad (2.17)$$

Inserting equation 2.16 and 2.17 into equation 2.15 results in

$$\text{Re}[-i\omega \mathbf{v}_c + \nabla p] e^{-i\omega t} = 0. \quad (2.18)$$

Thus, the part between brackets should be 0 for all values of t . For this case, the gradient of the pressure depends only on r , which leads to the sound velocity in radial direction

$$v_c = \frac{1}{i\omega \rho} \frac{\partial p_c}{\partial r}. \quad (2.19)$$

The complex pressure was defined by equation 2.14 and is inserted into equation 2.19. This results into

$$v_c = \left(1 + \frac{i}{kr}\right) \frac{p_c}{\rho c}. \quad (2.20)$$

2.6.2 Sound intensity for harmonic point source

The sound intensity of a harmonic point source can be found in a similar way. Equation 2.16 and 2.17 are substituted in the definition for sound intensity (equation 2.8). The time average of the sound intensity can then be found as

$$\mathbf{I}_{\text{av}} = \text{Re}\left(\frac{1}{2} p_c^* \mathbf{v}_c\right), \quad (2.21)$$

where p_c^* is the complex conjugate of the sound pressure.

2.6.3 Sound pressure level for a harmonic point source

The relations for sound pressure and sound velocity of a harmonic point source were already found and stated below for convenience

$$p_c = S \frac{\exp(ikr)}{r}, \quad (2.14)$$

$$v_c = \left(1 + \frac{i}{kr}\right) \frac{p_c}{\rho c}. \quad (2.20)$$

At large distance from the source we can assume that $kr \gg 1$, resulting in

$$v_c \approx p_c / \rho c. \quad (2.22)$$

Inserting equation 2.14 and 2.22 in equation 2.21 results in the following sound intensity at large distances from the source

$$I_{\text{av}} = \frac{1}{2} \frac{|p_c|^2}{\rho c}. \quad (2.23)$$

To go from the complex pressure to the average pressure we consider the definition for average pressure:

$$(p^2)_{av} = \frac{1}{t_{av}} \int_0^{t_{av}} p^2 dt. \quad (2.24)$$

The pressure (p) can be obtained by $\text{Re}[p_c]$, which results in $p = \frac{S}{r} \cos(\omega t)$. The integration time is one period which is equal to $2\pi/\omega$, resulting in

$$(p^2)_{av} = \frac{\omega}{2\pi} \int_0^{2\pi/\omega} \frac{S^2}{r^2} \cos^2 \omega t dt. = \frac{S}{2r} = \frac{|p_c|^2}{2} \quad (2.25)$$

Therefore, the average sound intensity can also be written as

$$I_{av} = \frac{(p^2)_{av}}{\rho c}. \quad (2.26)$$

The source power is found by inserting equation 2.26 into equation 2.10. The arbitrary surface S_a is in this case chosen as a sphere with radius r centered in the origin. Since the average sound intensity at every point of the sphere is equal, the sound intensity can be taken out of the integral. The resulting equation is

$$W_{av} = \frac{(p^2)_{av}}{\rho c} \int 1 dS_a = 4\pi r^2 \frac{(p^2)_{av}}{\rho c} \quad (2.27)$$

Rewriting equation 2.27 to obtain the average pressure squared gives

$$(p^2)_{av} = \rho c \frac{W_{av}}{4\pi r^2}. \quad (2.28)$$

Finally, equation 2.28 is inserted in the definition of sound pressure level (equation 2.7) and with the relation between reference pressure and reference power (equation 2.12) we obtain

$$\text{SPL}(r) = L_W - 10 \log_{10} 4\pi r^2. \quad (2.29)$$

This equation describes the sound pressure level induced by a harmonic point source with strength L_W at a radial distance r from the source.

2.7 Non harmonic sources & Octave bands

In the previous section, the sound pressure level was derived for a harmonic point source. The analysis of a non-harmonic source can be done by decomposing the pressure signal. For the sound pressure level L_p this results in [13]

$$L_p(f_n) = 10 \log_{10} \frac{(p_n^2)_{av}}{p_{ref}^2}, \quad (2.30)$$

where $L_p(f_n)$ is the sound pressure level for a specific frequency, f_n is a set of frequencies where n depicts the number in the set and p_n the corresponding sound pressures. The overall SPL is defined by the logarithmic summation of all frequencies

$$\text{SPL} = 10 \log_{10} \sum 10^{L_p(f_n)/10}. \quad (2.31)$$

The value of $f_n - f_{n-1}$ can, for example, be a small spacing step of 1 Hz. Instead of using this narrow band spectrum in practice, one often uses an octave band- or 1/3 octave band spectrum. The narrow band spectrum is divided into bands with a upper, lower and center frequency. The sound pressure level of each frequency within one band is logarithmically summed to represent the center frequency of that band

$$L_p(f_{c,m}) = 10 \log_{10} \sum_n^l 10^{L_p(f_n)/10}, \quad (2.32)$$

Table 2.1: Preferred 1/3 octave band center frequencies.

[Hz]	12.5	25	50	100	200	400	800	1600	3150	6300
$f_{c,m}$	16	31.5	63	125	250	500	1000	2000	4000	8000
	20	40	80	160	315	630	1250	2500	5000	10000

here the prime indicates the summation over the whole frequency band and $f_{c,m}$ is the center frequency for band m .

To calculate the center frequencies one can use the approximate relation of [13]

$$f_{c,m} \approx f_{c,30} 2^{-10+m/3} \quad (2.33)$$

where m is a positive integer and $f_{c,30} = 1000$ Hz. For octave bands m runs with a multiple of 3 ($m = 3, 6, \dots$), while for 1/3 octave bands $m = 1, 2, 3, \dots$. The upper and lower limits of an octave band are calculated by $2^{1/2} f_{c,m}$ and $2^{-1/2} f_{c,m}$ respectively. For 1/3 octave bands the upper and lower limits can be calculated by $2^{1/6} f_{c,m}$ and $2^{-1/6} f_{c,m}$. The center frequencies obtained by the approximated relation are not round numbers. Therefore, one often uses the preferred center frequencies. The preferred center frequencies for 1/3 octave bands are given in table 2.1.

2.7.1 Sound pressure level for a non harmonic point source

Considering the previous sections, the equation to calculate the sound pressure level for a non-harmonic point source is presented. By decomposing the pressure signal equation 2.29 becomes

$$L_p(f, r) = L_W(f) - 10 \log_{10} 4\pi r^2, \quad (2.34)$$

where the frequency depends on the considered frequency spectrum.

2.8 Free field pressure

The value of the sound pressure level in free space is also known as the free field pressure. In the previous sections, we worked out how to find the free field pressure for a point source. From equation 2.7 we have $L_{p, \text{free}} = 10 \log_{10} \left(\frac{1}{2} |p_{\text{free}}|^2 / p_{\text{ref}}^2 \right)$ and $L_p = 10 \log_{10} \left(\frac{1}{2} |p_c|^2 / p_{\text{ref}}^2 \right)$. These relations give

$$L_p = L_{p, \text{free}} + \Delta L \quad (2.35)$$

where

$$\Delta L = 10 \log_{10} \left(|p_c|^2 / |p_{\text{free}}|^2 \right) \quad (2.36)$$

The quantity ΔL is called the relative sound pressure level. In the case of an octave band, $\Delta L(f)$ is a function with the corresponding relative sound pressure levels. However, ΔL should not be considered an octave band spectrum since the value does not depend on the bandwidth. When converting ΔL to a certain spectrum one should use logarithmic octave band averaging

$$\Delta L(f_c) = 10 \log_{10} \left(\frac{1}{N} \sum' 10^{\Delta L(f)/10} \right). \quad (2.37)$$

In the next chapter, additional effects that contribute to the sound pressure level will be described. These effects are referred to as attenuation mechanisms, but keep in mind that they represent the relative sound pressure level.

Chapter 3

Atmospheric sound propagation

The sound pressure level depends not only on the sound source but also on the surroundings, the distance, and the meteorological conditions. The sound pressure level can be obtained by adding these combined influences to the sound source

$$L_p = L_w + A_{att}, \quad (3.1)$$

where L_p is the sound pressure level, L_w the sound power level induced by a source, and A_{att} the influence of the surroundings, the distance, and the meteorological conditions.

In this section, we first analyze this A_{att} term and then introduce methods to calculate the sound pressure level at a location.

3.1 Attenuation mechanics

Six effects that influence the sound level will be explored, which are referred to as attenuation mechanisms. These attenuation mechanisms are: geometrical spreading, atmospheric absorption, reflection, refraction, diffraction and turbulence.

Most of these attenuation effects cause a reduction in sound level. Nevertheless, in next sections it will become evident that an increase in sound level is also possible.

3.1.1 Geometrical spreading

Consider a point source and a receiver separated by distance r in free space. The sound level perceived at the receiver decreases with distance due to the spreading of the sound power over a larger surface, see Figure 3.1.

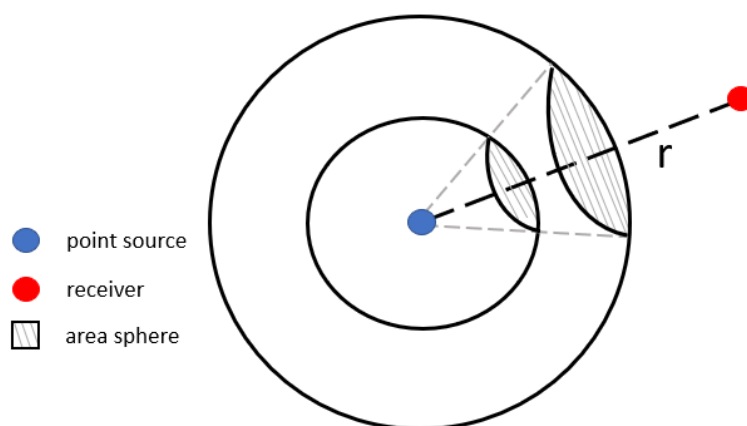


Figure 3.1: Spherical spreading from a point source in free space. The circular lines represent outgoing acoustical waves.

This is called geometrical spreading. In the case of a point source in free space, the spreading of sound power results in a reduction of sound intensity with r^2 , which is often referred to as the “inverse square law” [13]. In section 2.7.1 the sound pressure level for a non-harmonic point source in free space was found as

$$L_p(f) = L_W(f) - 10 \log_{10} 4\pi r^2 \quad (2.34)$$

where $L_P(f)$ and $L_W(f)$ are the sound pressure level and the sound power level respectively. $L_P(f)$ and $L_W(f)$ are both dependent on frequency and $10 \log_{10} 4\pi r^2$ is the attenuation term due to spherical spreading. This term implies that there is a 6 dB reduction in sound pressure level for every doubling of the distance with respect to the source [1, 13].

3.1.2 Atmospheric absorption

Another attenuation mechanism is atmospheric absorption, which occurs due to the interaction of a sound wave with air molecules. In this process, a wave loses energy to the air as it travels. The loss of energy is caused by two mechanisms [13]:

- Thermal conduction and viscosity of air.
- Relaxation losses of oxygen and nitrogen molecules in the air.

The first one is referred to as the “classical attenuation” and is caused by momentum transfer and heat flow as a result of velocity and temperature gradients. As the frequency rises, the gradients rise along with it, increasing air absorption. The second mechanism is the relaxation losses, which occur due to the compression and expansion of air. In these phases, molecules get excited and relaxed again. During this process, some energy is converted to heat, and thus some sound energy dissipates. Water plays an important role as a catalyst in these reactions. For this reason, atmospheric absorption is also dependent on the humidity of the air. The amount of atmospheric absorption is also dependent on the distance and can be described by the term αr . Including atmospheric absorption, the sound pressure level for a point source in free space becomes

$$L_p = L_W - 10 \log_{10} 4\pi r^2 - \alpha r, \quad (3.2)$$

where r is the propagation distance and α is a humidity and frequency dependent parameter.

For α there are empirical models available that give a realistic indication of its value. One of these models is the standard ANSI/ASA S1.26 (2014) [1]. The atmospheric absorption can be calculated per frequency and then added to the result of a narrow band spectrum. Appendix A demonstrates how to compute atmospheric absorption, in accordance with ANSI/ASA S1.26(2014). Figure 3.2 shows the effect of atmospheric absorption on the sound pressure level for a temperature of 293 Kelvin and a relative humidity of 25, 50, and 75%.

The figure clearly indicates that the atmospheric absorption effect is most pronounced at higher frequencies. This is also one of the main reasons why low tones are more frequently heard from a distance than high tones in the case of noise pollution. Relative humidity plays a less important role because its effect only becomes pronounced at higher frequencies, where the reduction in sound is already considerable.

3.1.3 Reflection

Surfaces can reflect sound waves, and because of this, multiple sound waves may reach the receiver position due to reflection. This phenomenon is depicted in figure 3.3 by placing a point source over a reflective surface.

The concept of “ray,” which denotes the direction in which a sound wave propagates, is introduced in the graphic for clearer understanding of the phenomenon (a more formal definition is provided in Appendix D). The sound pressure of the two sound rays can be summed to determine the sound at the receiver location. If the phase of the two rays is identical, constructive interference takes place, increasing sound pressure by 6 dB. Destructive interference occurs when the two incoming rays are in phase opposition, resulting in zero sound pressure at the receiver location.

The phase of a sound ray is mainly influenced by three things:

1. The wavenumber

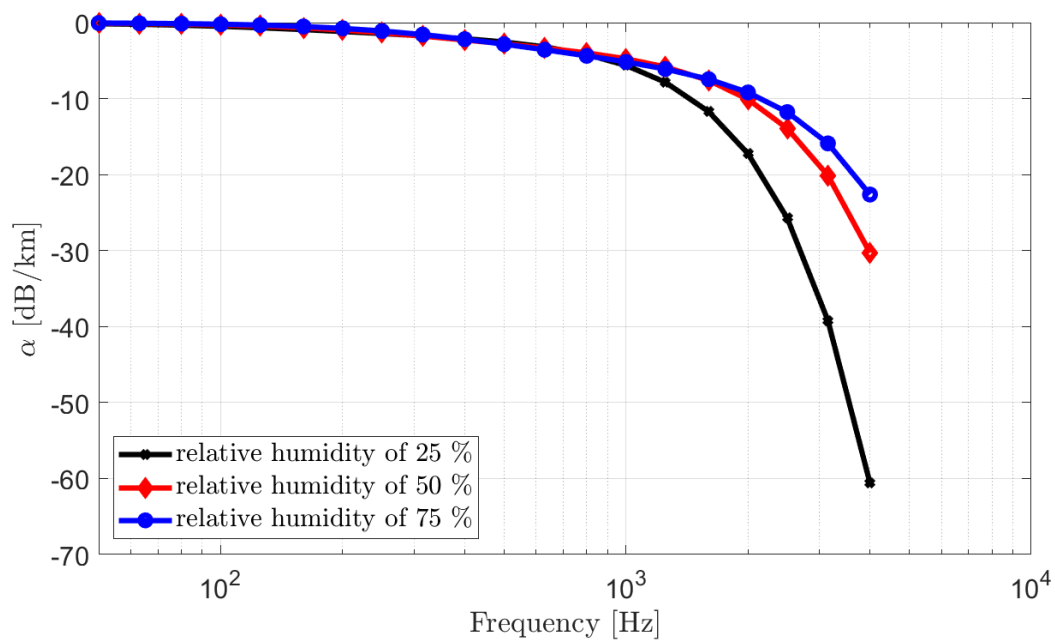


Figure 3.2: Effect of atmospheric absorption on the sound pressure level with respect to frequency for an ambient atmospheric temperature of 293 Kelvin.

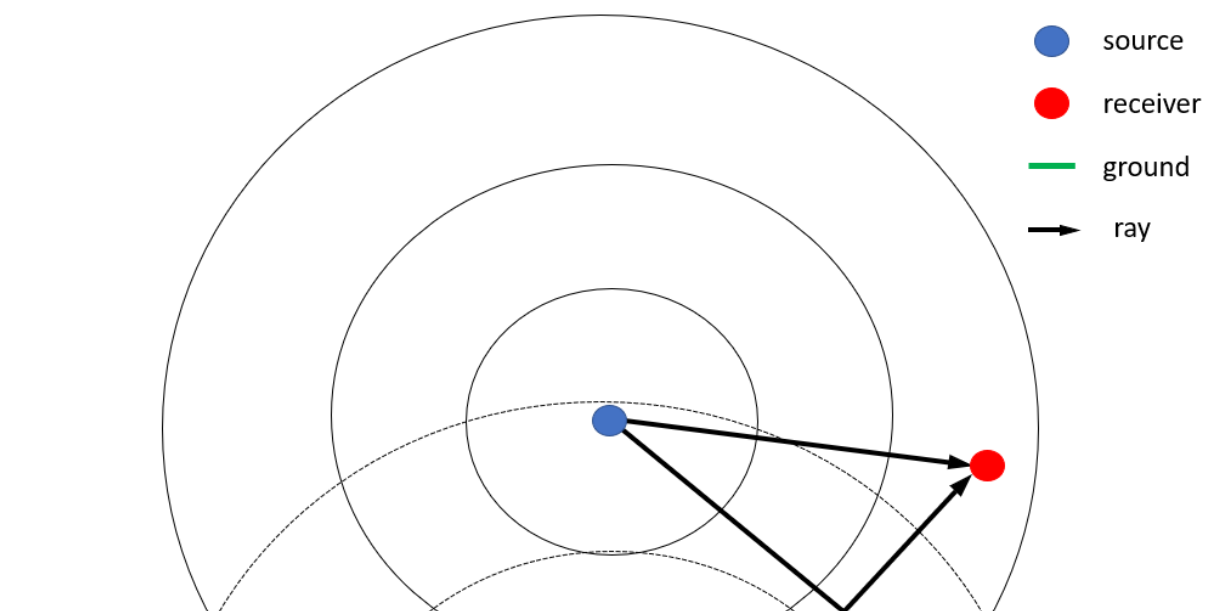


Figure 3.3: Point source over a reflecting surface, where the dotted circular line depicts the reflective part of a wave.

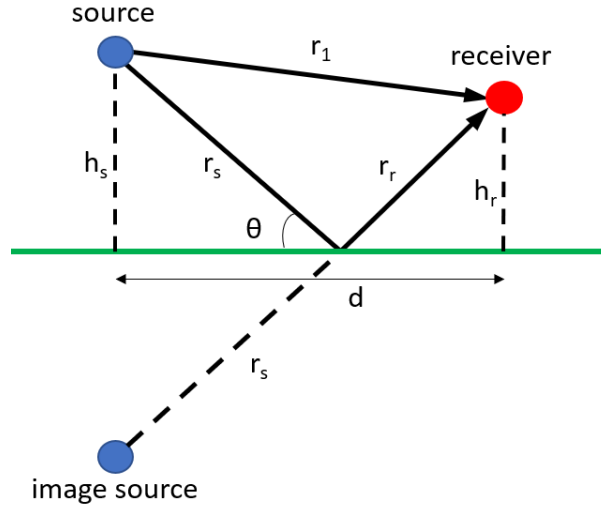


Figure 3.4: Image source method, the path length of the reflected ray path is $r_s + r_r$. In the figure is θ the elevation angle.

2. The propagation distance; distance travelled by the ray
3. The type of reflective surface

The frequency and speed of sound are used to calculate the wave number, which is defined as $k = \frac{2\pi f}{c}$. It is also called the spatial frequency and describes the number of waves per meter. To calculate the (normalized) phase, one can multiply k with the propagation distance. Only the relative phase difference is important when summing up the contributions of two rays. This can be obtained by

$$\Delta\phi_{rel} = k \cdot (r_1 - r_2), \quad (3.3)$$

where $\Delta\phi_{rel}$ is the relative phase difference, r_1 is the distance of the propagation path of ray 1 and r_2 the distance of the propagation path of ray 2.

The phase of a sound wave can also shift upon reflection. When a sound wave impacts the surface, part of the wave is reflected and part is transmitted into the surface. The reflected wave has a smaller amplitude than the incoming wave, and the phase of the wave can shift. The decrease in amplitude and shift in phase are dependent on the type of surface and elevation angle at the reflection interface. When the elevation angle is small (close parallel), this effect actually becomes very complex due to the spherical nature of the wave. See references [1, 23] for more information. For the sake of simplicity, it is assumed that all reflecting surfaces in this study are acoustically “hard”. An acoustically hard reflection surface means that upon reflection no phase shift and no reduction in amplitude occurs, which is characterized by an infinitely large impedance.

A method to calculate the attenuation that occurs due to the reflection is to place an image source below the actual source, see figure 3.4. In the figure, the direct propagation path from the image source to the receiver is the same as the reflected path from the source to the receiver. Consider a case where we assume an acoustically hard surface, a constant speed of sound of 340 m/s and put $h_s = 15$ m, $h_r = 12$ m, and $d = 50$ m. The reflection attenuation can now be found and is illustrated in figure 3.5. Details of the calculation can be found in Appendix B.

First of all, it is important to note that the results are in the 1/3 octave band spectrum and in the narrow band spectrum. There are many large minima in the narrow band spectrum. With a continuous spectrum, these minima would be $-\infty$. Because it is a narrow band spectrum rather than a continuous spectrum, not all minima have the same value. At higher frequencies, the wavelength is shorter, and therefore the minima are closer together. The 1/3 octave band result is the logarithmic average of the narrow band result. At low frequencies of the 1/3 octave band result is the interference pattern clearly visible, but at high frequency the attenuation tends to go to 3 dB. This value is to be expected as the phases between rays in a high frequency band become more random, and a random (incoherent) addition of sound waves results in a 3 dB increase in sound [24]. In figure 3.4, there is a maximum ground attenuation of 6 dB. The reason for this is that the maximum number of reflections that can

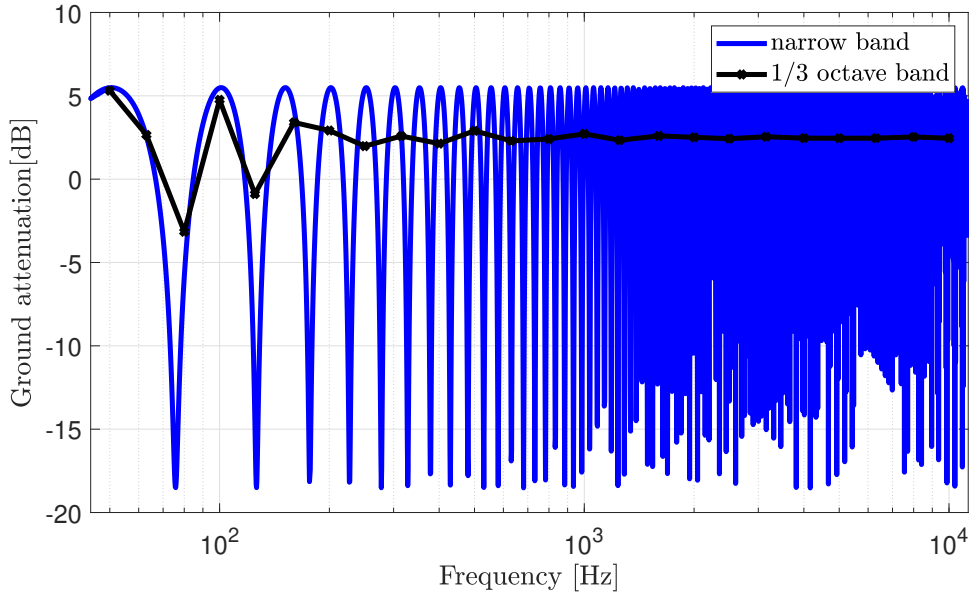


Figure 3.5: Reflection attenuation for different frequencies. The results are presented as the averaged 1/3 octave center frequencies.

reach the receiver in this case is one. As we will see in the following section, it is also possible that more reflections arrive, in which case the ground attenuation can exceed 6 dB.

3.1.4 Refraction

The next attenuation mechanism is refraction. Refraction is the bending of sound waves caused by the presence of a varying sound speed. Sound waves bend towards lower sound speed regions and thus do not always travel in straight lines. The amount of refraction is defined by Snell's law of refraction [13]

$$\frac{\cos \theta_1}{c_1} = \frac{\cos \theta_2}{c_2}, \quad (3.4)$$

where θ_1 is the elevation angle of the ray entering the medium, c_1 the sound speed of the current medium, θ_2 is the elevation angle of the ray leaving the medium and c_2 is the sound speed of the medium that the ray enters, see figure 3.6. For a continuous medium, like the speed of sound in the atmosphere, Snell's law states that the ratio of the elevation angle and the speed of sound are constant along a sound ray

$$\frac{\cos \theta}{c} = \text{constant along a sound ray.} \quad (3.5)$$

By integration of this condition, the path of a ray can be found [25].

Refraction affects a ray's phase and the number of rays that arrive at a given point. It can therefore have a significant impact on the sound field. Only for short propagation distances can refraction be neglected, because then the refraction is still minimal [13]. Refraction is a complicated subject since the atmosphere can be a non-constant medium with varying levels of refraction at various regions. Computation methods that can include refraction are described in section 3.2. Appendix C discusses the variation of sound speed in the atmosphere. In this section, we will limit ourselves to solely examining the refraction-related effects induced by a vertical linear wind speed profile.

The speed of sound induced by the wind can be approximated as $c_{eff}(z) = c + u(z)$ (see section 2.3.1), where u is the wind speed in the direction of the sound speed at height z . This means that the speed of sound will be greater when a sound wave moves along with the wind and smaller when it moves against the wind. The effect of a linear wind speed profile on a point source above a ground surface is depicted in Figure 3.7. When sound waves travel against the wind, the speed of sound will be smallest where the wind velocity is largest. In other words, the speed of sound decreases with height in this case. Hence, sound waves traveling against the wind refract upward. When a sound wave travels along with the wind, this effect is reversed. Which means the sound speed will increase with height, causing

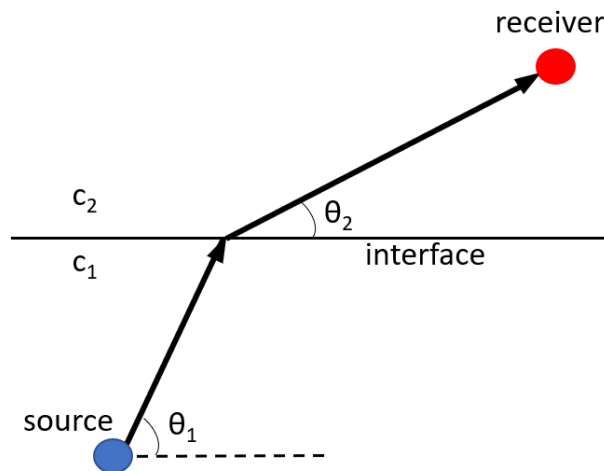


Figure 3.6: Refraction in the case of a discontinuous medium. Below the interface, the speed of sound is equal to c_1 and above the interface to c_2 .

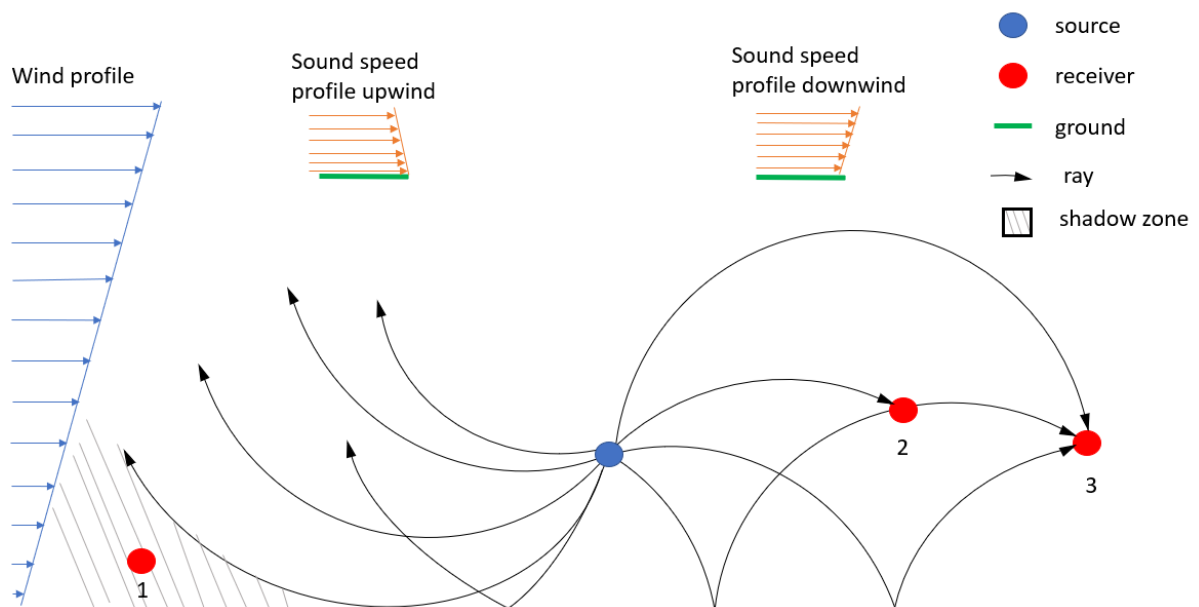


Figure 3.7: Several rays visualized from a source for a linear sound speed gradient. In the figure three receivers are shown that are affected by the refraction. The speed of sound profile is $c_0 + u$. The corresponding sound speed profiles are shown for upwind propagation and for downwind propagation.

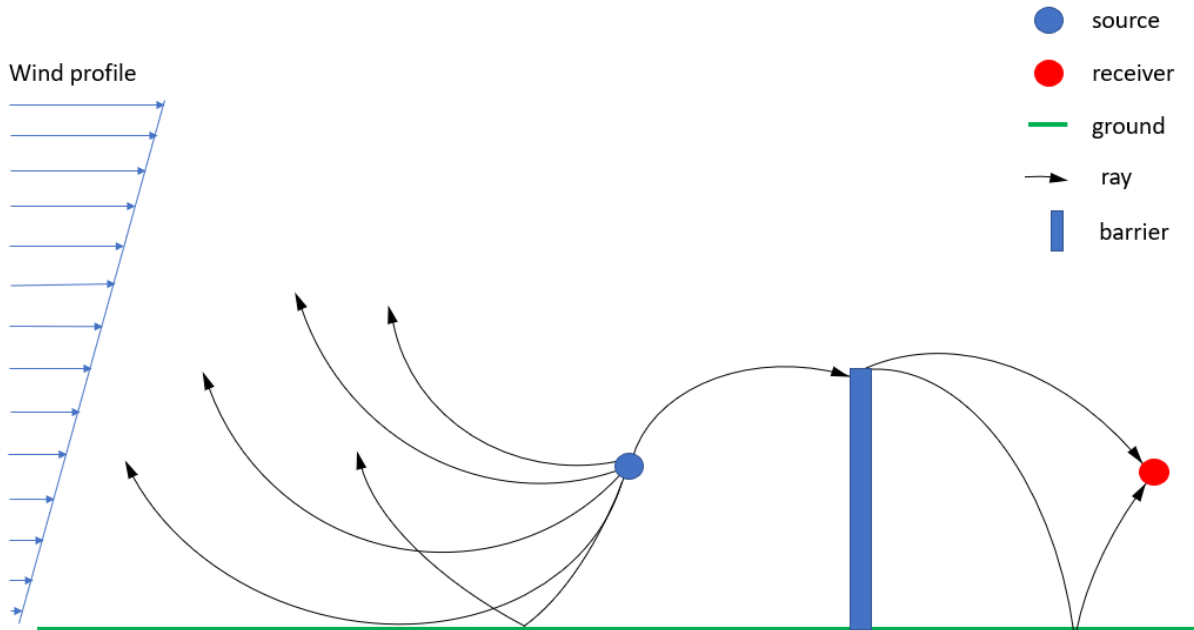


Figure 3.8: Ray visualization of sound diffracting around a barrier.

downward refraction of the waves. In figure 3.7, the sound speed profile as experienced by the sound waves is illustrated for upwind and downwind propagation.

To illustrate the effect on the sound level induced by refraction, first consider receiver 1 in Figure 3.7. Here, not a single ray will arrive at the receiver, and therefore the expected sound pressure is zero. The zone that no ray can reach is referred to as the “shadow zone.” In reality, the sound pressure in the shadow zone is very low, but not zero, due to the effects of turbulence and diffraction, which are discussed further in this section. Receiver 2 is reached by two rays: the direct ray and the reflected ray. Thus, depending on the phase between the rays, the sound level is either increased or decreased. At receiver 3 multiple rays arrive, indicating that the sound level is relatively large at this point (multiple reflected rays mean that the ground attenuation can exceed 6 dB). The number of rays that can arrive at the receiver increases as one moves further downwind from the source. Thus, refraction can cause multiple rays to arrive at a receiver downwind, while in case of no refraction only two rays would have arrived.

3.1.5 Diffraction

Diffraction occurs when a wave encounters a barrier. When this happens, some of the wave is reflected, while the other part bends around the barrier. How the wave bends around the object depends on the frequency of the wave and the object itself. When a person stands around a corner and speaks, we are able to hear the person but are unable to see the person. This can be explained by the fact that the wavelength of light is much smaller than the wavelength of audible sound, and therefore sound is able to diffract around the corner but light is not. For wind turbine applications, diffraction becomes important when large objects form a barrier between the source and the receiver, as is the case in figure 3.8.

In this report, sound propagation is determined for wind turbines. Wind turbines are high sources. Thus, the line of sight between a wind turbine and a receiver is only influenced by relatively large obstacles. If no such obstacles are present, diffraction does not have a lot of influence. Therefore, diffraction is disregarded in further analysis but can be described by most sound propagation methods (see section 3.2).

3.1.6 Turbulence

The final attenuation mechanism is turbulence. The sound profile in figure 3.8 was assumed to be a smooth profile that does not change with time. In reality, on the scale of seconds or minutes, the velocity and temperature of the atmosphere can randomly fluctuate. This fluctuation is known as turbulence and causes random local fluctuations in sound speed [13]. Section 3.1.4 showed that a variation in

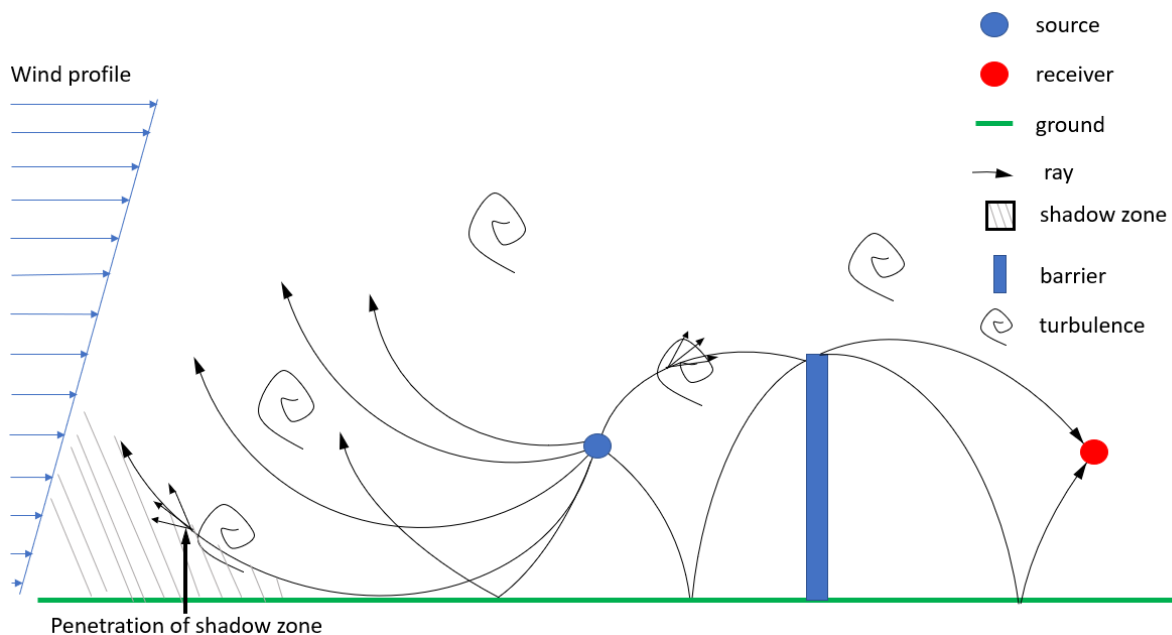


Figure 3.9: Illustration of small scale refraction due to turbulence.

sound speed leads to bending of the sound wave. In case of turbulence small scale refractions occur. Figure 3.9 illustrates these small scale refractions. The effect of this is that a ray path will randomly fluctuate, resulting in random fluctuations in amplitude and phase. In the case of a downward refracting atmosphere (at the right side of the source in figure 3.9) two or more rays arrive at a receiver location. All of those rays will be affected by random fluctuations in amplitude and phase. Therefore, the location of local minima; the location where deconstructive interference takes place, shifts at a certain interval. When this is averaged over time, the result is that the depth of the peaks of the interference minima is reduced.

In the case of an upward refracting atmosphere, an additional phenomenon is present. Near the source, where still several rays arrive, a reduction of local minima will happen. However, no rays arrive further away from the source, in the shadow zone. Without turbulence, the sound levels in the shadow zone would be zero, but due to the small refractions, sound can penetrate the shadow zone.

In this report, most attention is given to the downward-refracting atmosphere and not much to the shadow zone. Thus, the simplification is made to disregard turbulence. Therefore, one needs to keep in mind that, in reality, the peaks of the local minima will be reduced.

3.2 Models to calculate the sound propagation

Several types of models are available for the calculation of the sound pressure field in the atmosphere. The three main types that have been applied to wind turbine noise are identified and briefly described here: ray tracing, parabolic equation method, and engineering methods.

3.2.1 Ray tracing

The first model is called ray tracing. Ray tracing uses the idea of “tracing” all the relevant different ray paths and summing the contributions of all rays at certain locations to estimate the sound pressure level [13, 25, 26]. Ray tracing is used for a wide variety of applications, such as room acoustics, ocean acoustics, and atmospheric acoustics. What makes ray tracing so appealing is that it is very intuitive. All ray paths in a domain can be visualized to quickly get a sense of the propagation of sound in a situation. To illustrate this, consider a source placed above a reflecting surface at a height of 2 meters. The effective sound speed profile in the example is assumed to be in the form of

$$c_{\text{eff}}(z) = c_0 + B \log \left(\frac{z}{z_0} + 1 \right) \quad (3.6)$$

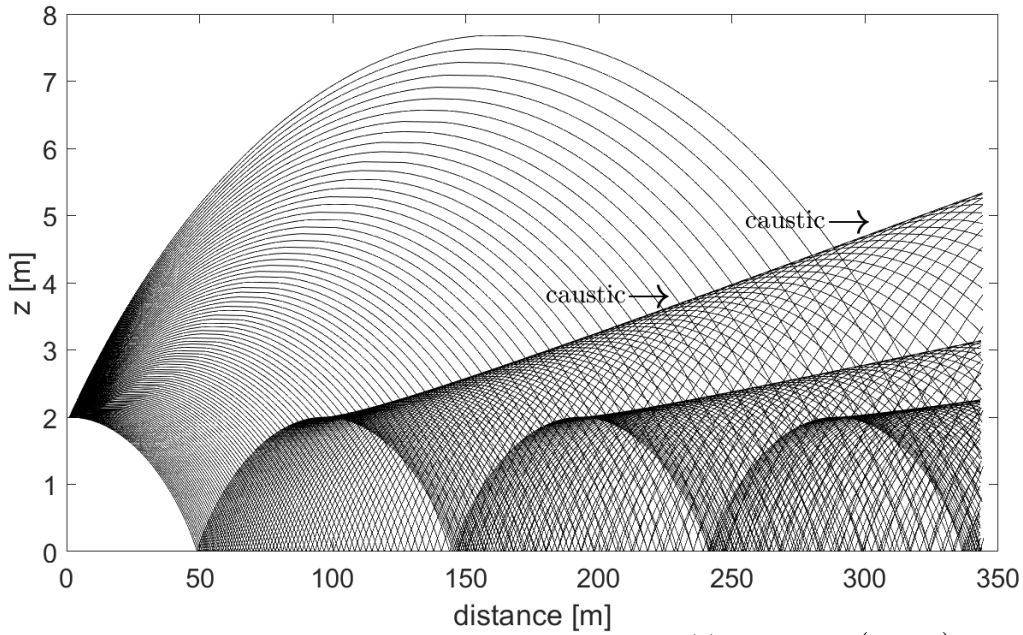


Figure 3.10: Ray tracing in an atmosphere with sound speed profile $c_{\text{eff}}(z) = 340 + \log\left(\frac{z}{0.1} + 1\right)$. In the figure, 100 rays are illustrated with shooting angles between 0 and 5°, where the angle is the angle between the ray and the horizontal.

with $c_0 = 340$ m/s, $B = 1$ m/s and $z_0 = 0.1$ m. Figure 3.10 shows the computed ray paths for this case. More information about this computation can be found in Appendix D.1. In the figure, one can directly see how the sound energy propagates through the atmosphere. At locations with a high ray density, relatively large sound levels are present, and at locations with a low ray density, the sound levels are relatively low. Also, multiple reflections are occurring, resulting in more than two rays arriving at some locations. This case is a good illustration of a possible scenario of downwind sound propagation.

Figure 3.10 gives a good first grasp of what is happening in downwind sound propagation. However, calculating the actual sound pressure turns out to be more complex. A reason for this is the occurrence of caustics. Caustics are curves where the normal distance between two rays, with small differences in elevation angle, vanishes (see figure 3.10). In ray tracing, the normal distance between two rays is a measure of the concentration of rays, which is used to calculate the sound pressure level. The result is that the estimated sound pressure level will be infinite at caustics [25]. This is not physical, as the actual sound pressure is large near caustics but not infinite. Furthermore, when a ray passes through a caustic, a phase shift happens. If this phase shift is not taken into account, errors may arise also arbitrarily far from the caustics. Dealing with caustics is possible, but the complexity is a drawback of this methodology [13].

In comparison to the parabolic equation method (discussed in the next part), the accuracy of ray tracing can be somewhat low. This is because ray tracing is essentially a high-frequency approximation of the wave equation (see e.g. [25]). A rule of thumb is that the considered wavelength should be much smaller than any physical scale in the problem. However, it remains difficult to predict whether ray tracing will produce sufficiently accurate results. Ray tracing is now most commonly used when environmental uncertainty imposes the largest constraint on the accuracy achievable.

3.2.2 Parabolic equation method

The second type of sound propagation model is based on solving the parabolic equations (PE). Parabolic equations arise from small- or large-angle approximations of the wave equation [13]. These differential equations are then solved with common numerical techniques. A large advantage of the PE method is that it can be used for non-homogeneous ground surfaces and large sonic gradients [13]. One limitation of the PE method is that it is applicable for small elevation angles only. This is due to approximations made in the derivation of the parabolic equation and the use of the effective sound speed approximation. Another limitation of the PE method is the computational cost: the grid points increase rapidly with increasing

frequency, and for a lot of 3D problems the computational power required is too high. An approach that is often used in atmospheric acoustics is to use the Green's function parabolic Equation (GFPE) method to solve the PE [27]. This increases the computational efficiency in comparison with other PE methods by enabling the possibility for coarser grids in the propagation direction [28]. A more detailed explanation of PE methods and the GFPE method is provided in Appendix E.

3.2.3 Engineering models

The computing time of ray tracing and parabolic equation solvers is a significant limitation for some practical applications. In these cases, engineering models can be used instead. These models are ray based but do not use an iterative scheme to trace all ray paths; instead, ray paths are approximated analytically. The rays are used in several analytical models to roughly represent the sound pressure due to the propagation effects. This approach reduces the computational time significantly [1]. A drawback of engineering models is that the assumptions used to derive them might not be valid in some conditions. This will result in a lower accuracy of the results when compared to standard ray tracing or PE methods.

The general approach of engineering models is to calculate the sound pressure level by summation of individual attenuation effects to the sound power level, which was defined in the introduction of this chapter as

$$L_p = L_W + A_{att}, \quad (3.1)$$

where

$$A_{att} = A_{div} + A_{atm} + A_{gr} + A_{refr} + A_{dif} + A_{tur}, \quad (3.7)$$

is the sum of all the attenuation mechanisms described above: geometrical spreading, atmospheric absorption, ground reflections, refraction, diffraction, and turbulence, respectively.

All these effects are approximated and linearly added to the sound power level to obtain the sound pressure level at a location. A problem with this approach is that most effects are interrelated, and treating them individually leads to an increase in error [1]. Only the more complex models attempt to account for this by combining some propagation effects. Furthermore, engineering methods calculate the sound pressure level in the octave- or 1/3 octave band spectrum. This is because at single frequencies, constructive or destructive interference will cause interference peaks. A small error at the frequency at which this occurs is expected, and by averaging out the results over a band, the final results give a better approximation of reality.

The next chapter explains the Harmonoise model in detail, which is a state-of-the-art engineering model.

Chapter 4

The Harmonoise model

The Harmonoise project aimed to improve noise mapping in the European Union. At the end, it produced two types of models: a reference model that uses a combination of numerical techniques to evaluate outdoor sound [29] and an engineering model [19]. From this point on, the Harmonoise engineering model will be referred to as the Harmonoise model. For low sources (< 5 m) and relatively short propagation distances (< 300 m), the Harmonoise model has been proven to be accurate (± 3 dB) for environments with several diffraction edges and varying ground properties [19, 30].

This chapter only describes the Harmonoise model for the effects of geometrical spreading, atmospheric absorption, reflections, and refraction. The effect of refraction is combined with the other attenuation mechanisms. Therefore, equation 3.7 becomes

$$A_{att} = A_{div} + A_{atm} + A_{gr}. \quad (4.1)$$

The Harmonoise model calculates the sound levels in 1/3 octave bands and thus equation 3.1 becomes

$$L_p(f_n) = L_W(f_n) + A_{att}(f_n), \quad (4.2)$$

where f_n are the center frequencies of the 1/3 octave band.

In this chapter, the calculation procedure of the Harmonoise model for attenuation effects in equation 4.1 is described first, followed by a discussion of the limitations. The described model is then implemented in Matlab code. This code's output is compared to reference solutions. The emphasis of these comparisons is on ground attenuation in conjunction with refraction to determine the Harmonoise model's ability to accurately capture the influence of various atmospheric conditions (and hence different sound speed profiles).

4.1 Geometrical spreading & Atmospheric absorption

The geometrical spreading term, A_{div} , was defined as $-10 \log_{10} 4\pi r^2$ by equation 2.34. The distance between source and receiver r can be found by

$$r = \sqrt{d^2 + (h_s - h_r)^2}, \quad (4.3)$$

where d is the horizontal distance between source and receiver, h_s the source height and h_r the receiver height.

Atmospheric absorption is implemented as described in section 3.1.2. It is a function of distance, frequency, humidity and temperature. This implementation is meant for single frequencies, with as consequence that in the case of 1/3 octave bands, the error increases. Therefore, a correction is made to the atmospheric absorption [1]

$$A_{atm} = A_0 (1.0053255 - 0.00122622A_0)^{1.6}, \quad (4.4)$$

where A_0 is equal to αr and can be calculated as described in Appendix A.

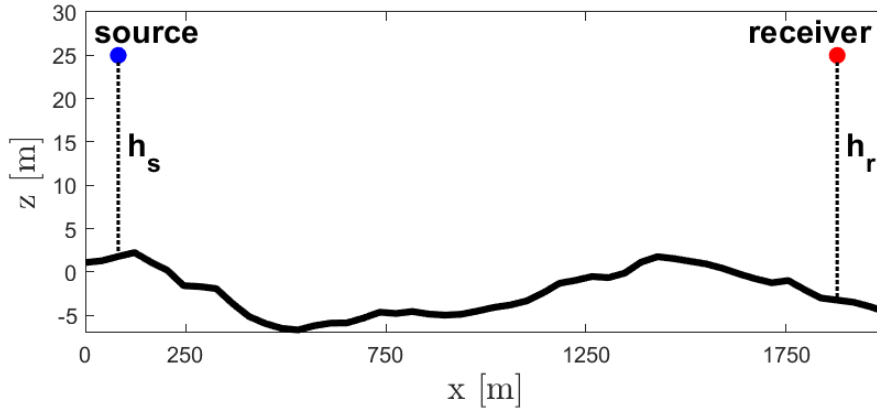


Figure 4.1: A source and receiver placed above a randomly generated ground profile.

4.2 Ground reflections

In this section and section 4.3, the method used by the Harmonoise model to calculate the attenuation caused by ground reflections will be explained. The model is constructed in the vertical xz -plane and includes both a source and a receiver. The overall process consists of three steps:

- Segmentation of the actual ground profile.
- Calculation of the contribution of each individual segment.
- Combining the contributions of each segment to obtain the overall attenuation.

As an illustrative example, consider a source and receiver placed above a randomly generated ground profile. The height of the source with respect to the ground profile is h_s , and the height of the receiver is h_r . This configuration is shown in figure 4.1.

To calculate the ground attenuation in this situation, first the ground has to be segmented, which is discussed in the next section.

4.2.1 Ground segments

A ground profile is described by N straight line segments. The coordinates of the end points of these segments are labeled as P_i with $i = 0, 1, \dots, N$. The x, z coordinates of a point P_i are (x_i, z_i) . Individual ground segments are labeled with $k = 1, 2, \dots, N$, where the first segment is $P_0 - P_1$. The locations of the source and receiver are $(x_0, y_0 + h_s)$ and $(x_N, y_N + h_r)$ respectively. The terrain that has to be segmented is an input parameter in the Harmonoise model. To do the segmentation as efficiently as possible, parts of the terrain that have large changes in slope need additional segments, while relatively constant parts of the terrain can be modeled with only a few segments. A method for efficient segmentation is described below [1].

Consider the example terrain displayed in figure 4.1. Draw a line from the start point to the end point of the terrain (see figure 4.2). The next step is to find the ground point that is farthest away from this line, which is labeled as L_1 . Point L_1 in combination with the begin and end points represents the terrain approximated by two segments. Following that, two lines can be drawn: one from the start point to point L_1 and another from point L_1 to the end point. Repeat the process of finding the ground point furthest from those two new lines to find point L_2 . Note that the distance from a point to a line in 3D space can be calculated as [31]

$$d = \frac{|(\mathbf{x}_2 - \mathbf{x}_1) \times (\mathbf{x}_1 - \mathbf{x}_0)|}{|\mathbf{x}_2 - \mathbf{x}_1|}, \quad (4.5)$$

where \times is the cross product, \mathbf{x}_0 contains the coordinates of the point in 3D space, \mathbf{x}_1 the beginning of the line and \mathbf{x}_2 the end of the line. To use this formula in 2D space one can simply put the third component of the vectors as 0.

Following this procedure for 10 segments, the considered ground profile of figure 4.1 will be segmented as figure 4.3.

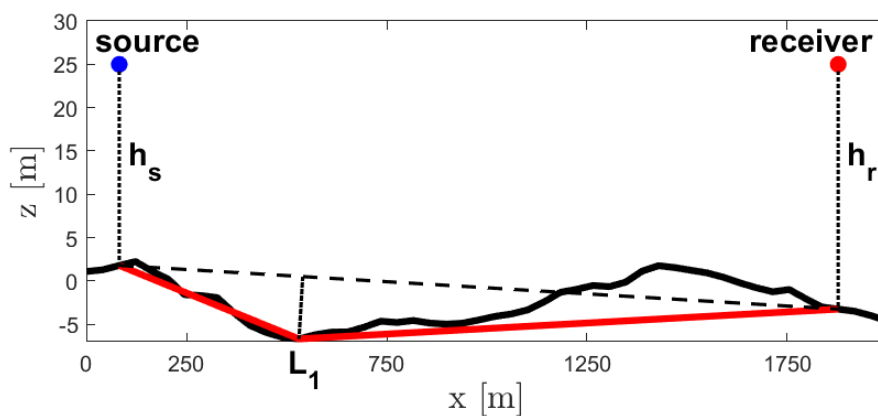


Figure 4.2: Segmentation of the ground profile in case of two straight line segments.

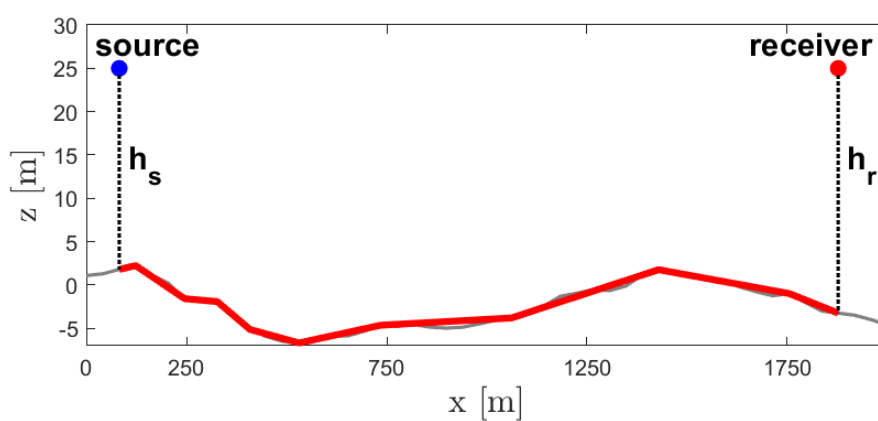


Figure 4.3: Segmentation of the ground profile in case of 10 straight line segments.

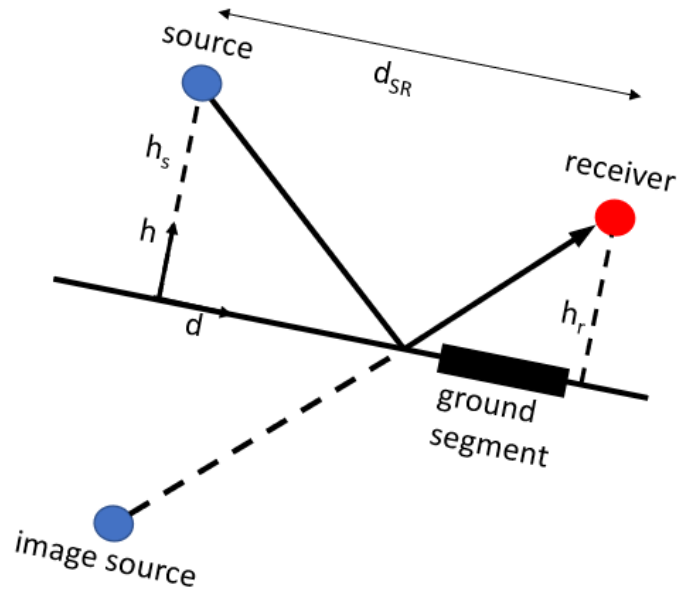


Figure 4.4: Local coordinate system of a ground segment.

The number of segments can be increased until certain conditions are met, such as the shortest segment length and the greatest distance between the segmented profile and the actual profile [19]. The obtained segmentation is the situation which is solved by the Harmonoise model, using the concave model. The concave model is explained in the next section.

4.3 Concave model

The Harmonoise model calculates the ground attenuation by summing up the contributions of each segment. The ground effect's attenuation, where the ground attenuation is defined as the actual pressure divided by the free field pressure (see section 2.7.1), is conceptually predicted by the model as

$$\Delta L = 20 \log \left| \frac{p}{p_{free}} \right| = \sum_{i=0}^N \Delta L_{G,k} \quad (4.6)$$

where p is the acoustical pressure, p_{free} the acoustical pressure in the free field and $\Delta L_{G,k}$ is the ground attenuation per segment.

Each ground segment uses a local d, h coordinate system as illustrated in figure 4.4, where the ground segment has its own local source height (h_s) and receiver height (h_r).

Depending on h_s and h_r , three types of ground segments can be distinguished:

- concave segments, with $h_s > 0$ and $h_r > 0$
- convex segments, with $h_s < 0$ or $h_r < 0$
- hull segments, with $h_s = 0$ and $h_r = 0$

The concave model is used if the ground consists only of concave segments. For the cases that will be considered in this report, only concave segments can be used. This is because the considered cases are all flat ground profiles, resulting in only concave segments except for upwind propagation close to the shadow zone. Therefore, only the concave model is considered.

4.3.1 Flat and deep-valley ground attenuation

The concave model is based on a two ray approximation [30]

$$\Delta L_G = 10 \log (|1 + CQD|^2 + (1 - C^2) |QD|^2) \quad (4.7)$$

where C is the coherence factor that accounts for the coherence between the direct and reflected wave fields, as will be explained in section 4.3.4. The geometrical weighting factor D takes into account the strength of the image source with respect to the free field. In case of a flat ground this is defined by

$$D = \frac{p_{free}(S', R)}{p_{free}(S, R)} \text{ and } p_{free}(S, R) = \frac{1}{r(S, R)} e^{ikr(S, R)} \quad (4.8)$$

where S the position of the source, R the position of the receiver, S' the position of the image source, and $r(S, R)$ the length of the ray path from S to R . The spherical reflection coefficient Q takes into account phase shifts and amplitude changes of the reflected ray due to the reflection. In the case of a hard ground, Q is equal to 1.

Because of the surface properties of the ground, the parameters C , Q , and D can change for different ground segments. To overcome this problem, the two ray approximation model is applied to all ground segments separately. The total ground effect is calculated by means of a Fresnel weighting method of the contributions of each ground segment [19]

$$\begin{aligned} \Delta L_k &= 10 \log_{10} \left(|1 + C_k Q_k D_k|^2 + (1 - C_k^2) |Q_k D_k|^2 \right) \\ \Delta L_{G, \text{flat}} &= \sum_{k=1}^N w_k \Delta L_k, \end{aligned} \quad (4.9)$$

where the summation is over each ground segment and w_k is the Fresnel weighting factor of each ground segment. The Fresnel weighting method will be elaborated in more detail in section 4.3.2.

This model can be extended to also incorporate non-flat ground by making D_k dependent on different ground segments. For this, the quantities of D are calculated relative to an infinite supporting plane of each segment, meaning that the image source is calculated with respect to (an extension of) the segment that is considered.

However, over deep valleys, this model might become unstable. This can be solved by separating the coherent and incoherent parts of the reflected field [32]

$$\begin{aligned} \Delta L_{G, \text{valley}} &= 10 \log_{10} \left(\left| 1 + \sum_{k=1}^N w_k C_k D_k Q_k \right|^2 \right. \\ &\quad \left. + \sum_{k=1}^N w_k (1 - C_k^2) |D_k Q_k|^2 \right). \end{aligned} \quad (4.10)$$

Finally, the ground attenuation can be found as a weighted average combination of the flat formulation and the deep-valley formulation

$$\Delta L_{Gc} = F_G \Delta L_{G, \text{flat}} + (1 - F_G) \Delta L_{G, \text{valley}}, \quad (4.11)$$

where L_{Gc} is the ground attenuation for the concave model, $L_{G, \text{flat}}$ the attenuation by the formulation for flat terrain and $L_{G, \text{valley}}$ the attenuation by the valley shaped terrain.

The parameter F_G was derived from the fact that whether the flat or valley model should be used depends on the frequency. Therefore, the parameter F_G was found in [17] by comparison with numerical results. A correction was made in [30] to better represent the results in the case of a refracting atmosphere. In the end, F_G is defined as

$$F_G = 1 - e^{-1/x_g^2}, \quad (4.12)$$

with

$$\begin{aligned} x_g &= \frac{w_t}{\sqrt{1 + (f/f_c)^2}} \\ w_t &= \sum w_k \end{aligned} \quad (4.13)$$

where f_c is the transition frequency described in section 4.3.3. The summation to obtain parameter w_t is over all the ground segments.

4.3.2 Fresnel weights

The Fresnel weights are used to determine the contribution to the attenuation of each individual ground segment. This is necessary because the reflection of a sound wave does not only involve the ground at the specular point of reflection, but is also affected by the ground on either side of that point. The specular reflection point is the point of reflection between a source and receiver as found by considering the path of the reflected ray (see figure 4.4). The formulation is based on a Fresnel zone. The general idea of the use of a Fresnel zone was presented in [33]. They discovered that the excess attenuation is constant up to a certain distance from the source when looking at a two-impedance boundary problem for a single frequency and ignoring oscillations due to refraction. After that, a transition zone was identified until the results became constant again. This transition zone happens in a well-defined region around the specular reflection point. Consider the paths from the source to the receiver that involve a reflection somewhere on the boundary. The path is the shortest if this location on the boundary is the specular reflection point. Moving further away from this point increases the path's length. Hothersall and Harriot [33] defined the region where the transition of excess attenuation occurs as the point where the path length is greater by a value of $\lambda/3$ compared to the path length via the specular reflection point, this region is known as the Fresnel zone. The Fresnel zone is an ellipse for a 2D reflective surface area (see figure 4.5). This method was further developed in the NORD2000 project[17].

The implementation in the Harmonoise model of the Fresnel zone for a reflected ray path satisfies

$$r(S', P) + r(P, R) = r(S', R) + \lambda/n_F, \quad (4.14)$$

where λ is the wavelength, P the location of the specular reflection point and n_F is the Fresnel parameter. Thus, instead of using the value $\lambda/3$ as explained previously, the actual distance of the Fresnel zone is set as a parameter for further fine-tuning. Initially, n_F was set to 8. However, to yield more accurate results at higher frequencies, the modified Fresnel weights are calculated afterwards, which makes the parameter n_F frequency dependent. The Fresnel weights can be calculated through

$$w_{F,k} = F_w(\xi_2) - F_w(\xi_1), \quad (4.15)$$

with

$$F_w(\xi) = \begin{cases} 0 & \text{for } \xi \leq -1 \\ 1 - \frac{1}{\pi} \left(\cos^{-1}(\xi) - x\sqrt{1 - \xi^2} \right) & \text{for } -1 < \xi < 1 \\ 1 & \text{for } \xi \geq 1 \end{cases} \quad (4.16)$$

The variables ξ_1 and ξ_2 are computed as

$$\xi_m = \frac{d_m - d_F}{a}; \quad m = 1, 2 \quad (4.17)$$

where d_1 is the horizontal distance between the beginning of the ground segment and the source, d_2 is the horizontal distance between the source and end of the ground segment, d_F is the horizontal position along the x-axis of the center of the ellipse, and the size of the Fresnel ellipse along the x-axis is $d_F \pm a$. The parameters are also indicated in figure 4.5. The parameters are dependent on the source and receiver configurations and can be found as

$$d_F = \frac{d}{2} \left(1 + \frac{h'_s{}^2 - h'_r{}^2}{D^2 - d^2} \right). \quad (4.18)$$

where h'_s and h'_r are the source and receiver heights with respect to (an extension of) a ground segment. The value of a can be found as

$$a = \frac{1}{2} \sqrt{\frac{D^4 + (D_S^2 - D_R^2)^2 - 2D^2(D_S^2 + D_R^2)}{D^2 - d^2}}, \quad (4.19)$$

where

$$\begin{aligned} D &= \frac{\lambda}{n_F} + \sqrt{(h'_s + h'_r)^2 + d^2} \\ D_S^2 &= d_F^2 + h'_s{}^2 \\ D_R^2 &= (d - d_F)^2 + h'_r{}^2. \end{aligned} \quad (4.20)$$

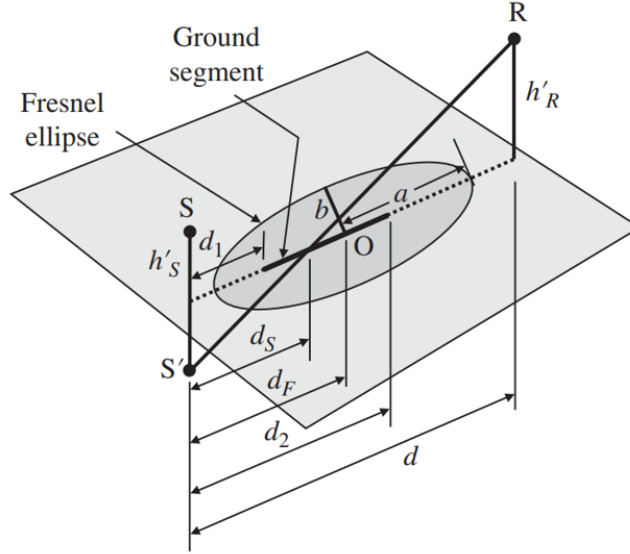


Figure 4.5: This figure shows the Fresnel ellipse with the parameters that are used in the formulation. Figure taken from [1].

These Fresnel weights yield accurate results at low frequencies but are less accurate at higher frequencies. To solve this the tuning parameter n_F is made frequency dependent and is calculated as [19]

$$n_F = 32 [1 - \exp(-f_c^2/f^2)]. \quad (4.21)$$

The modified Fresnel weights can still be calculated by equation 4.15 but now with modified arguments

$$w_k = F_w(\xi'_2) - F_w(\xi'_1), \quad (4.22)$$

with

$$\xi'_m = \frac{\xi_m - \xi_C}{1 - \xi_m \xi_C}, \quad (m = 1, 2) \quad (4.23)$$

$$\xi_C = \frac{d_C - d_F}{a}, \quad (4.24)$$

$$d_C = \alpha(f)d_F + (1 - \alpha(f))d_{SP} \quad (4.25)$$

$$d_{SP} = d_{SR} \frac{h_S}{h_S + h_R} \quad (4.26)$$

$$\alpha(f) = \left[1 + \left(\frac{f}{f_c} \right)^2 \right]^{-1}. \quad (4.27)$$

4.3.3 Transition frequency

The transition frequency is the frequency used for the transition between the low- and high-frequency models. It is also used to determine the transition between the flat and deep-valley models. It was found in [17] that the transition frequency between the low- and high-frequency models could be determined by the phase shifts from reflections of the softest ground surface between the source and receiver. The bounds of the transition region were identified as the lowest frequency for which the phase shift is $\frac{\pi}{2}$ and π for the lower and upper bound, respectively. The transition frequency is estimated as

$$f_c = \sqrt{f_{\min} f_{\max}}, \quad (4.28)$$

where f_{min} and f_{max} are the frequencies for which the following relationship holds:

$$\begin{aligned}\varphi_{\max}(f_{\min}) &= \frac{1}{2}\pi, \\ \varphi_{\max}(f_{\max}) &= \pi,\end{aligned}\tag{4.29}$$

The phase difference φ between the direct and reflected ray is defined as

$$\varphi_k(f) = \arg(Q_k) + k[r(S'_k, R) - r(S, R)],\tag{4.30}$$

where $\arg(Q_k)$ is the phase shift upon reflection, k is the wavenumber, $r(S'_k, R)$ the distance between the image source in the reference frame of segment k (see figure 4.4) and the receiver, and $r(S, R)$ is the distance between the real source and receiver.

The “max” subscript in equation 4.29 stands for the largest phase shift difference of all ground segments k . The values of f_{min} and f_{max} are found from equation 4.29 and 4.30 by linear interpolation between the 1/3 octave band center frequencies

$$f_{\max} = f_{n-1} + (f_n - f_{n-1}) \frac{\pi - \varphi(f_{n-1})}{\varphi(f_n) - \varphi(f_{n-1})}.\tag{4.31}$$

where f_n is the center frequency just above π . The same can be done for f_{min} but with π replaced by $\pi/2$. If $n = 1$, f_{min} is set as f_n .

4.3.4 Coherence factor

The coherence factor takes into account the fluctuations in phase difference between rays. When rays have a constant phase difference with changing distance, they can be regarded as coherent. When the phase difference changes, the rays are incoherent with each other. Coherent addition of waves means that the phase is taken into account within the addition, and thus constructive and destructive interference will take place. Incoherent addition simply means summing up the squared amplitudes of a wave, disregarding the phase [24]. The Harmonoise model considers coherence in terms of the coherence factor; if the coherence factor is 1, the rays are summed up as perfectly coherent. If the coherence factor is 0, the phase is summed using incoherent addition. The Harmonoise model only considers the coherence between the direct ray and the reflections, not the coherence between several reflections.

The coherence factor C is calculated as [30]

$$C = \exp\left(-\frac{1}{2}\sigma_\varphi^2\right)\tag{4.32}$$

where σ_φ is the standard deviation of the phase difference fluctuation. This standard deviation consists of the standard deviation of the uncertainty of the distance between source and receiver (σ_d), the standard deviation of the uncertainty of the source and receiver height (σ_{h_s} and σ_{h_r}) and the standard deviation of the uncertainty of the 1/3 octave band averaging (σ_f). The total standard deviation can be calculated by

$$\sigma_\phi^2 = \phi^2 \left[\left(\frac{\sigma_f}{f}\right)^2 + \left(\frac{\sigma_d}{d}\right)^2 + \left(\frac{\sigma_{h_s}}{h_s}\right)^2 + \left(\frac{\sigma_{h_r}}{h_r}\right)^2 \right]\tag{4.33}$$

where

$$\phi = k\Delta d = \frac{2\pi f}{c_0} \frac{2h_s h_r}{d}.\tag{4.34}$$

The term that accounts for the 1/3 octave frequency band averaging is calculated by

$$\frac{\sigma_f}{f} = \frac{1}{3} \frac{\Delta f}{f} = \frac{1}{3} \left(2^{B/2} - 2^{-B/2}\right)\tag{4.35}$$

where $B = 1/3$ for 1/3 octave band averaging. The remaining terms σ_d , σ_{h_s} and σ_{h_r} account for the uncertainty in distance between source and receiver, uncertainty in source height, and uncertainty in

receiver height, respectively. In absence of better information the following values for the standard deviations can be used [1, 19]

$$\begin{aligned}\frac{\sigma_d}{d} &= 0 \\ \frac{\sigma_{h_s}}{h_s} &= \min\left(1, \frac{h_s}{10}\right) \\ \frac{\sigma_{h_r}}{h_r} &= \min\left(1, \frac{h_r}{10}\right).\end{aligned}\tag{4.36}$$

The simulations in section 5.1 and chapter 6 use the standard deviations of equation 4.35 and 4.36.

4.4 Refraction

The Harmonoise model explained thus far is only considering a non-refracting atmosphere. Harmonoise incorporates refraction by applying a conformal mapping that transforms ray paths into approximately straight lines. The new problem can then be solved with the models introduced in the previous sections. This method is referred to as the ‘‘curved ground analogy.’’ To transform the ray paths into straight lines, the assumption is made of a linear sound speed profile, resulting in all ray paths being described by a circular arc. The radius of this arc is described by [1]

$$R = \frac{c}{g \cos \theta},\tag{4.37}$$

where c is the speed of sound, g is the gradient of the sound speed, and θ is the elevation angle as denoted in figure 4.6.

In reality, the sound speed profile is not linear. To approximate the ray paths as well as possible, the sound speed profile is linearized, taking into account the maximum ray height.

This section will first introduce the concept of the curved ground analogy, then explain the conformal mapping of the Harmonoise model, and finally address the linearization done by Harmonoise. Additional information about conformal mappings can be found in Appendix F.

4.4.1 Curved ground analogy

In acoustics, it can be difficult to correctly reconstruct propagation conditions in laboratories. For example, it is hard to mimic sonic gradients without the use of wind tunnels. A possible method to simulate the correct propagation conditions without the construction of a sonic gradient is by curving the ground in the same manner as the rays originally would. The curvature of the ground can be chosen as the same curvature a ray would have in the case of a constant vertical sonic gradient. For an engineering model such as the Harmonoise model, it is difficult to incorporate refraction analytically. The use of the curved ground analogy is a convenient method to include refraction but still use the analytical models that are based on straight ray paths.

As shown in equation 4.37, the ray radius is dependent on the elevation angle. For near horizontal propagation, the ray radii are very similar. One ray has to be chosen as the ground curvature. In the Harmonoise model, the direct ray between source and receiver is chosen for this. Figure 4.6 illustrates the curved ground analogy for a downward-refracting atmosphere.

The new situation correctly simulates the ground effect if:

- angles at the reflection interface are preserved.
- phase differences between rays are preserved.

The angles are preserved in the case of a conformal mapping, but the lengths and thus the phase difference is not. Almgren [34] conducted a theoretical and numerical study with the sound-ray approximation. He showed that the phase difference is not preserved but remains close to the original phase difference in situations important for outdoor sound prediction, e.g., small elevation angles. In other words, the ray path lengths change in such a way that the difference in path length between the rays remains relatively close to the original problem. Consider the equation for phase shift

$$\phi = k\Delta r,\tag{4.38}$$

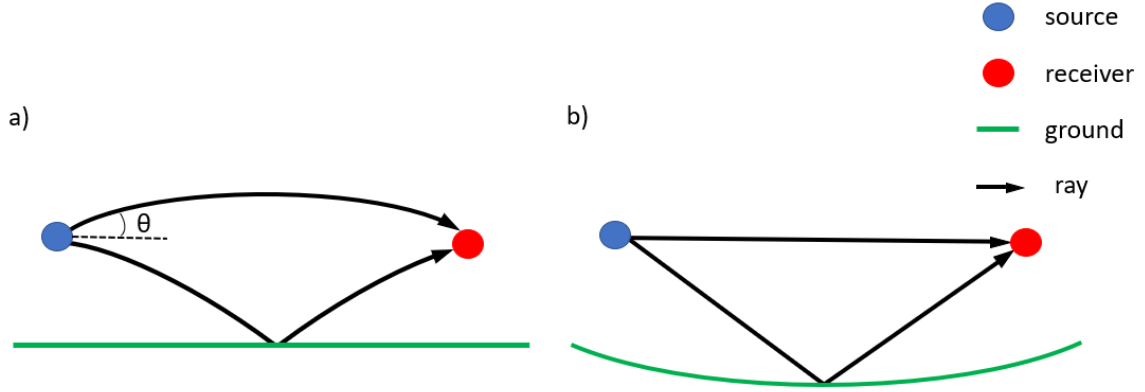


Figure 4.6: a) Sound rays between source and receiver in case of a downward-refracting atmosphere. b) Curved ground analogy that represents situation a. The curvature of the ground is chosen as the limiting ray.

where Δr is the difference in path lengths between rays. This implies that a similar difference in path length results in a similar phase difference. The curved ground analogy is what the Harmonoise model uses to simulate refraction.

4.4.2 Conformal mapping in the Harmonoise model

Refraction is taken into account by a conformal mapping, using the curved ground analogy. It is assumed that the speed of sound can be described by a constant gradient, resulting in

$$c(z) = c_0 \left(1 + \frac{z}{R}\right), \quad (4.39)$$

where z is the height above the ground and c_0 is the speed of sound at $z = 0$.

Consider the following conformal mapping [30]

$$\zeta = u + iv = \frac{iRw}{w + 2iR}, \quad (4.40)$$

with $w = x + iz$ and R being the radius of the circle of the ray path. This transformation maps circular ray paths through the origin, $w(0, 0)$, to straight lines. The effects of this transformation can be seen by applying the transformation of equation 4.40 on the original wave equation [30]

$$\frac{\partial^2 p}{\partial x^2} + \frac{\partial^2 p}{\partial z^2} - \frac{1}{c(z)^2} \frac{\partial^2 p}{\partial t^2} = q(t)\delta(x)\delta(z), \quad (4.41)$$

which transforms into

$$\frac{\partial^2 p}{\partial u^2} + \frac{\partial^2 p}{\partial v^2} - \frac{1}{c(u, v)^2} \frac{\partial^2 p}{\partial t^2} = q(t)\delta(u)\delta(v), \quad (4.42)$$

with

$$c(u, v) = c_0 \left(1 + \frac{u^2 + v^2}{4R^2}\right) \quad (4.43)$$

Equation 4.43 is a radial function of space, thus rays are straight lines. For short propagation distances, the speed of sound can be considered constant, $c(u, v) = c_0$. At a certain distance, the term $\frac{u^2 + v^2}{4R^2}$ can not be neglected anymore. A condition for the validity of this approximation is $\frac{d}{R} < 0.2$ from the work in [30].

The conformal mapping used in the Harmonoise model is slightly different but based on the same principle:

$$w = x + iz \quad \rightarrow \quad w' = x' + iz' \quad (4.44)$$

$$w' = \frac{C(w - w_0)}{C + (w - w_0)} \quad (4.45)$$

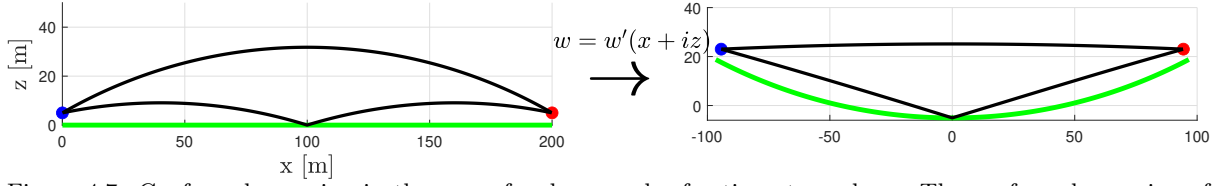


Figure 4.7: Conformal mapping in the case of a downward refracting atmosphere. The conformal mapping of equation 4.44 is used.

with,

$$w_0 = \frac{x_0 + x_N}{2} + i \frac{z_0 + h_s + z_N + h_r}{2}, \quad (4.46)$$

$$C = iC_0 \quad (4.47)$$

$$C_0 = 2 \left(\frac{h_s + h_r}{2} + R \right), \quad (4.48)$$

where x_0 is the x coordinate of the ground segment below the source, x_N is the x coordinate of the ground segment below the receiver, z_0 is the z coordinate of the ground below the source and z_N is the z coordinate of the ground below the receiver. This mapping transforms ray paths through the origin $w = w_0 - C$ to straight paths. Other circular ray paths are mapped to circles, but they are very large circles such that they approximate straight ray paths.

To illustrate the mapping of equation 4.44, consider two rays between a source and receiver in the case of a downward refracting atmosphere with a flat ground, as shown at the left of figure 4.7. This situation is mapped to the one on the right, where the rays are approximately straight. The rays are not completely straight because they do not go through the origin and are therefore mapped to a large circle.

4.4.3 Linearization

Only linear sound speed profiles can be used in the Harmonoise model to guarantee that rays follow circular pathways, allowing analytical approximations. However, linear-logarithmic profiles are a better fit for reality. In order to address this, Harmonoise linearizes lin-log profiles in a way that produces results that are as similar as possible to the ones obtained with the lin-log function. This is predicated on the requirement that a ray path passes through the source, receiver, and the sound ray's highest point [19].

A lin-log profile is used to approximate realistic wind profiles

$$c(z) = c_0 + Az + B \log \left(1 + \frac{z}{z_0} \right), \quad (4.49)$$

where A [1/s] is the linear part parameter, B [m/s] is the logarithmic part parameter, and z_0 [m] is the roughness length. A methodology to calculate these parameters using the Monin-Obukhov similarity theory is described in Appendix C. Harmonoise divides the contributions of the linear and logarithmic part by calculating the radius of the ray from the linear part and the logarithmic part separately. Afterwards, these radii are combined as follows [35]

$$\frac{1}{R} = \frac{1}{R_A} + \frac{1}{R_B}, \quad (4.50)$$

where R_B is the radius because of the logarithmic part and R_A the radius of the linear part. The linear part can be found as

$$\frac{1}{R_A} = \frac{A}{c_0}. \quad (4.51)$$

The logarithmic part R_B is determined by the conditions that a ray needs to go through the source, receiver, and highest point of the ray. The highest point of a ray can be estimated by [1, 13]

$$h_{max} = d \sqrt{\frac{B}{2\pi c_0}}, \quad (4.52)$$

where d is the horizontal distance between source and receiver. This ray path is replaced with a circular ray path with radius R and $z = -R_B$ as position of the center of the circle below ground level, which is set at $z = 0$. The height for this circular ray path can be obtained by

$$h_{max} = R - R_B. \quad (4.53)$$

The horizontal distance can be found as

$$d = 2\sqrt{R^2 - R_B^2}. \quad (4.54)$$

Substituting equation 4.53 and 4.54 in equation 4.52 results in

$$\frac{R}{R_B} = \gamma = \frac{1 + 4K^2}{1 - 4K^2}, \quad (4.55)$$

with $K = \sqrt{\frac{B}{2\pi c_0}}$. The value K is only dependent on the parameter of the logarithmic part B . The equivalent linear part can now be identified as

$$c(z) \approx c_0 \left(1 + \frac{z}{R_B}\right). \quad (4.56)$$

Finally the equivalent linear part of the lin-log profile is approximated as

$$c(z) \approx c_0 \left(1 + \frac{z}{R}\right). \quad (4.57)$$

In the derivation above, d is taken as the distance between the intersections of the ray path with the ground. For low sources, this is close to the distance between source and receiver, but for higher sources, this approximation is not valid anymore. Therefore, this linearization of the logarithmic part is only valid for low sources. Hansen et al. [1] and de Roo et al. [35] generalized the derivation to also include the possibility of high sources and found the logarithmic part as

$$\frac{1}{R_B} = \frac{\sqrt{B^2 - AC} - B}{C}, \quad (4.58)$$

where $A = 1 + \text{tg}^2 \theta - \gamma^2$, $B = h_M (1 + \text{tg}^2 \theta)$ and $C = h_M^2 (1 + \text{tg}^2 \theta) + (r/2)^2$. With $\text{tg} \theta = \frac{h_r - h_s}{d_{SR}}$, $h_M = \frac{h_s + h_r}{2}$, $d = \sqrt{d_{SR}^2 + (h_s - h_r)^2}$, $\gamma = (1 + 4K^2) / (1 - 4K^2)$ and $K = \sqrt{b / (2\pi c_0)}$. Figure 4.8 shows the meaning of the parameters θ and h_M . The actual distance between the source and receiver is represented by r , while the horizontal distance is represented by d_{SR} .

Figure 4.9 illustrates the linearization of a random sound speed profile in the case of a low source and in the case of a high source. The exact values used for this example can be found in the caption. It clearly shows that for a high source, the gradient of the equivalent linear profile is taken from a higher altitude, and for a low source, the relevant region is the gradient at a lower altitude. Note that the actual value of the speed of sound is not important, but the gradient is used for the conformal mapping.

4.5 Assumptions used in the Harmonoise model

Because analytical models are used, the Harmonoise model has a very low computation time. It is only possible to avoid iterations and a large computational cost by making assumptions about many significant propagation effects. Therefore, using Harmonoise in a particular situation requires careful evaluation of a number of fundamental hypotheses. These hypotheses are recalled here below:

- The conformal mapping assumes constant sound speed which is only a valid approximation if the condition $d/R < 0.2$ is met. To illustrate this constraint suppose that a problem with a linearized sonic gradient of 0.05 1/s has to be solved, which is a large but realistic gradient. By using equation 4.51 this gradient corresponds to a ray path radius of 7800 m. Using the condition of $d/R < 0.2$ indicates that the maximum propagation distance where the results can be regarded accurate is 1560 m, a lower sonic gradient would increase this number.

- The Harmonoise model does not account for multiple ray reflections. The model should not be applied in circumstances where the receiver receives multiple ground reflections.
- Only 1/3 octave band analysis is supported by the Harmonoise model. Coarser bands like standard octave bands are also viable [1]. The accuracy of bands smaller than 1/3 octave should be evaluated first, as it may be insufficient.
- The Harmonoise model is only valid for point sources. However, this limitation could be overcome as explained in [1].
- Actual sonic profiles are approximated by lin-log profiles. Furthermore, lin-log profiles are linearized to ensure that ray paths are circular arcs.
- It is assumed that the sonic gradient is only a function of height so that no horizontal gradient is present. In chapter 7 a method is proposed to overcome this problem.

The implications of these limitations will be explored in the next chapters.

Chapter 5

Matlab implementation and validation

The Harmonoise model as described in chapter 4 was implemented as Matlab code. This implementation will be validated in the next section and, after that, its validity for wind turbine sound propagation cases is discussed.

The Harmonoise model calculation scheme is visualized in terms of the roadmap shown in figure 5.1. The roadmap consists of three branches: one for the geometrical spreading, one for the atmospheric absorption, and one for the ground attenuation.

The input parameters for the Harmonoise model are summarized in table 5.1.

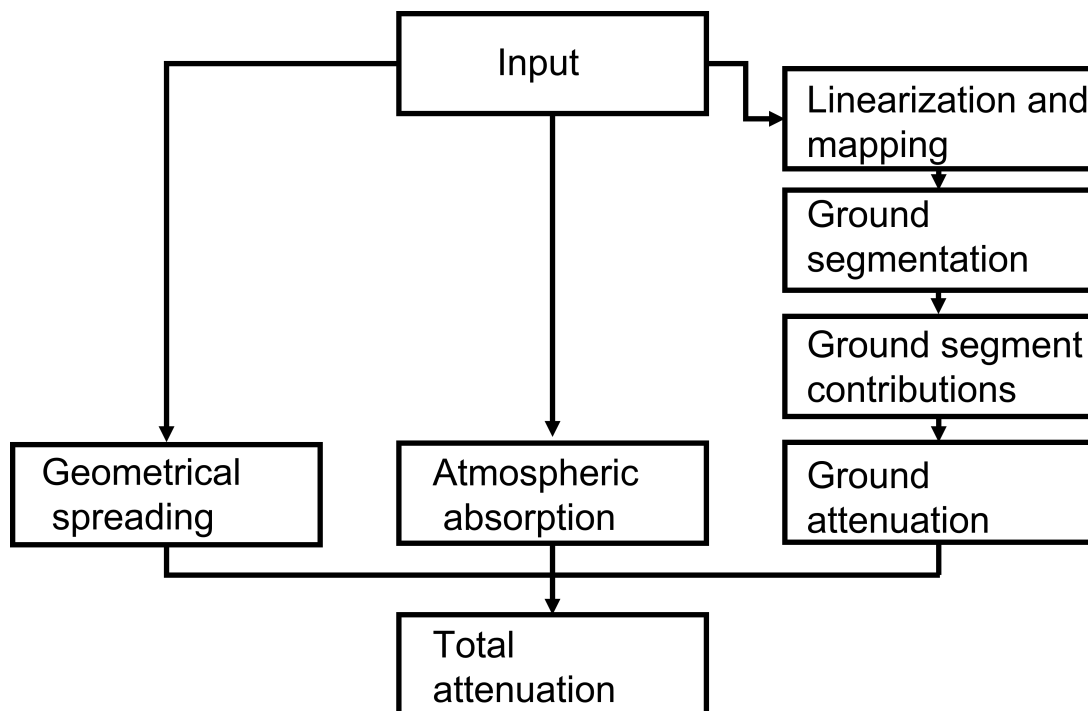


Figure 5.1: Calculation scheme of the Harmonoise model.

Table 5.1: Input parameters of the Harmonoise model.

<i>Input parameters</i>	<i>Description</i>
h_s	Source height [m]
h_r	Receiver Height [m]
(x, z)	Coordinates of ground profile. The source is placed above x_0 and the receiver above x_N .
N	Amount of straight segments used for segmentation of the ground
A	Linear part of sound speed profile [1/s]
B	Logarithmic part of sound speed profile [m/s]
z_0	Roughness length [m]
T_0	Ambient atmospheric temperature [K]
h_{rel}	Relative humidity [%]

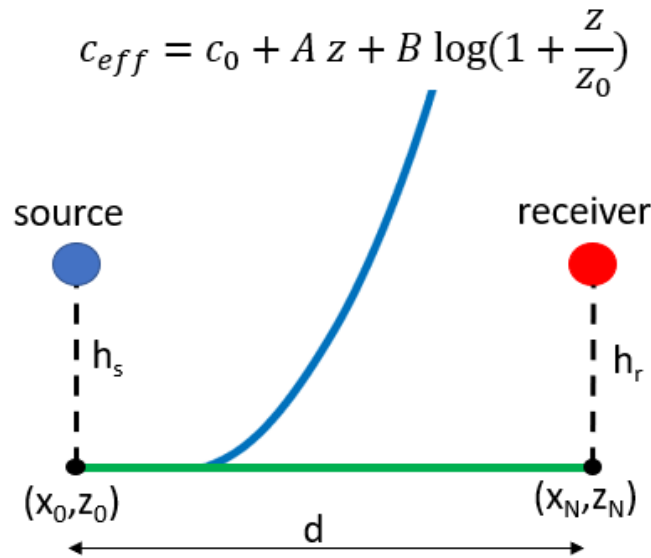


Figure 5.2: Geometry for validation of the Harmonoise code. The blue line depicts the effective speed of the sound profile that varies only with height.

5.1 Validation

To confidently use the implemented Harmonoise model, the code should be validated. The effect of geometrical spreading was easily defined as correct by comparing the result with other free field pressures. The validation of the attenuation by atmospheric absorption was done by comparing absorption values with available values presented in [36]. The ground attenuation will be validated in the subsequent section for several cases. This is accomplished using a combination of analytical results, more accurate results obtained by solving parabolic equations, and another Harmonoise code.

Cases with a flat, acoustically hard ground surface in the presence of different sound speed profiles are used to validate the Harmonoise code. Figure 5.2 shows the geometry used for all the validation cases. In the next sections, this geometry will be used with different values of h_s , h_r , d , A and B . In all cases $z_0 = 0.1$ m, $c_0 = 340$ m/s and $N = d/5$.

There are four steps involved in the validation of ground attenuation. The first step involves a comparison between the ground attenuation of the Matlab code and the output of the Harmonoise code implemented by the Centre Scientifique et Technique du Bâtiment (CSTB). The results should be the same in this case.

Following that, reference results are generated using the GFPE solver ATMOS of the CSTB (details can be found in Appendix E). These reference results will be used to validate the Harmonoise model for different cases where analytical results are not obtainable. To get an indication of the accuracy of the reference results and to select appropriate parameters for the GFPE solver, results from the GFPE solver

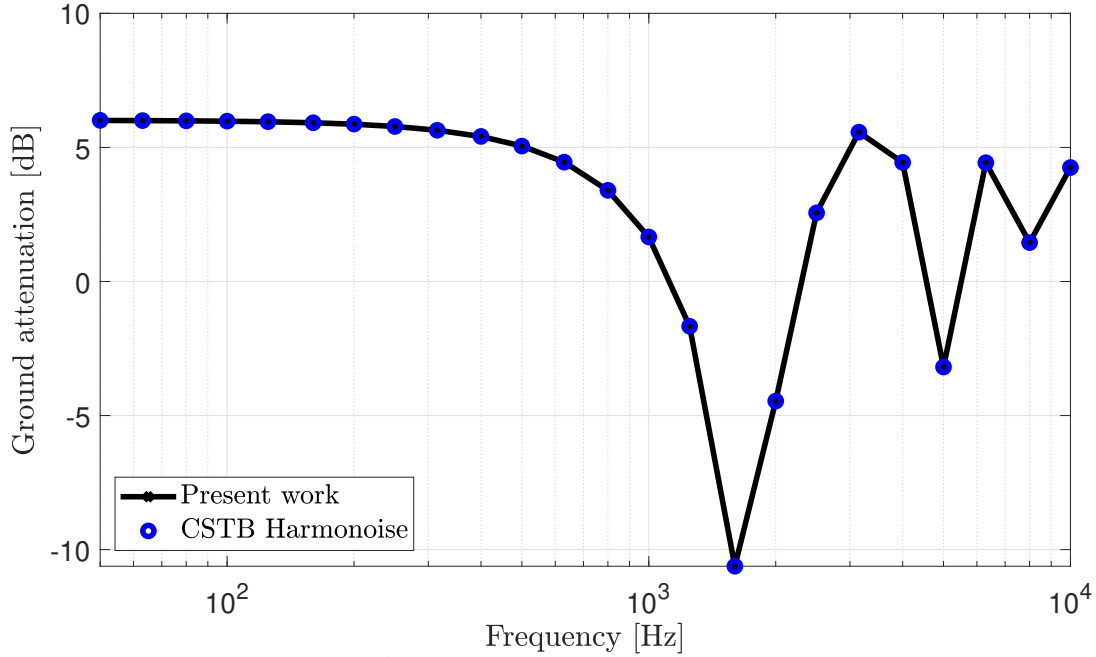


Figure 5.3: Ground attenuation of case A_1 calculated with the implemented Matlab Harmonoise code and with the CSTB in-house code. The results are presented in the $1/3$ octave band spectrum.

are first computed for simple cases where an analytical solution is possible with several computational grid sizes. These results are then compared with the corresponding analytical solution to determine the appropriate computational grid size.

Then, the attenuation in the case of a low source and low receiver is considered. This instance is compared with the reference results generated by the GFPE solver. Next, the same is done for a high source and a low receiver.

After all four validation steps, the Harmonoise model's potential application to noise simulations of wind turbines is examined.

5.1.1 Validation of Matlab implementation

The MATLAB implementation of the Harmonoise model is validated against the CSTB implementation of the Harmonoise model. A model for diffraction edges is not implemented in the Matlab version; thus, a case has to be chosen that does not have any diffraction edges. This is the case for the setup shown in figure 5.2. The following parameters for two cases were chosen:

Case A_1 : $A = 0$, $B = 0$, $h_s = 0.75$ m, $h_r = 5$ m, $d = 75$ m with a flat acoustically hard ground profile

Case A_2 : $A = 0.2$, $B = 0$, $h_s = 0.75$ m, $h_r = 5$ m, $d = 75$ m with a flat acoustically hard ground profile

The attenuation due to the ground reflection for the two cases are presented in figure 5.3 and 5.4 respectively. It can clearly be seen that the results almost perfectly overlap for both cases. The actual differences are displayed in figure 5.5 for case A_1 and in figure 5.6 for case A_2 . The differences in case A_1 are very small and can be due to rounding errors. However, the differences for case A_2 are a bit larger, especially near the minimum for 1200 Hz. This difference can be explained by small differences between the CSTB code and the Harmonoise model as presented in the original papers. However, the differences can still be considered negligible, and therefore the implementation of the Matlab version is regarded as good.

5.1.2 Evaluating the accuracy of ATMOS

The parabolic equation solver ATMOS (see Appendix E) is used to obtain accurate reference solutions. Computations of ATMOS with several grid spacings are compared in two different cases to determine if the chosen computational space is appropriate. The two cases are both for a non-refracting atmosphere

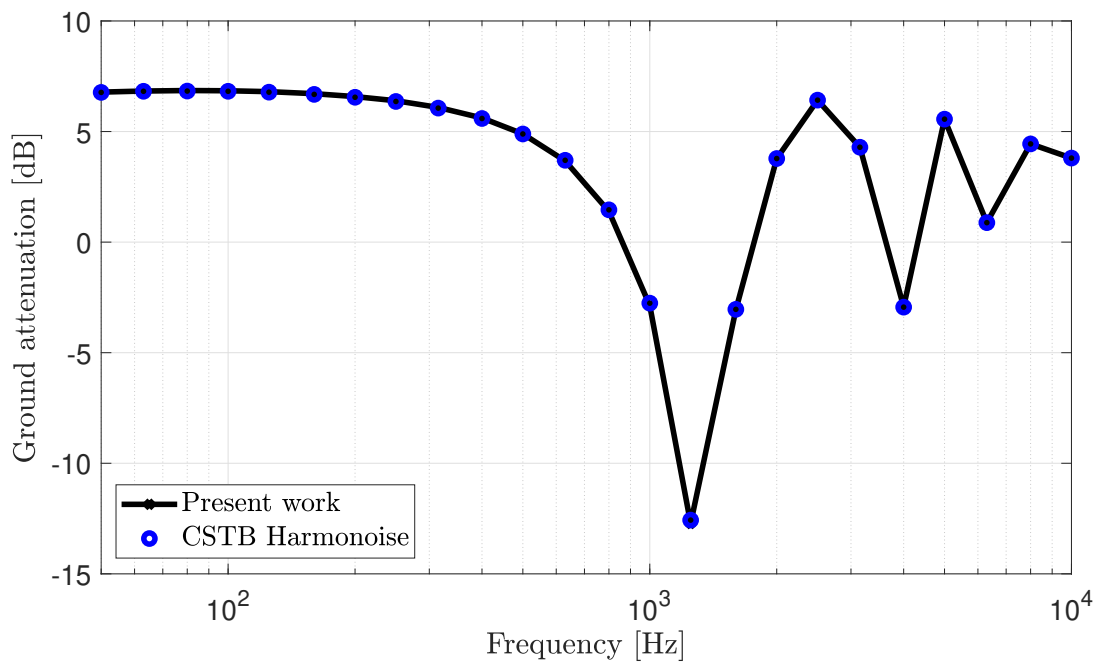


Figure 5.4: Ground attenuation of case A₂ calculated with the implemented Matlab Harmonoise code and with the CSTB in-house code. The results are presented in the 1/3 octave band spectrum.

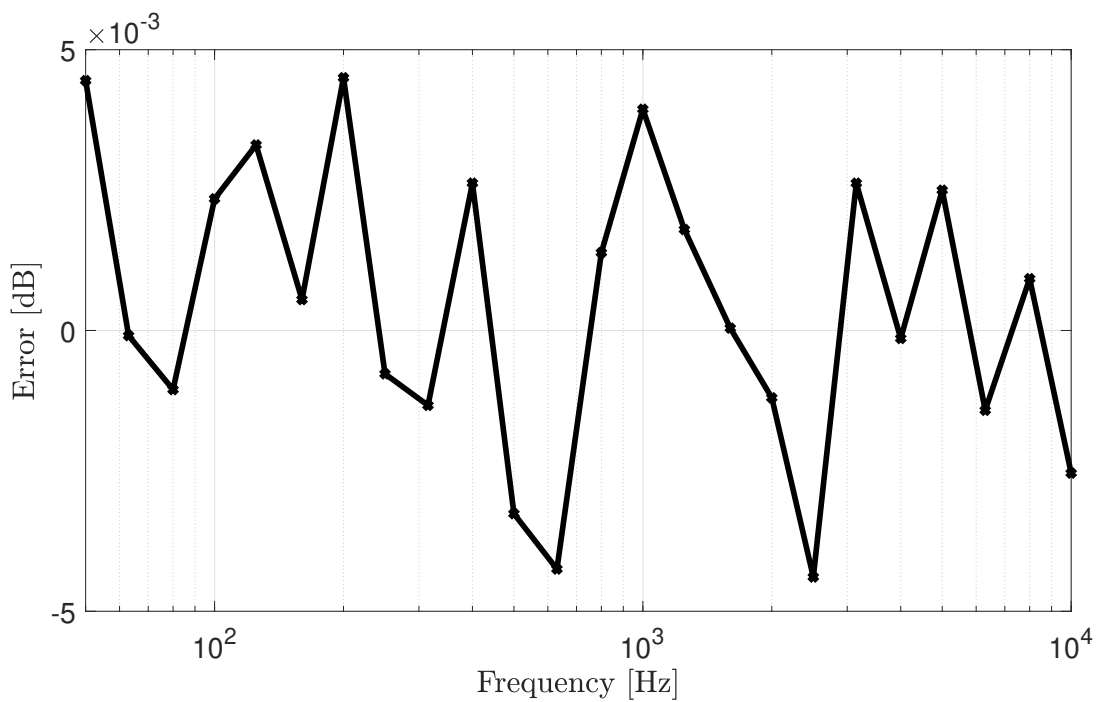


Figure 5.5: The difference for case A₁ between the Harmonoise code implemented in Matlab and the in-house Harmonoise code of the CSTB.

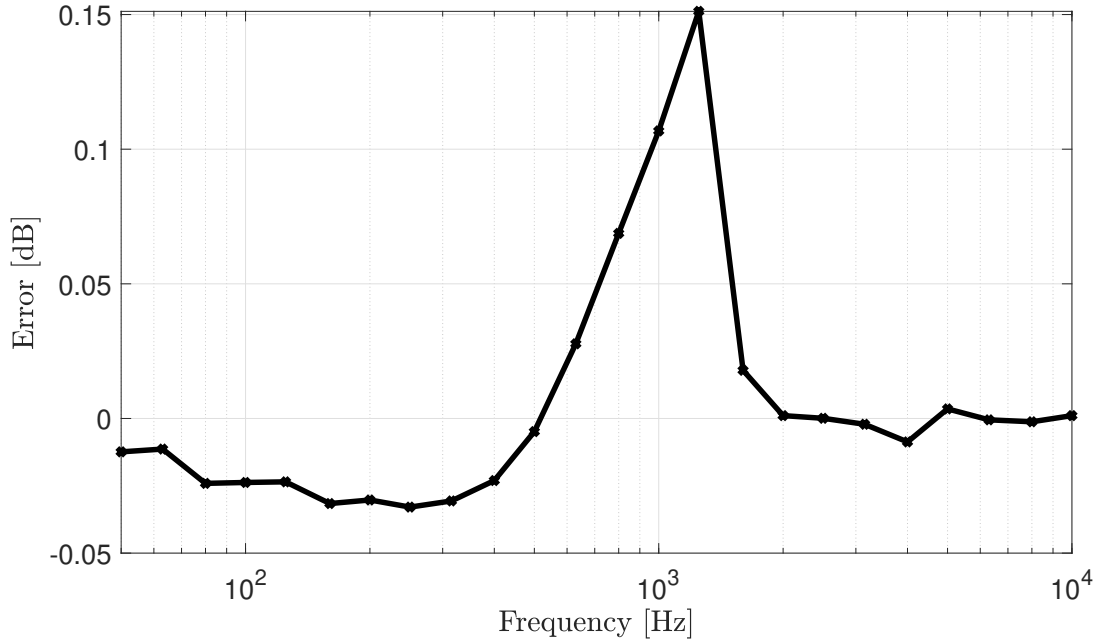


Figure 5.6: The difference for case A_2 between the Harmonoise code implemented in Matlab and the in-house Harmonoise code of the CSTB.

and a fully reflecting ground, since the ground attenuation can be analytically determined in that case. The parameters of the cases are:

Case B_1 : $A = 0$, $B = 0$, $h_s = 0.75$ m, $h_r = 5$ m, $d = 75$ m with a flat acoustically hard ground profile

Case B_2 : $A = 0$, $B = 0$, $h_s = 80$ m, $h_r = 1.5$ m, $d = 1200$ m with a flat acoustically hard ground profile

The first case determines the error for short propagation distances with a low source, and the second case for a high source and a long propagation distance. The analytical solution is obtained as described in Appendix B. In the calculations, 10 frequencies are used per 1/3 octave band for averaging. Since computational times would be too large otherwise, the two cases are calculated up to 1000 Hz.

Figure 5.7 and 5.8 show the ground attenuation for the two cases respectively. All results are very close to the analytical solution. The error, calculated as the difference between the analytical solution and ATMOS' solution, is presented in figure 5.9 and 5.10. The coarsest grid, $dx = \lambda/1$, $dz = \lambda/20$, has a relatively large error at higher frequencies for both cases. The other two grids perform similarly. The maximum error for the first case is about 0.07 dB and for the second case 0.6 dB. This error is only that large in local minima, and therefore the results can be considered accurate enough. Because the grid size $dx = \lambda/3$, $dz = \lambda/60$ and the grid size $dx = \lambda/6$, $dz = \lambda/120$ produce similar results, the coarsest grid between the two is chosen. Thus, the grid size that is chosen for the generation of reference results is $dx = \lambda/3$, $dz = \lambda/60$.

5.1.3 Validation for low sources

In the next part, the Harmonoise model implemented in Matlab will be compared to a reference solution generated by the GFPE solver ATMOS in case of a low source and a short propagation distance. ATMOS is a more accurate method than the Harmonoise model. Thus, the comparison between the Harmonoise model and ATMOS gives an indication of the accuracy of the Harmonoise model. Three types of sound speed profiles are considered: a linear profile, a logarithmic profile, and a linear-logarithmic (lin-log) profile. The parameters of the cases are:

Case C_1 : $A = 0.2$, $B = 0$, $h_s = 0.75$ m, $h_r = 5$ m, $d = 75$ m with a flat acoustically hard ground profile

Case C_2 : $A = 0$, $B = 1$, $h_s = 0.75$ m, $h_r = 5$ m, $d = 75$ m with a flat acoustically hard ground profile

Case C_3 : $A = 0.1$, $B = 0.5$, $h_s = 0.75$ m, $h_r = 5$ m, $d = 75$ m with a flat acoustically hard ground profile

The results for case C_1 , the case with the linear sound speed profile, are presented in figure 5.11. The figure shows the ground attenuation by the two different models. The overall agreement is good. The

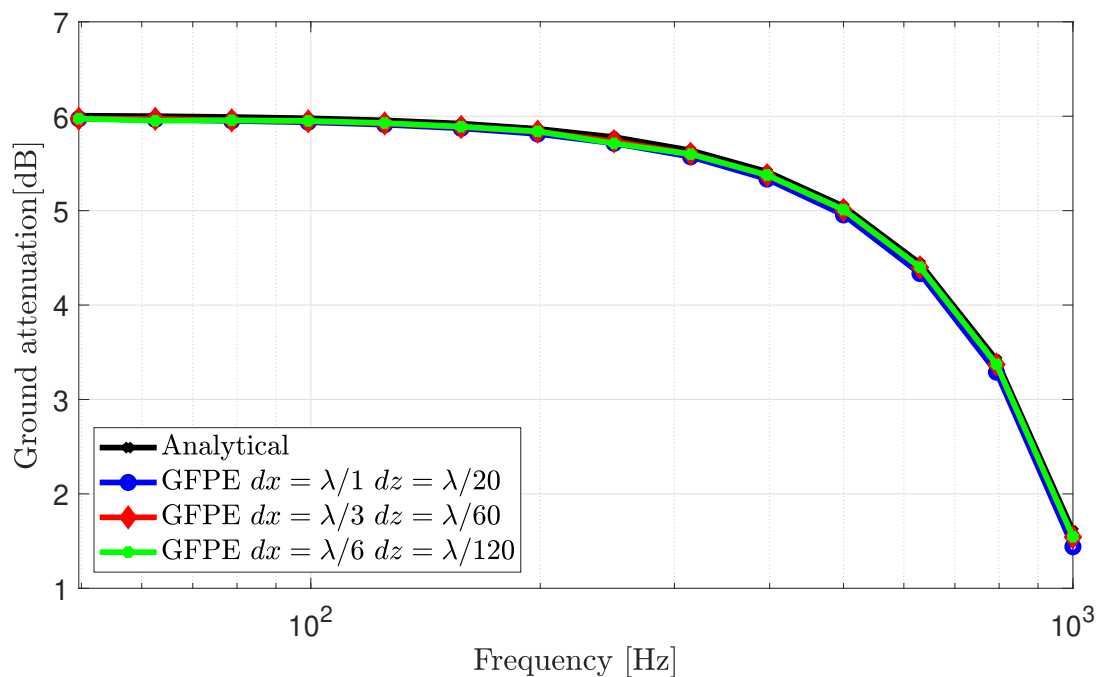


Figure 5.7: Results of ATMOS (a GFPE solver) for different grid spacings compared to an analytical solutions for case B₁.

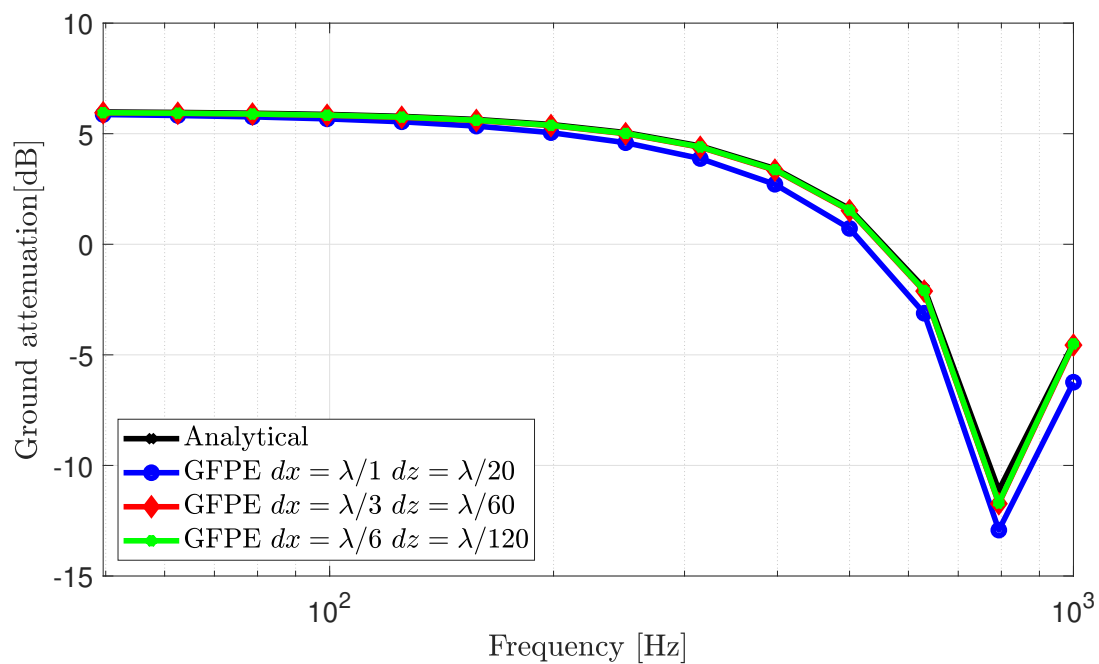


Figure 5.8: Results of ATMOS (a GFPE solver) for different grid spacings compared to an analytical solutions for case B₂.

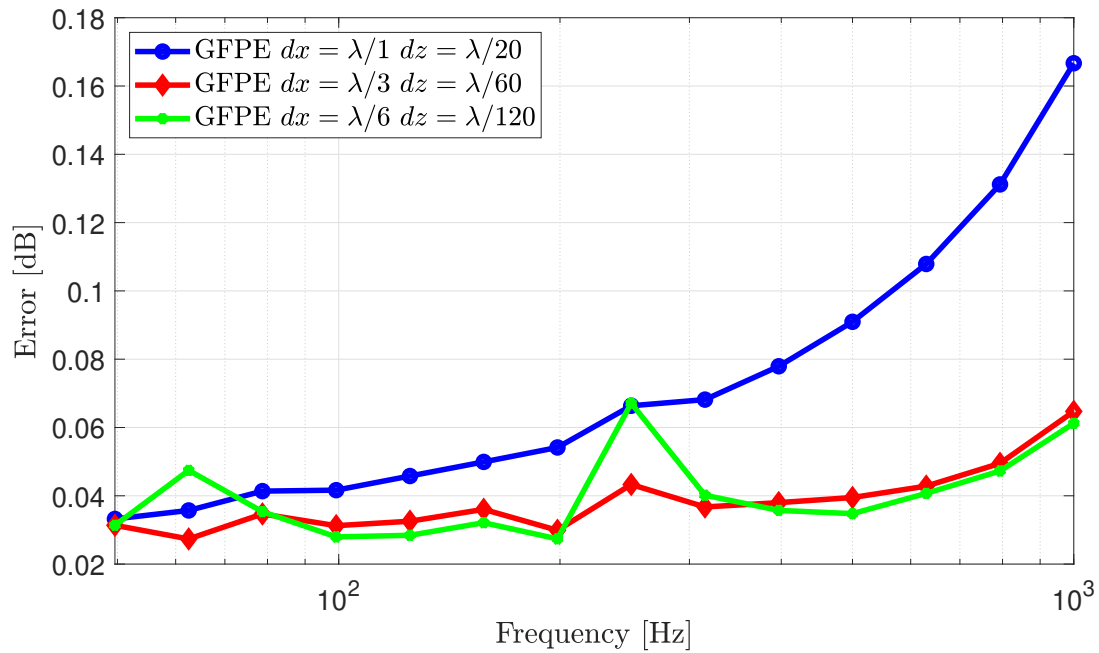


Figure 5.9: The difference between the analytical solution and ATMOS with different grid spacings for case B₁.

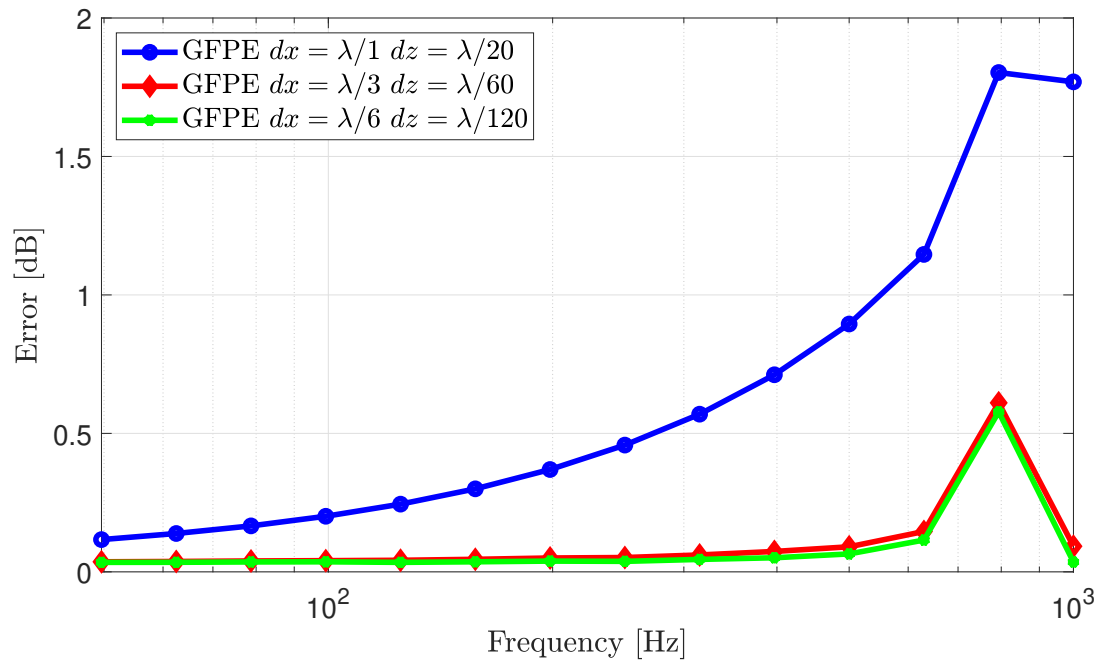


Figure 5.10: The difference between the analytical solution and ATMOS with different grid spacings for case B₂.

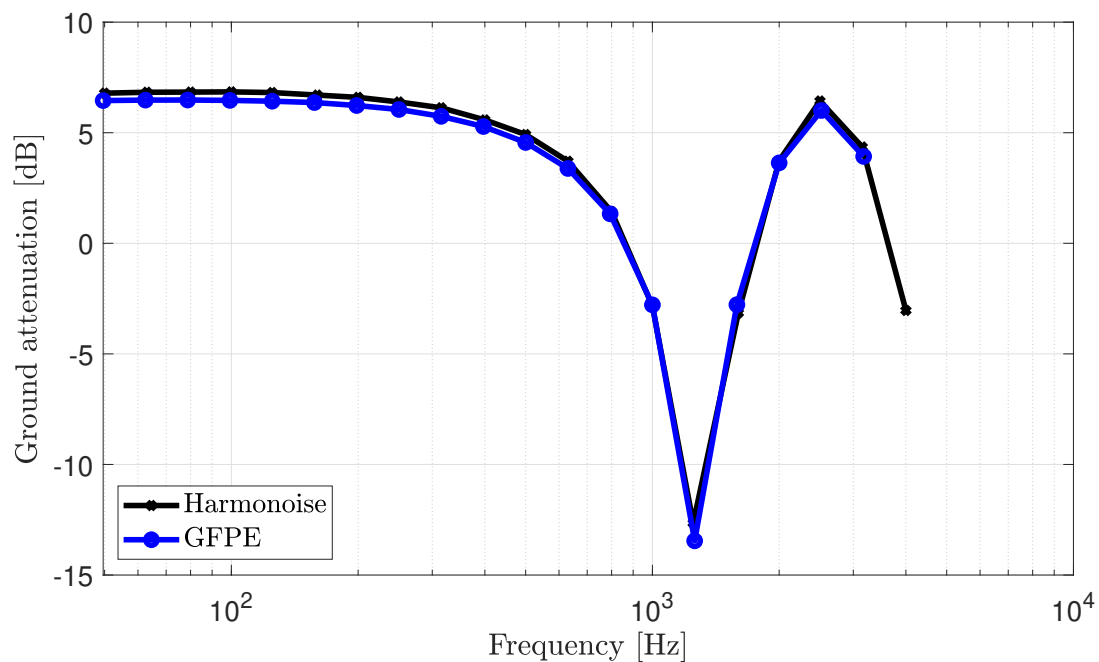


Figure 5.11: Ground attenuation of case C_1 calculated with ATMOS (a GFPE solver) and the Harmonoise model. This case illustrates the difference between ATMOS and Harmonoise. The results are presented in the 1/3 octave band spectrum.

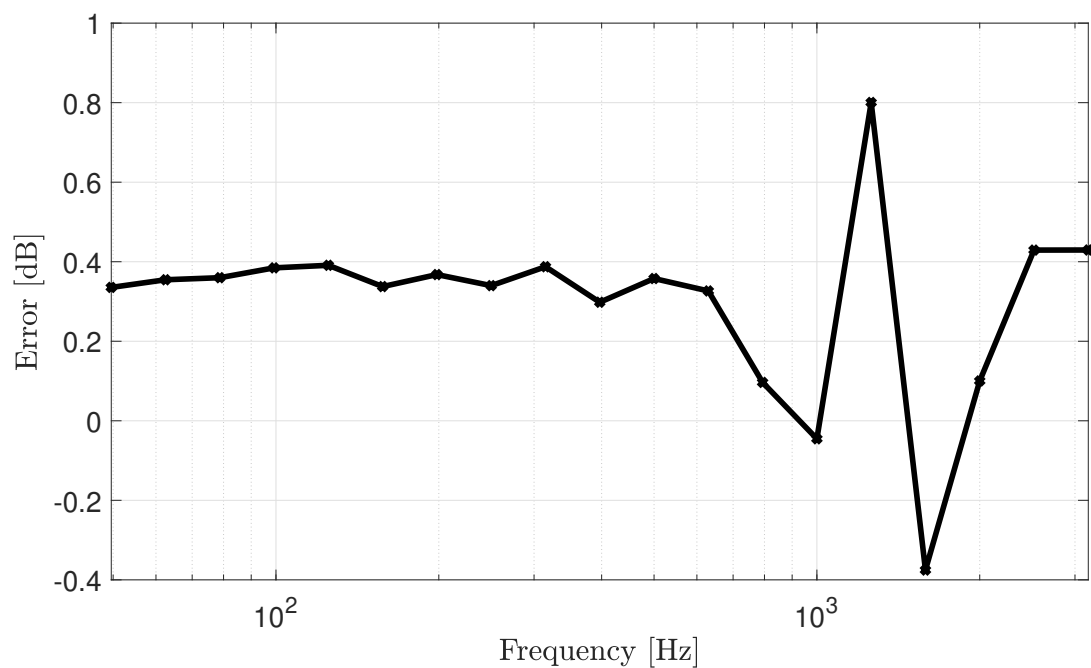


Figure 5.12: The difference between the ground attenuation obtained with ATMOS and the Harmonoise model for case C_1 .

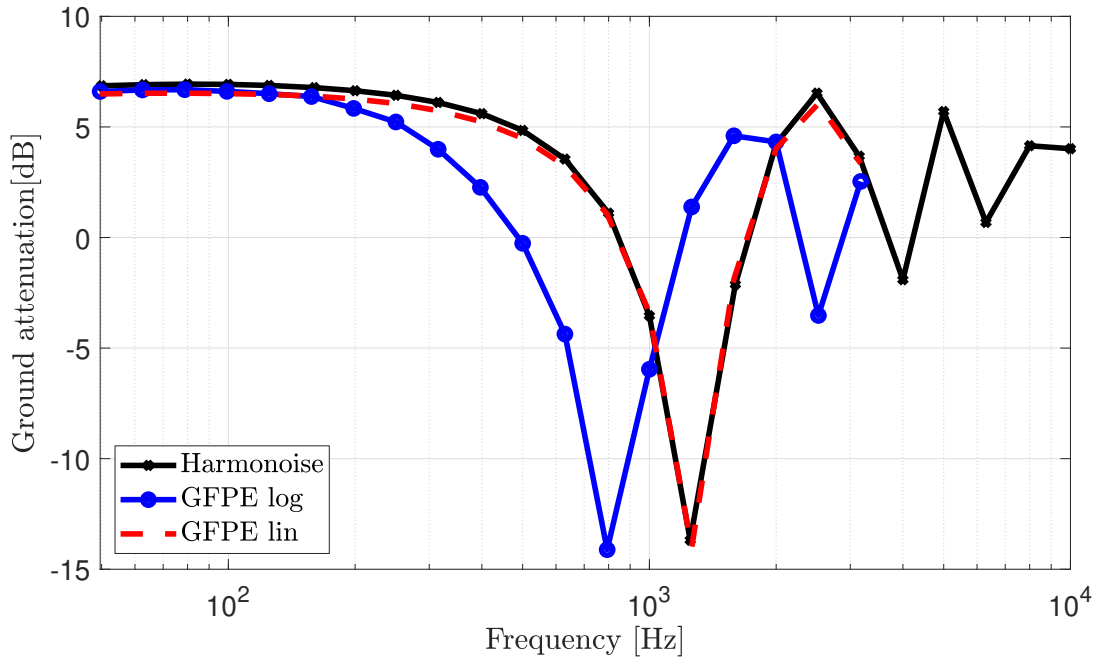


Figure 5.13: Ground attenuation of case C_2 calculated with ATMOS (a GFPE solver) and the Harmonoise model. This case is a reference to illustrate the difference between ATMOS and Harmonoise. The results are presented in the 1/3 octave band spectrum.

actual accuracy is better represented by the difference between the reference solution and the Harmonoise model, this is shown in figure 5.12. As seen before is the error the largest around the frequency of the local minimum, 1200 Hz. The overall error is well below 3 dB. Therefore, the results of the Harmonoise model for this case can be considered accurate. Note that the computational time of the Harmonoise model is drastically lower. The computation of both solutions was done on the same computer. The computation time of the Harmonoise solution was < 1 second, while the computation time of ATMOS was around 20 minutes. In case of larger propagation distances this difference is even larger.

Case C_2 looks at a strictly logarithmic profile. It is recalled that the Harmonoise model linearizes the logarithmic profile (see section 4.4.3). Figure 5.13 shows the result of case C_2 . Two reference results are included in the figure: ‘GFPE log’ is the actual parabolic equation solution for the chosen parameters and ‘GFPE lin’ is the parabolic equation solution for the sound profile as linearized by the Harmonoise model. The Harmonoise model is quite far off from the logarithmic reference solution. The actual values in dB over the whole frequency range look similar, indicating that the overall sound pressure level might still be accurate. However, it seems that the frequencies where the destructive and constructive interference occurs are shifted. The linear profile gives a correct result for the center frequencies, suggesting that the linearized profile is not able to correctly approximate the logarithmic profile in this case.

The final case considered is the lin-log case C_3 . Figure 5.14 shows the results for this case. By comparing the results with figure 5.13 it can be seen that the frequency shift is reduced. This makes sense because the logarithmic parameter B is reduced from 1 to 0.5 in this case. The minima of the GFPE solution at 1000 Hz seems low in comparison with the minima around 1200 Hz calculated by the Harmonoise model. However, since the results are in 1/3 octave bands, this can be explained by the fact that part of the low values is shifted into the next band by the calculation with the Harmonoise model.

It can be concluded that for cases where the source and receiver are low and the propagation distance is relatively short in the presence of a partly logarithmic sound speed profile, the linearized profile does not accurately capture the ground attenuation. However, the more linear the profile is in these circumstances, the better the accuracy.

5.1.4 Verification for high sources

In this part high sources (which could be, for example, wind turbines) and longer propagation distances are considered. To determine the accuracy for a higher source and longer propagation distance one has to keep in mind the limitations of the Harmonoise model (see section 4.5):

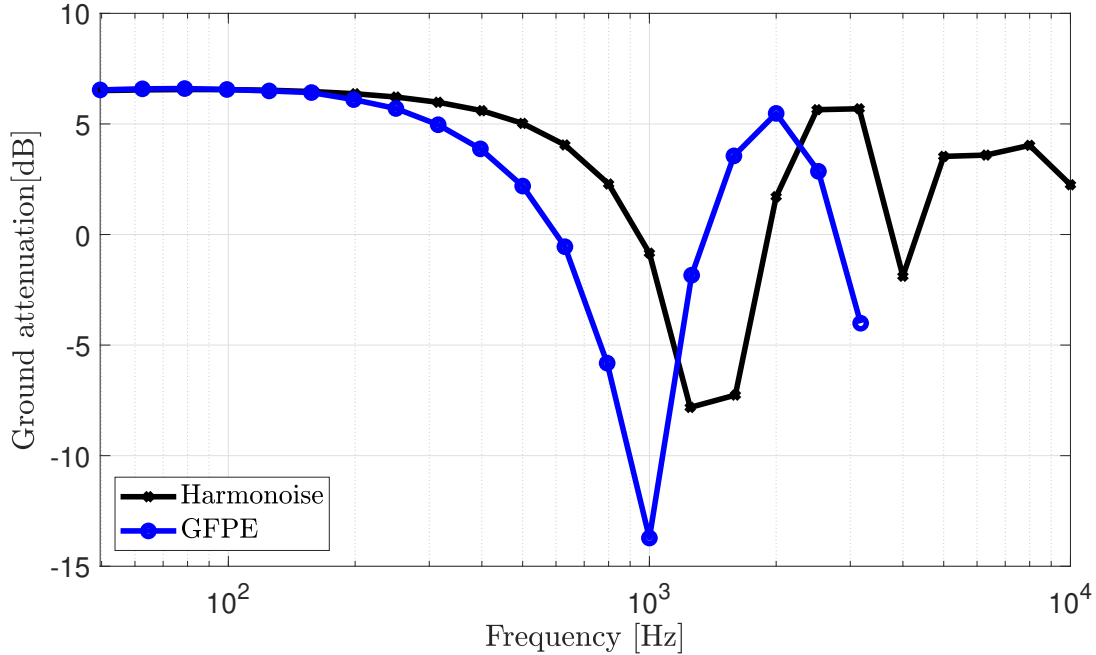


Figure 5.14: Ground attenuation of case C_3 calculated with ATMOS (a GFPE solver) and the Harmonoise model. This case illustrates the difference between ATMOS and Harmonoise. The results are presented in the 1/3 octave band spectrum.

Table 5.2: Limitations for the considered cases for verification of high sources

	A_{har} [1/s]	R [m]	d/R	Multiple reflections from [m]
Case D ₁	0.03	$1.1 \cdot 10^4$	0.10	3815
Case D ₂	0.0117	$2.9 \cdot 10^4$	0.04	5395
Case D ₃	0.03	$1.1 \cdot 10^4$	0.10	3125

- multiple reflections should not occur
- the distance between source and receiver divided by the radius of a ray path should not exceed 0.2, $d/R < 0.2$

Again three type of sound profiles are chosen: a linear profile, a logarithmic profile and a lin-log profile. The parameters of the considered cases are:

Case D₁: $A = 0.03$, $B = 0$, $h_s = 80$ m, $h_r = 1.5$ m, $d = 1200$ m with a flat acoustically hard ground profile

Case D₂: $A = 0$, $B = 1$, $h_s = 80$ m, $h_r = 1.5$ m, $d = 1200$ m with a flat acoustically hard ground profile

Case D₃: $A = 0.03$, $B = 0.2$, $h_s = 80$ m, $h_r = 1.5$ m, $d = 1200$ m with a flat acoustically hard ground profile

Table 5.2 shows the corresponding limitations of the Harmonoise model for these cases. In the table multiple reflections are calculated by tracing the ray paths as described in Appendix D and R as c_0/A_{har} (see section 4) where A_{har} is the gradient of the linearized profile. Thus, all the cases are well within the constraints of the model.

Figure 5.15 shows the ground attenuation for case D₁ calculated with the Harmonoise model and with the GFPE solver ATMOS. The results agree very well. The difference between the Harmonoise model and the GFPE solver, the error, is illustrated in Figure 5.16. The error is close to the error of the low source result. Thus, for this case the Harmonoise model is valid.

Next case D₂, with a strictly logarithmic profile, is considered. The results of the Harmonoise model are shown in figure 5.17 along with the reference results for the actual logarithmic case solved with the GFPE solver and the sound profile as linearized by Harmonoise. Initially one might expect the results to be slightly better as the results of case D₂ for the low source because the gradient of the logarithmic profile at higher altitudes is more constant (see for example figure 6.4) and since the source is higher

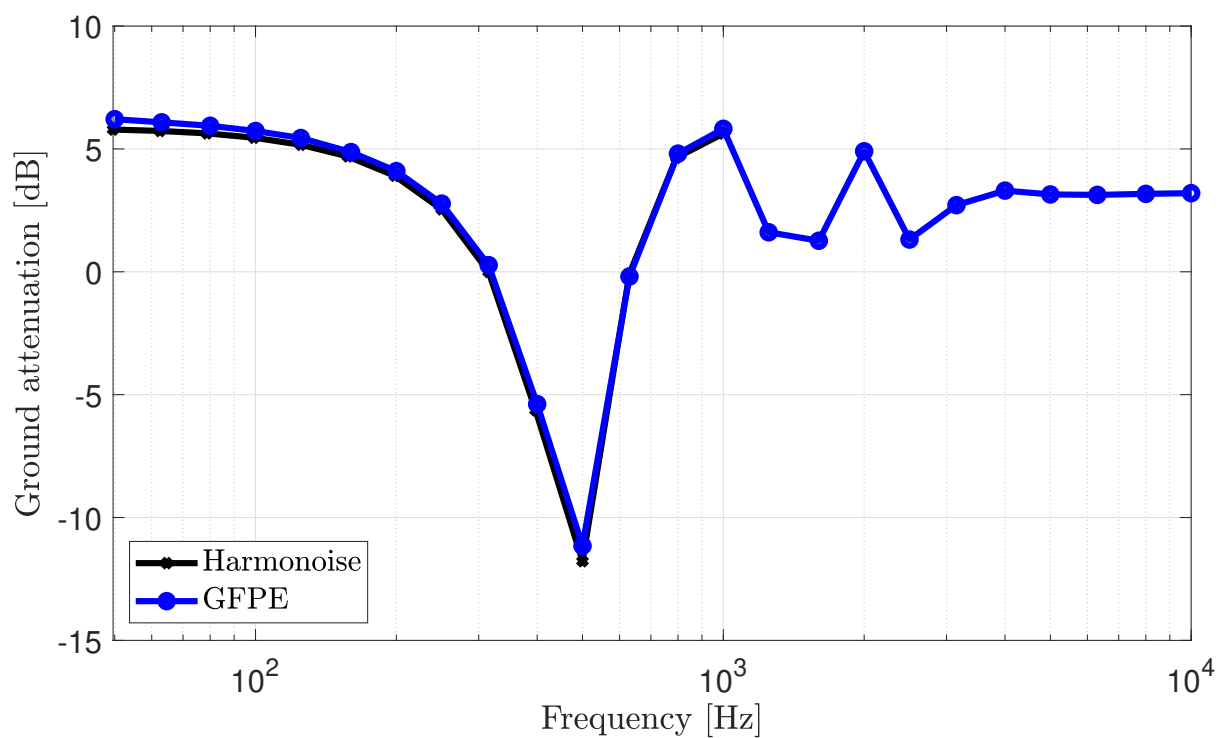


Figure 5.15: The ground attenuation of case D_1 for several 1/3 octave band frequencies computed by the Harmonoise model and ATMOS.

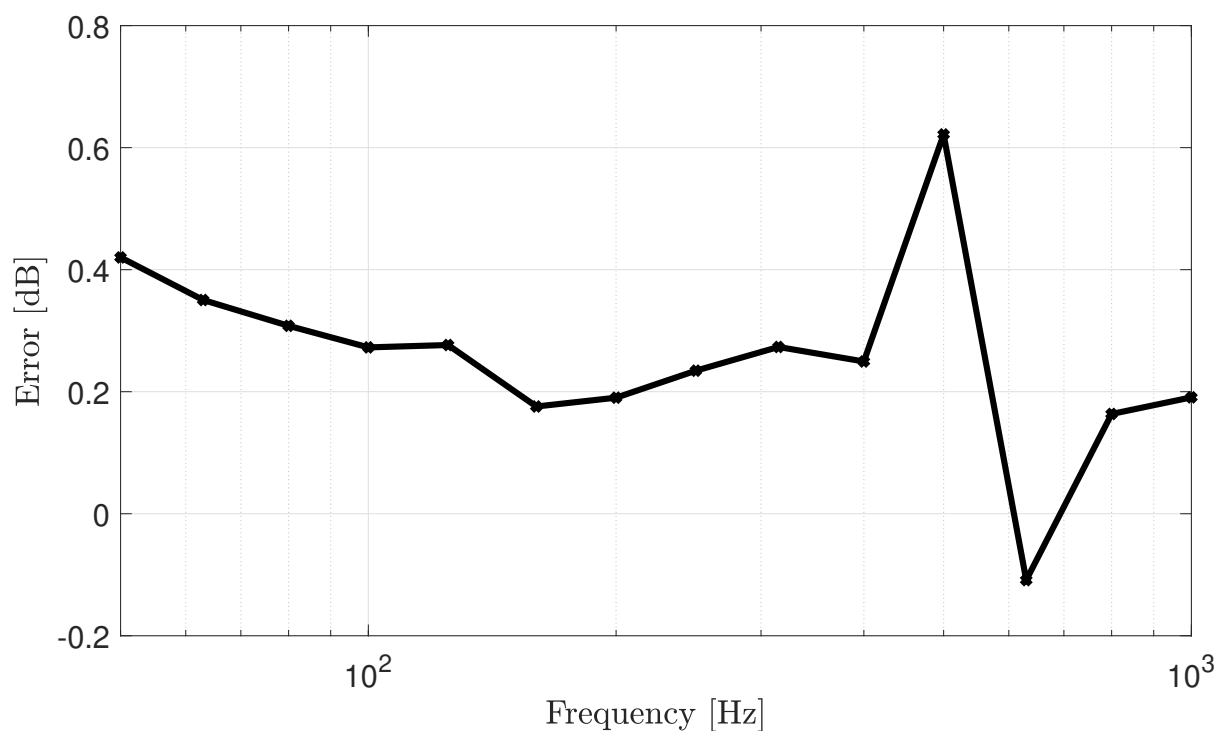


Figure 5.16: The difference between ATMOS and the Harmonoise model of case D_1 .

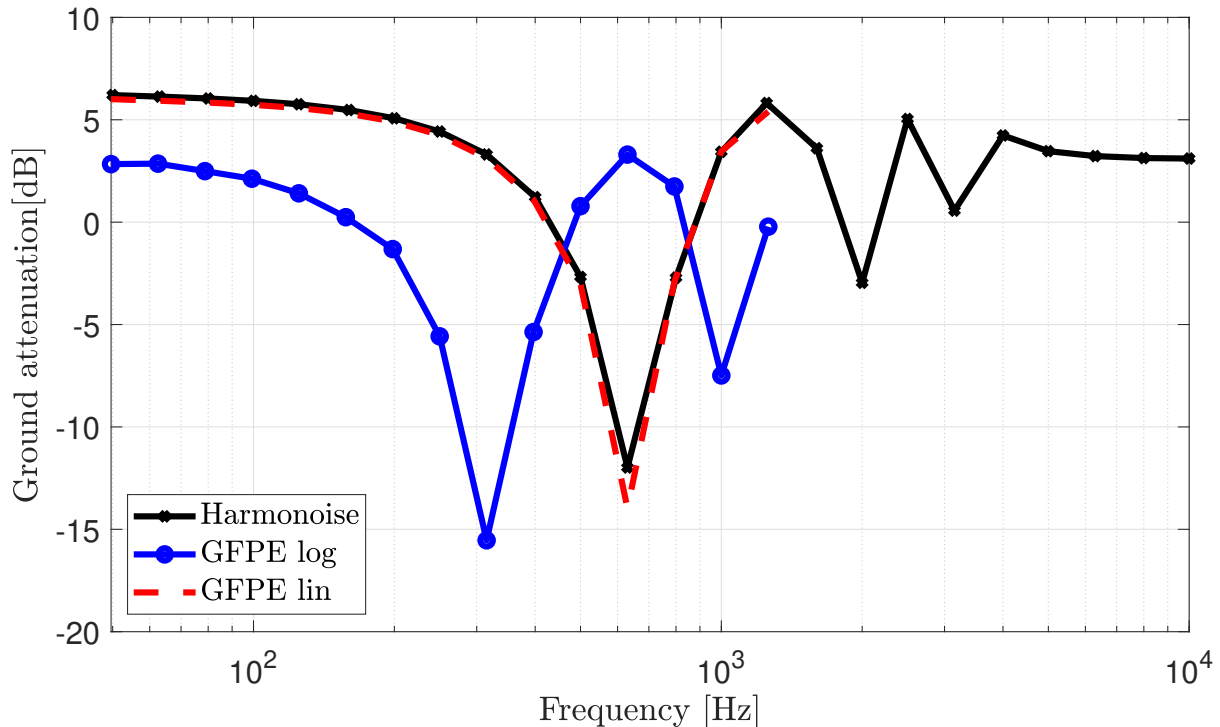


Figure 5.17: The ground attenuation of case D_2 for several 1/3 octave band frequencies computed by the Harmonoise model and ATMOS.

positioned, the rays travel more through this relatively constant region. However, the contrary is true; probably because of the larger distance, the error is amplified. Similarly to case D_2 of the low source, the frequency is shifted but in this case also the actual value of the ground attenuation is over predicted by the Harmonoise model.

Finally, case D_3 with a lin-log profile is simulated. Figure 5.18 shows the results. In comparison with case D_2 , the logarithmic part for this case is relatively small. Note that it is so small that the Harmonoise model linearizes the profile as if it were strictly linear (see table 5.2). Possibly because of the small logarithmic part, the results of the Harmonoise model in comparison with the reference solution agree better than they did for case D_2 . Still, a frequency shift of approximately 100 Hz occurs, indicating that the small logarithmic part does influence the result.

For high sources with long propagation distances, the linear case is still accurate. However, the sound speed gradients had to be scaled down to comply with the constraints of the Harmonoise model. In the case of logarithmic profiles, errors can be considerable and therefore only situations with sound profiles dominated by linear behavior will give reliable results.

5.2 The Harmonoise model for wind turbine noise

In the previous sections, several cases with the Harmonoise model were compared with reference results. It was found that the accuracy of the ground attenuation was strongly dependent on the case. The overall conclusion was that relatively linear sound speed profiles are captured correctly, but logarithmic sound speed profiles increase the error significantly. The other attenuation mechanisms considered, geometrical spreading and atmospheric absorption, are accurate in all cases. All the cases verified were in downwind directions, indicating a downward refracting atmosphere.

To estimate the capability of the Harmonoise model to predict the propagation of sound emitted by wind turbines, the following questions need to be considered:

- Are multiple reflections important for wind turbine sound?
- Is the range limitation of the Harmonoise model induced by the conformal mapping a problem?
- Can the lin-log profile describe a realistic atmosphere, and is the error of linearizing this profile

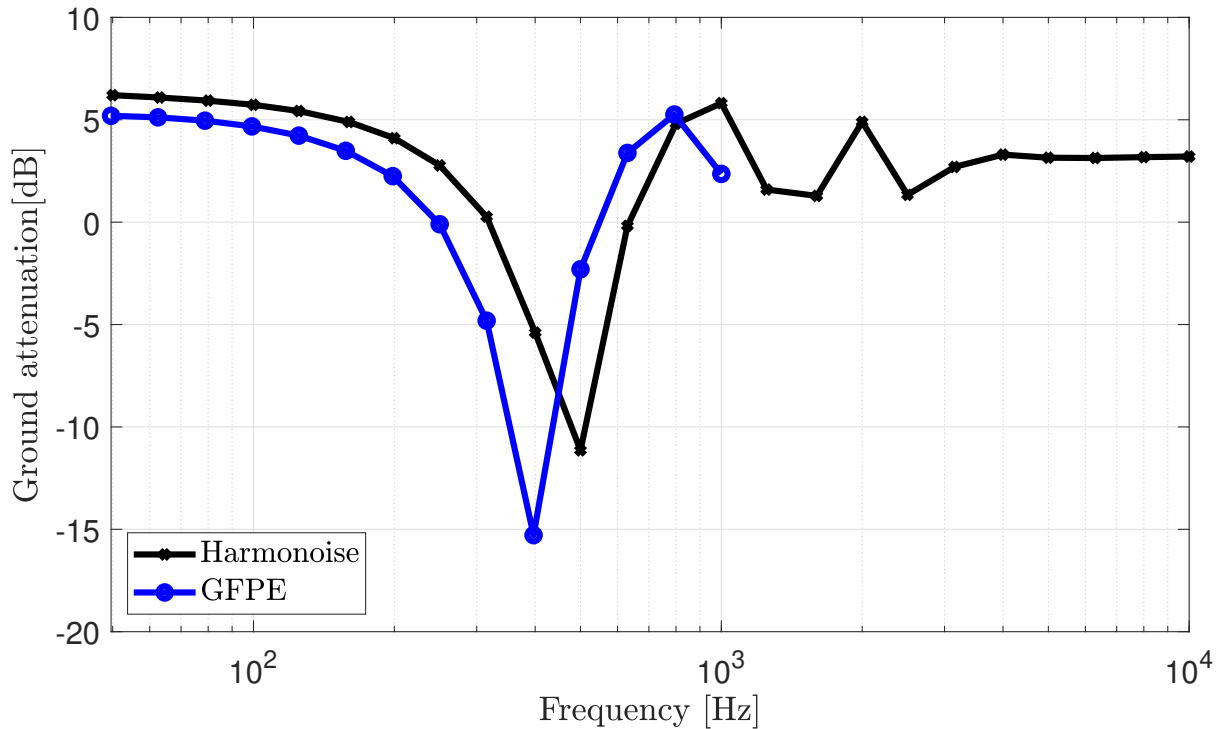


Figure 5.18: The ground attenuation of case D_3 for several 1/3 octave band frequencies computed by the Harmonoise model and ATMOS.

acceptable?

- What is the importance and prediction for upwind conditions?
- Can a wind turbine be modeled as a point source?

Multiple reflections can significantly increase sound pressure levels in certain situations. For example, Hansen et al.[1] has shown that in the case of multiple ground reflections, the reduction in dB per doubling of distance from the source can decrease to 3 dB, compared to the normal reduction of 6 dB due to geometrical spreading. The distance at which multiple reflections occur depends on the source height, receiver height, and sound speed gradients. A wind turbine, being a high source, will typically have the point of multiple reflections occurring at a relatively far distance from the turbine (the distance for several cases was presented in table 5.2). At this point, other attenuation effects have already significantly decreased the sound pressure level, making multiple reflections less relevant. Additionally, sound waves lose some of their energy upon reflection, further reducing the impact of multiple reflections. However, low frequency sounds, which are not greatly affected by atmospheric absorption and are better reflected than higher frequencies, can travel long distances under certain circumstances. These low frequency sounds do not always show up in a dBA spectrum but are produced by wind turbines. Therefore, one has to keep in mind that for predicting noise of very low frequencies, the range of the Harmonoise model might be less than desired.

The range limitation due to conformal mapping was defined as $d/R < 0.2$. This limitation depends on atmospheric gradients. In the following chapter, it will be shown that the gradients of cases D_1 and D_3 in table 5.2 are reasonable gradients for wind turbine propagation. This means that the maximum distance will be approximately 2200 m, and even beyond this distance, the results may still be accurate enough. At this point, the sound pressure levels for frequencies between 50-10000 Hz have already decreased significantly. Therefore, similar to the case of multiple reflections, the range may only become a limitation for very low frequencies.

The Harmonoise model takes as input a lin-log sound speed profile. If a real atmosphere can not be described by such a profile, errors will occur. In Appendix C a methodology to approximate a real atmosphere is presented. There, it is shown that a lin-log profile can describe such an atmosphere very well. On the contrary, the linearization that the Harmonoise model does with the lin-log profile results in quite a large error for sound speed profiles with a logarithmic behavior. Unfortunately, the speed of

sound in the atmosphere is best described by a logarithmic profile (see Appendix C). In the next chapter, the Harmonoise model will be used anyway to draw conclusions about the expected behavior of wind turbine sound. However, one has to keep in mind that the expected error of the ground attenuation is similar or even worse, as presented in figure 5.17 and 5.18.

In the verification cases, only a downwind propagation direction was considered. Generally, the upwind propagation cases are less relevant due to the fact that sound refracts upwards and that the perceived sound levels are the same or lower compared to downwind propagation. Nevertheless, limitations imposed by upwind propagations have to be accounted for. This is done in the next chapter.

Finally, the Harmonoise model as presented here is based on point-to-point propagation. So, the question that could be raised is whether a wind turbine can be modeled as a point source. In [37] it was determined that a wind turbine can be modeled as a point source if the following condition is met:

$$\sqrt{d^2 + h^2} > B_L \sqrt{5} \quad (5.1)$$

where d is the horizontal distance, h is the rotor height and B_L is the length of the wind turbine blade. This implies that even near the root, a wind turbine can be considered a point source. However, additional studies indicate that the point source approximation somewhat flattens interference dips. This effect is clearly visible at 500 m, but becomes less pronounced as one moves further away. Also, with the point source approximation, it is not possible to correctly predict the amplitude modulation [38, 39]. The latter is not an issue for this work because only the averaged sound levels over one wind turbine rotation will be considered.

Chapter 6

Wind turbine simulation

In this section, the Harmonoise model is used to perform simulations to estimate the sound pressure level around a single wind turbine. To perform the simulation, two things still need to be considered. The first is that the actual power and directivity of the source are unknown. To perform realistic simulations, realistic source data is necessary. The sound emitted by a wind turbine depends heavily on several factors, like the type of turbine and atmospheric conditions. The generation of reliable source data is done with a semi-analytic Amiet method, which is discussed in section 6.1.

Secondly, a realistic atmosphere needs to be considered. The atmosphere depends on several factors, such as topology, time of day, and weather conditions. A possible way to approximate the atmosphere is via similarity theory. This is discussed in Appendix C.

Figure 6.1 shows the calculation procedure for the sound pressure levels around a single wind turbine. The input parameters are dependent on the case that is simulated. Section 6.2 presents the general case that will be simulated. In section 6.3 the results of the source simulation are presented. Finally, in section 6.4 the sound pressure levels around a wind turbine are calculated with the Harmonoise model and the source model.

6.1 Source simulation

Amiet's theory for leading- and trailing-edge broadband noise has been used to model the noise from wind turbines [40, 41]. Amiet's theory for trailing-edge noise is an analytical method that relates the fluctuations in wall pressure close to the trailing edge of a flat plate to the power spectral density (PSD) of the sound pressure radiated in the far-field. In a similar way, the leading-edge noise theory links the power spectral density (PSD) of the up-wash velocity fluctuations of the flow near the leading edge to the PSD of the pressure in the far field. Most of the time, Amiet's theory has been used to predict the noise radiated from fixed airfoils in a uniform flow. However, it can also be used to simulate the noise emitted by rotating machines by dividing the blades into segments to account for different relative speeds and flow conditions at different radial positions. This method is called "strip theory," [42] and it has been used for fans [43, 44, 45, 46, 47], helicopters [42, 48], and wind turbines [49, 50, 51, 52, 53].

As was said above, the trailing-edge noise theory is based on the wall pressure fluctuation spectrum. In this work, semi-empirical models from Goody [54] and Rozenberg [55] are used for positive and negative pressure gradients, respectively. XFOIL is used to calculate the parameters of the boundary layer [56].

The von Kármán spectrum is used to model the inflow velocity spectrum for the leading-edge noise theory. Monin-Obukhov similarity theory is used to figure out the integral length scale and the amount of turbulence (see Appendix C.2 for more information about Monin-Obukhov theory).

The used code is developed by [57] where more details are available.

In the far field of the wind turbine, the sound pressure levels in 1/3 octave bands are calculated on a sphere with an arbitrarily large radius. The spectrum is then scaled on a sphere with a radius of 1 m, centered at the hub. Christophe et al. [58] have recently used the same method.

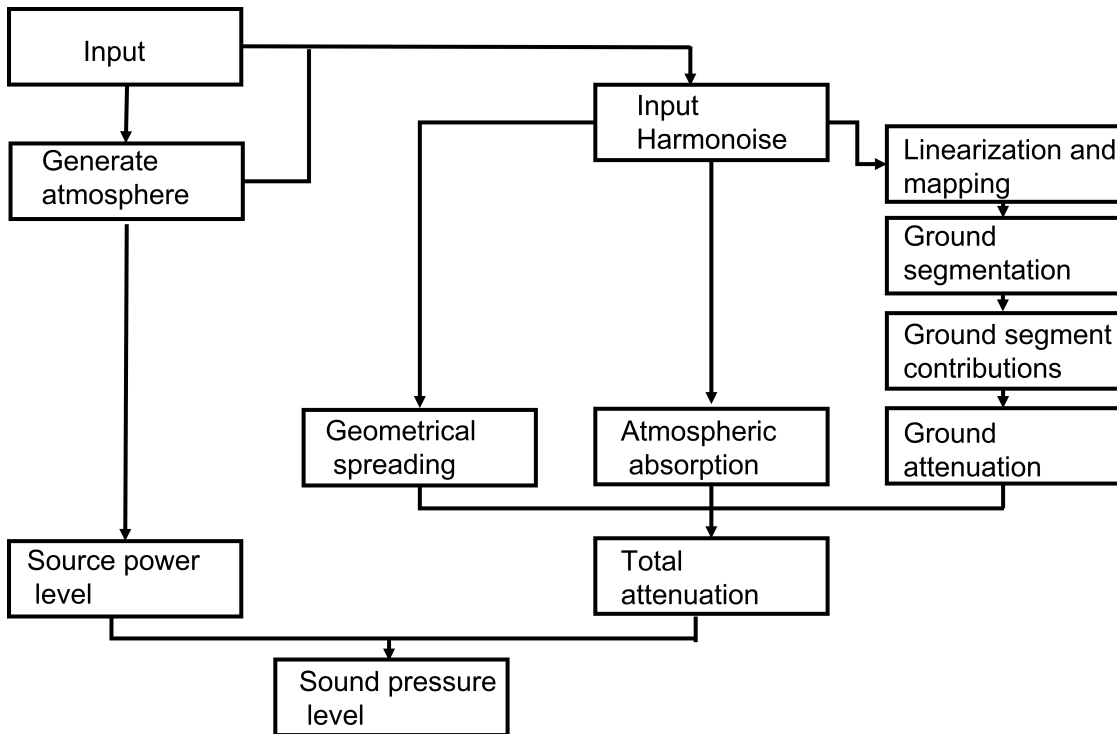


Figure 6.1: Calculation procedure of calculating the sound pressure level around a wind turbine with a source model and the Harmonoise model.

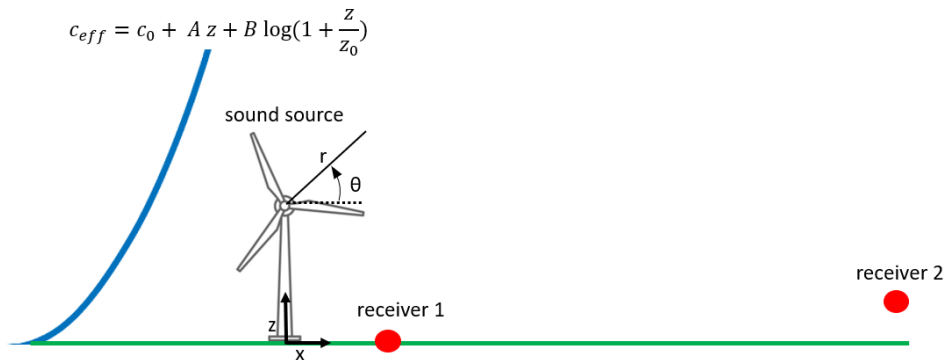


Figure 6.2: Representation of the general 2D case that is used to simulate wind turbine noise of a single turbine.

6.2 Test case

The case of a wind turbine present in an area with a flat, acoustically hard surface will be simulated for 2D and 3D cases. The main focus of the simulations is on how the meteorological conditions affect the sound pressure level and to get a general idea of possible sound levels around wind turbines.

The general 2D case is visually represented by figure 6.2. The figure shows a wind turbine as a sound source with two receivers downwind. The results of receiver 1 will be compared to on-site measurements of a real wind turbine. Receiver 2 will be used to give detailed information about the sound pressure levels in the 1/3 octave band spectrum and how much each propagation effect is responsible for them. In the figure, two coordinate systems are present. Sources and receivers will always be described in cartesian coordinates, but post-processing of source data is more convenient in polar coordinates. Therefore, a polar coordinate system (spherical for 3D) is placed with as center the location of the point source (in cartesian coordinates $(0, h_{hub})$).

The 3D case is the same situation as the 2D case, but now the xy -plane around the turbine is considered. Figure 6.3 shows the 3D case. The receivers and conditions that are simulated will be presented in section 6.4.2.

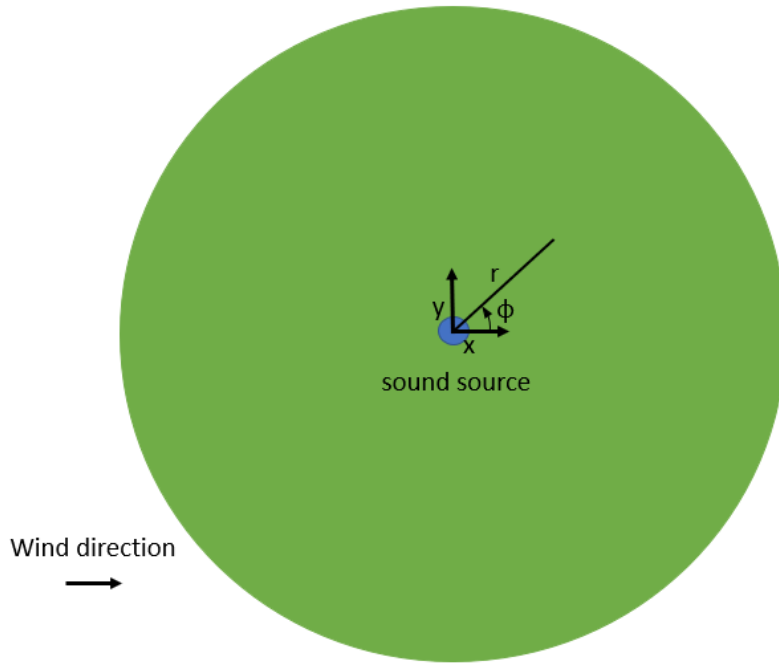


Figure 6.3: Representation of the 3D case, where the sound levels will be calculated somewhere in the xy -plane for a given receiver height.

Table 6.1: Parameters used in the source model to generate source data.

Parameter	Description	Value
Atm	Atmospheric stability	stable/neutral/unstable
h_{hub}	Hub height	80 m
z_0	Roughness length	0.1 m
T_s	Surface temperature	20 °C
H	Surface heat flux	-25/0/200 W/m ²
U_0	wind speed at hub height	8 m/s

6.3 Source simulation results

Using the source model, the sound pressure levels on a sphere with a radius of 1 meter are calculated. As a source, the SWT 2.3-93 turbine is considered (2.3 MW and 93 m rotor diameter). The three blades of the turbine are divided into 8 segments with a constant aspect ratio of 3. Each segment uses the NACA 63-418 airfoil, and the chord varies linearly from 3.5 m at the root to 0.8 m at the tip of the turbine blade. The angle of attack in the XFOIL simulations is 4 degrees. Table 6.1 shows the operating conditions of the turbine. For the generation of source data, three different atmospheric conditions are used: stable, neutral, and unstable. These atmospheres' corresponding heat fluxes are -25,0 and 200 W/m², respectively. Figure 6.4 shows the corresponding temperature profiles, wind velocity profiles, and effective sound speed profiles for downwind propagation. The corresponding parameters for the Harmonoise model are shown in table 6.2, these values result in the effective sound speed profile for downwind propagation by using the equation shown in figure 6.2. Note that the effective sound speed is dependent on the propagation direction, which is accounted for within the Harmonoise code. The source model with the three different atmospheres resulted in three sets of source data. Below, the results of a stable atmosphere are presented and discussed. The stable atmosphere is chosen because, in such an atmosphere, the sound speed gradients are the largest. The results of the stable atmosphere will be compared to the other atmospheres afterward.

The results are generated by using a grid in spherical coordinates, where θ equals the elevation angle, ϕ represents the azimuth angle, and r is the radial distance to the source. The source model averages over 1 blade rotation. So, the results are axisymmetric, which means that the pattern of radiation in the

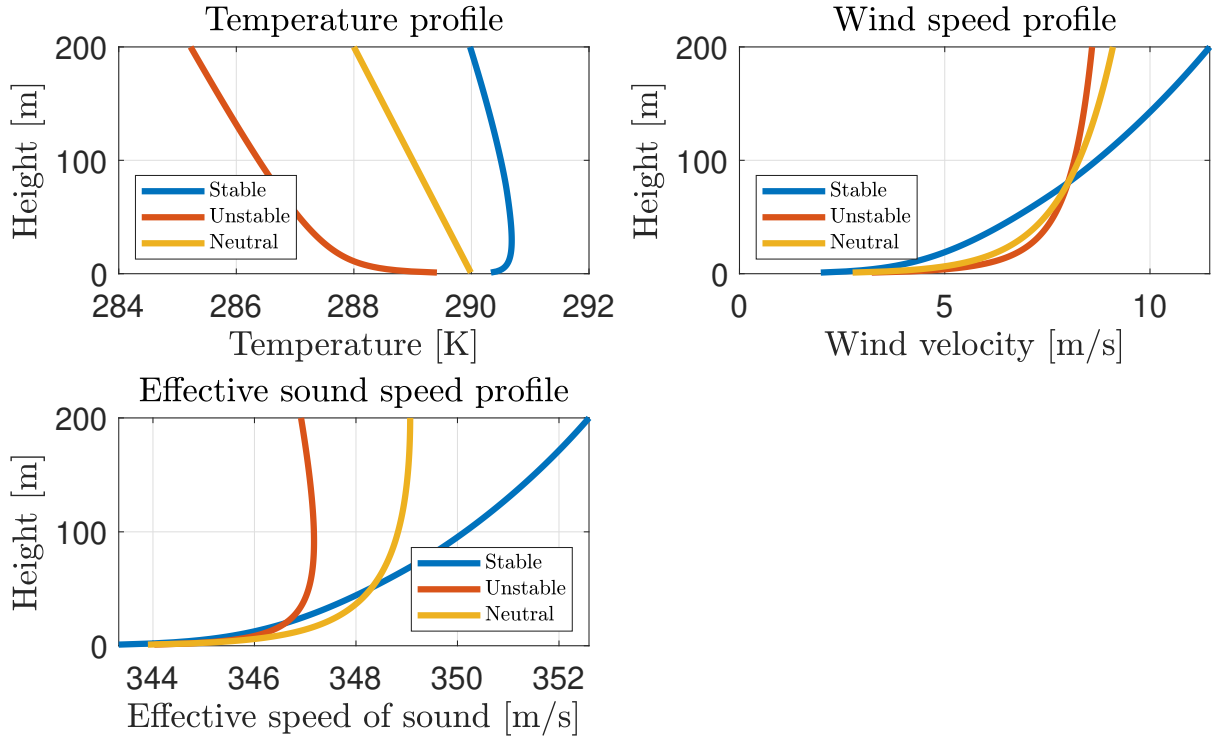


Figure 6.4: Temperature, velocity and effective sound speed profiles for a stable, unstable and neutral atmosphere. Generated with $U = 8$ m/s at 80 m, $z_0 = 0.1$ m, $T_s = 290$ K and Obukhovs lengths of 145,-86 and infinity respectively (see appendix C.2 for the definition of the Obukov length).

Table 6.2: The Harmonoise model's input values for lin-log sound speed profiles in a stable, unstable, and neutral atmosphere.

	A [1/s]	B [m/s]	c_0 [m/s]
stable	0.0191	1.1260	340.37
unstable	-0.0090	0.8355	342.32
neutral	-0.0059	1.1971	341.15

horizontal direction is the same as the pattern of radiation in the vertical direction. The 2D radiation pattern visualized by a polar plot is shown in figure 6.5. In this figure, the plane of rotation of the wind turbine is perpendicular to the wind direction. Note that, in the plane of rotation, a relatively low sound intensity is emitted.

The 3D results are represented by a sphere. To show the dependency of frequency, the sphere representing a low frequency, $f_c = 63$ Hz, is shown in figure 6.6 and a sphere representing a mid-frequency, $f_c = 1$ kHz, is shown in figure 6.7. The figures show that the sound power level is approximately 15 dBA higher at 1 kHz in comparison with the sound power level at 63 Hz. It is important to note here that the scale is in dBA and not in dB. A-weighting at 63 Hz is about -30 dB (see figure 2.2), thus the actual sound pressure of the low frequencies is quite high in comparison with 1 kHz. Figure 6.8 represents the overall sound pressure level.

For all frequencies, a blue circle of low sound power levels is present on the sphere. This region is parallel with the plane of rotation and is common for wind turbine sound [59]. The highest sound levels are found at the poles, which are located perpendicular to the plane of rotation. However, the sound levels for a large region around the poles are all relatively close.

Source data for the different atmospheric conditions is compared at a receiver 1200 m downwind with a height of 1.5 m. The data on the sound sphere as presented in figures 6.6, 6.7 and 6.8 depends on the location of the sphere. Therefore, the appropriate value of the source data needs to be used for the considered point. The data point that is chosen for this is the one that corresponds with the direct ray between the source and the receiver. The angle of the emitted ray by the source that directly reaches

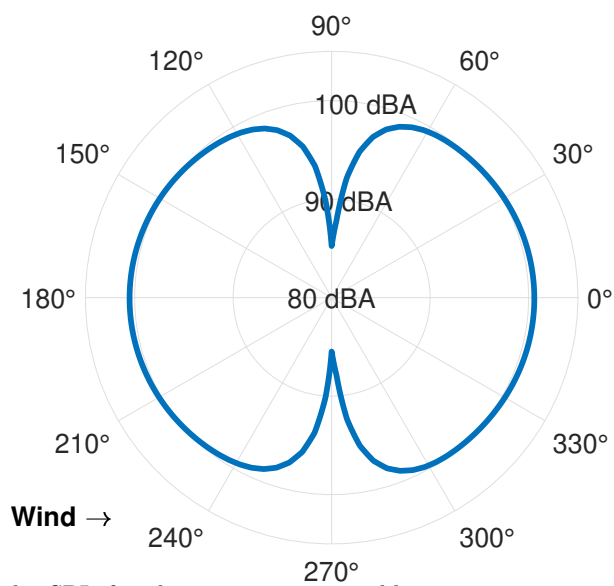


Figure 6.5: Polar plot of the SPL for the parameters in table 6.2, representing the horizontal and vertical directivity.

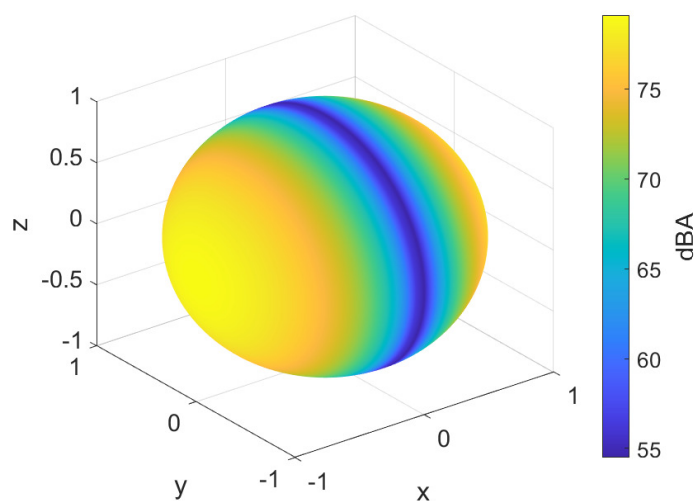


Figure 6.6: Directional source of 63 Hz represented by a sphere with a radius of 1 meter.

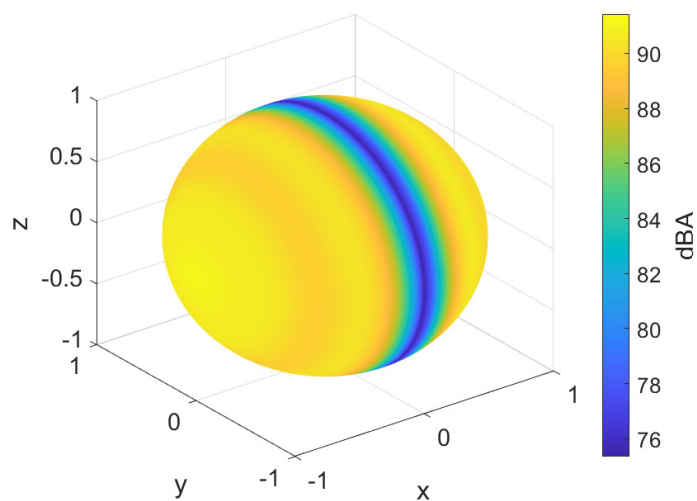


Figure 6.7: Directional source of 1 kHz represented by a sphere with a radius of 1 meter.

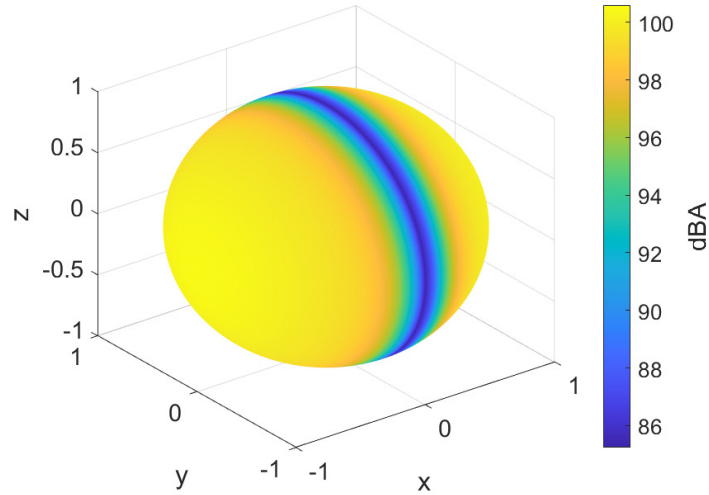


Figure 6.8: Directional source of the overall sound pressure level represented by a sphere with a radius of 1 meter.

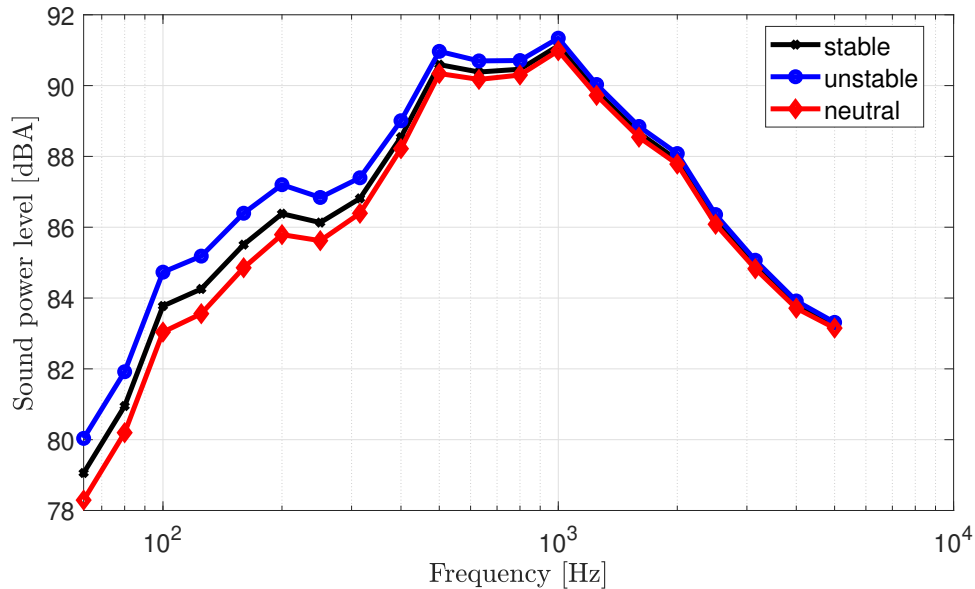


Figure 6.9: Sound power level of points source used to calculated values at 1200 m downwind from the SWT 2.3-93 wind turbine for different atmospheric conditions. The location on the 1 meter radius sphere is described by $\theta = -0.0077$ and $\phi = 0$

the receiver can be found by geometry as

$$\theta_s = -\theta_{SR} + \sin^{-1} \left(\frac{d}{2R \cos(\theta_{SR})} \right) \quad (6.1)$$

where θ_{SR} is the angle between the source and receiver defined as $\theta_{SR} = \tan^{-1}((h_s - h_r)/d)$. The propagation direction is downwind, indicating that $\phi = 0$. Thus, the value used of the sound sphere is the value at the location (θ, ϕ) which is for this case $(-0.0077, 0)$. Figure 6.9 shows that the largest deviations in sound power level are present in the lower frequency range. These deviations are 1-2 dB. At higher frequencies, the differences are small. Therefore, the results presented above for a stable atmosphere are a good representation of the other atmospheric conditions.

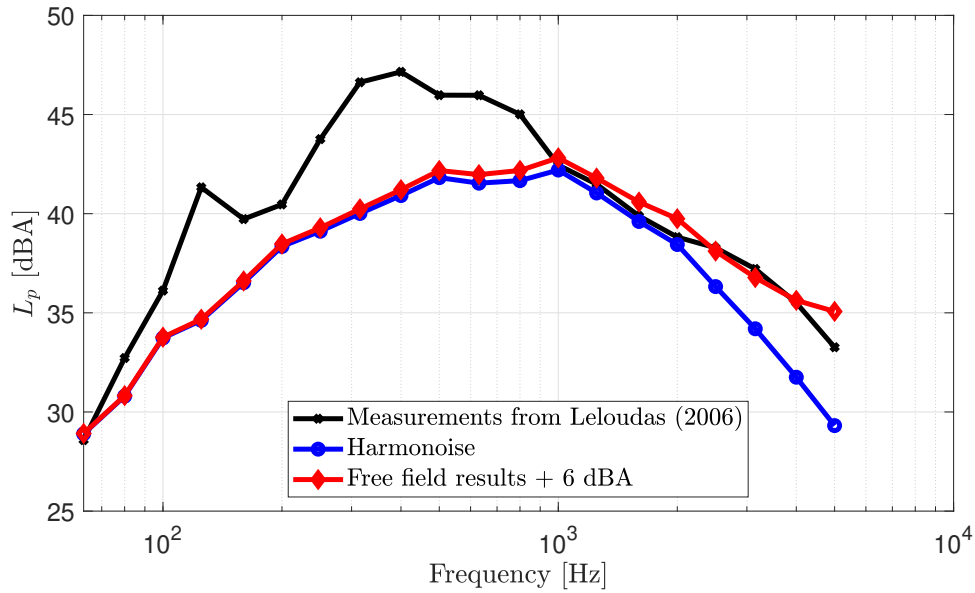


Figure 6.10: Comparison of the Harmonoise model with the source model, free field results of the source model + 6 dBA and on-site measurements for the SWT 2.3-93 wind turbine are presented.

6.4 Results

6.4.1 2D case

The 2D case, as shown in figure 6.2, represents two receivers. Receiver 1, located 100 meters downwind of the turbine, will be used to give an estimation of the accuracy of the source results. The sound pressure level at receiver 1 is computed for a neutral atmosphere. Figure 6.10 shows the results compared to on-site measurements of the SWT 2.3-93 turbine and free field results +6 dBA. The reason for the addition of 6 dBA is because the measurements are done with a hard measurement board, meaning that the receiver is placed at ground level to ensure that the direct and the reflected ray are in phase with each other; hence, 6 dBA is expected above the free field sound pressure level. Since the propagation distance is very short, refraction does not play a noticeable role. The results are in fact close to the free field results for low frequencies. At higher frequencies, where atmospheric absorption becomes relevant, the two results differ. The overall agreement with the experimental results is reasonable, the source model captures the general trend of the emitted sound levels, although deviations up to 6 dBA occur. Deviations like this are expected since there are often a lot of uncertainties in the simulation parameters (on top of the numerical errors) [1].

Receiver 2, located 1200 meters downwind of the turbine with a height of 1.5 meters, is used to give a detailed analysis of the 1/3 octave band spectrum at that point. Figure 6.11 shows the sound pressure level at receiver 2 and also includes results of the Harmonoise model and the source model to illustrate the influence of different effects. The figure demonstrates that the main influences on the sound pressure level are the source term and the spherical divergence. At higher frequencies, the atmospheric absorption becomes considerable. For certain frequencies, the sound pressure level increases due to the ground effect, and at other frequencies, because of destructive interference, the sound pressure level decreases. This is the same effect as observed in section 4. The actual sound pressure levels at receiver 2 are below 20 dBA for almost all frequencies, which is less than background noise.

6.4.2 3D Case

Next, the case of figure 6.3 is considered. The general approach is to make a grid of receivers and use the source data for each receiver with the Harmonoise model to obtain the sound pressure levels. Afterward, the results are interpolated to obtain a smooth sound map around the turbine.

The simulation grid must be defined by first determining its boundaries. The horizontal component of wind velocity can be calculated using $u \cos(\phi)$, where ϕ is the azimuth angle. The simulations are performed in a stable atmosphere, and the fitted lin-log profile in this type of atmosphere consists of a linear part ($A = 0.0191$ 1/s), a logarithmic part ($B = 1.1260$ m/s), and a constant ($c_0 = 340.37$ m/s).

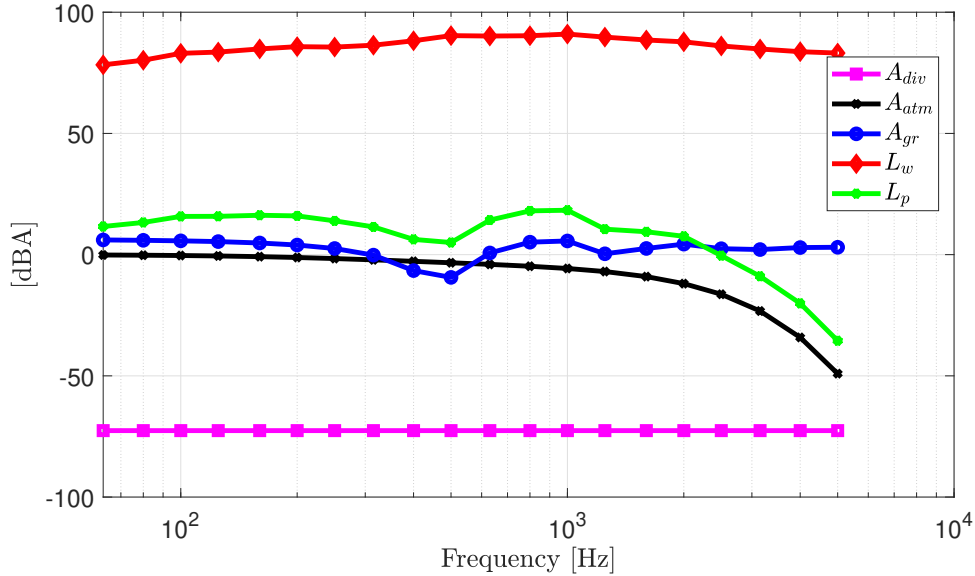


Figure 6.11: Sound pressure level of receiver 2. All the attenuation effects and the source power level are shown as well. The actual sound pressure level is calculated with $L_p = L_w + A_{div} + A_{gr} + A_{atm}$.

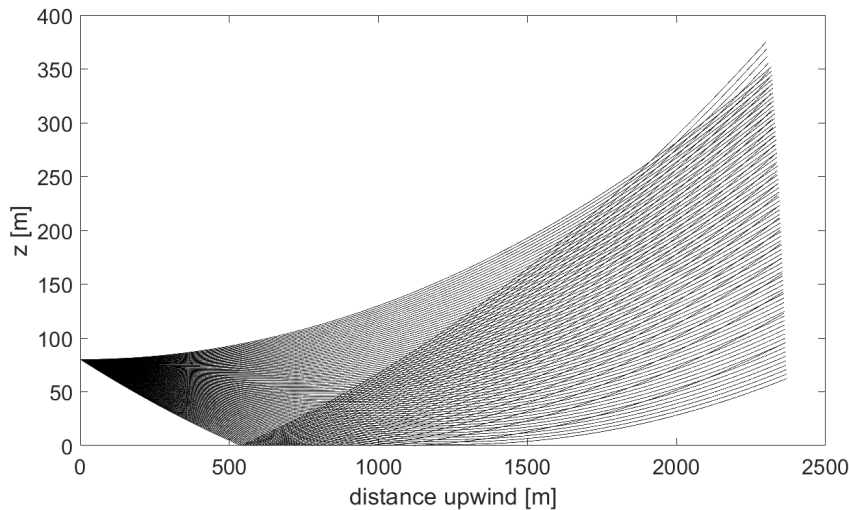


Figure 6.12: Ray tracing for a linear sound speed profile with a gradient of -0.0337 ; 100 rays leave the source at angles ranging from $-\pi/9$ to 0 radians. The start of the shadow zone can be identified around 1500 meter.

This corresponds to a linearized (A_{har}) gradient of 0.0337 $1/s$ according to the Harmonoise model. The value of A_{har} varies between -0.0337 and 0.0337 $1/s$ when the azimuth angle is taken into account. The maximum distance that can be considered due to conformal mapping ($d/R < 0.2$) at an azimuth angle of 0 or π is 2000 meters. Multiple reflections downwind of the turbine may also occur at a later distance (see table 5.2). However, at some point upwind of the turbine, the shadow zone is present. Since the Matlab version of the Harmonoise model does not include the effect of diffraction, the results near and within the shadow zone may not be simulated accurately. To estimate the location of the shadow zone, the method of ray tracing described in Appendix D.1 can be used (refer to figure 6.12). The figure shows that the shadow zone starts at around 1500 meters for a low receiver. Therefore, the simulation distance upwind should be less than 1500 meters at an azimuth angle of 0 or π .

The simulation grid is in polar coordinates, with ϕ spaced 61 times from $-\pi$ to π . The radial distance from the point source, r , is spaced in 100-meter increments from 100 to 2200 meters. Post-processing is done in cartesian coordinates and with the limitation of 1500 m in mind, a rectangular snapshot is taken from the computational grid. The resulting grid for the 3D simulation is shown in figure 6.13, where the red square is the area, in cartesian coordinates, used for post-processing. All the black dots on the grid correspond to receivers, and the blue dot in the middle represents the point source.

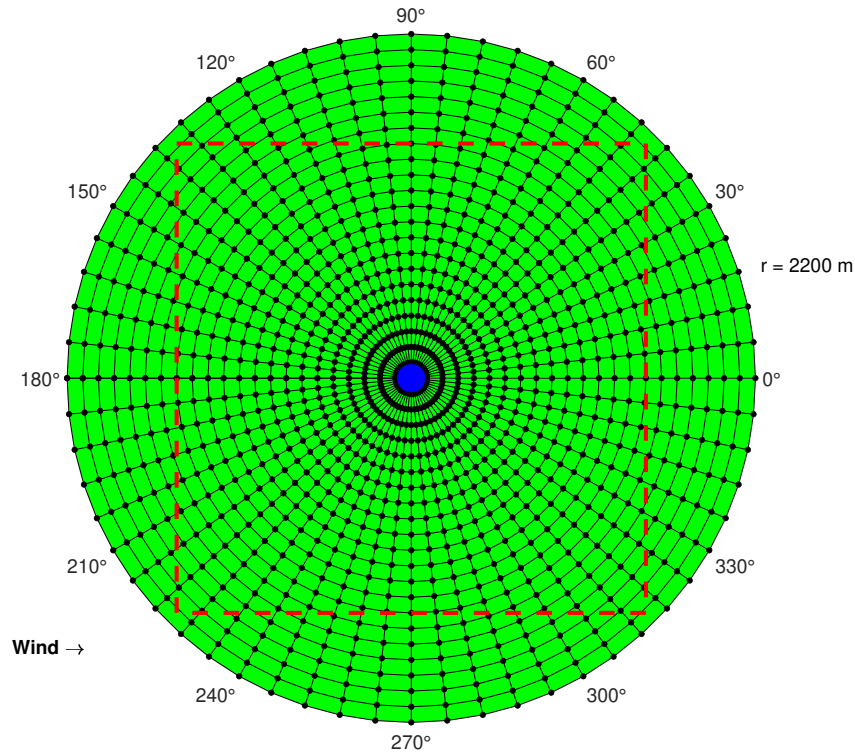


Figure 6.13: Simulation grid for the sound pressure level around a wind turbine. All black dots can be considered receivers with a height of 1.5 meter above the ground plane. The red square indicates the area that is used for post-processing of the results.

The grid is used in the case of a stable atmosphere with the source data for the SWT-93 wind turbine. The temperature, wind, and effective sound speed profiles for a stable atmosphere are shown in figure 6.4.

Figure 6.14 shows the results for a low center frequency of 63 Hz. In this case, the results for upwind and downwind conditions are fairly symmetric. The frequency is low. Therefore, the difference between the direct and reflected rays' paths is small compared to the wavelength. Thus, the rays are almost in phase for every distance. Because of this, no interference patterns can be seen. The actual sound pressure level at 63 Hz is quite low as well, around 20 dBA near the root of the wind turbine.

The results of a larger center frequency, 1000 Hz, are shown in figure 6.15. In this figure, the interference patterns are clearly visible. The overall dBA is considerably larger than the 63 Hz case as well. Note that the green area around $x = -1500$ m is the edge of the shadow zone. Therefore, the results over there can not be considered accurate.

The overall sound pressure level is shown in figure 6.16. Again, the results are symmetric, meaning that the overall sound pressure levels upwind and downwind are approximately similar. However, as seen in figure 6.15 the 1/3 octave band spectrum at every location will be unique. The fact that the overall sound pressure levels are similar can be explained by the fact that at every location in the region, two rays arrive. Thus, if all the frequencies are summed up logarithmically, the overall sound pressure level is equal for the same radial distance from the source. Since the 1/3 octave band results vary, the perceived sound can be slightly different for different locations at the same radial distance from the source. The actual values of the overall sound pressure levels are mainly considerable nearby the wind turbine. Most sounds below 30 dBA ($r > 500m$) will be overruled by background noise or other noise sources.

In the next part, different types of atmospheres will be considered for various azimuth angles. Again, the profiles for stable, neutral, and unstable atmospheres are shown in figure 6.4.

Figure 6.17 displays the sound pressure level at 1000 Hz for five different azimuth angles ($0, \pi/4, \pi/2, 3\pi/4$ and π). At small distances, where the rays are almost perfectly in phase, the difference is small. However, deviations begin to appear at a distance of approximately 400 meters. Only the azimuth angle of $\frac{1}{2}\pi$ shows minimal deviations. This is because, in this case, the term $u \cos(\phi)$ is zero, meaning that the horizontal component of the wind velocity is zero. The minor differences are caused by the temperature

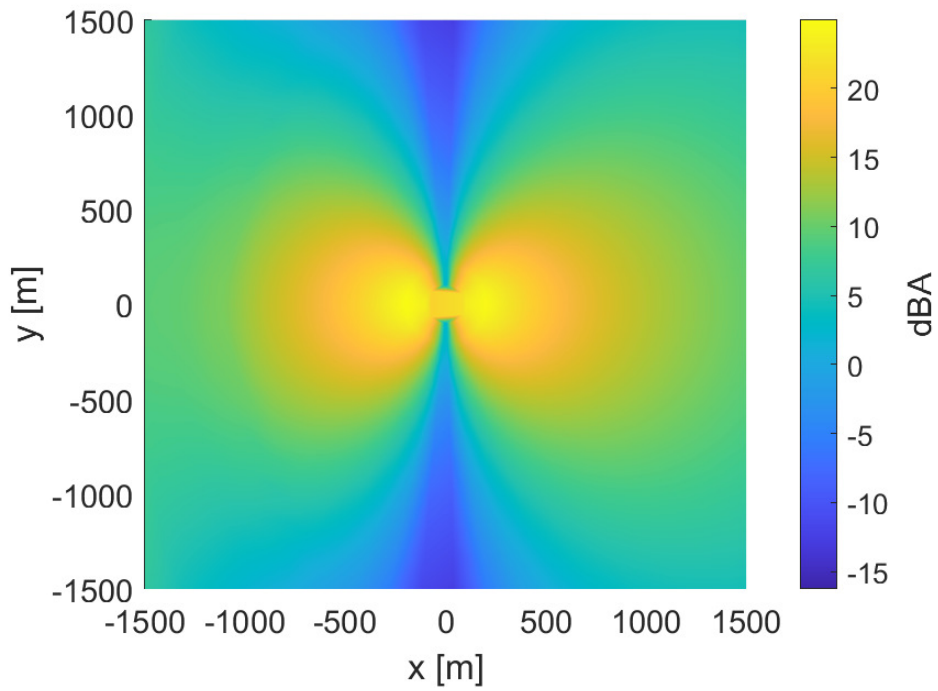


Figure 6.14: Sound pressure level around a wind turbine for the center frequency of 63 Hz in case of a stable atmosphere.

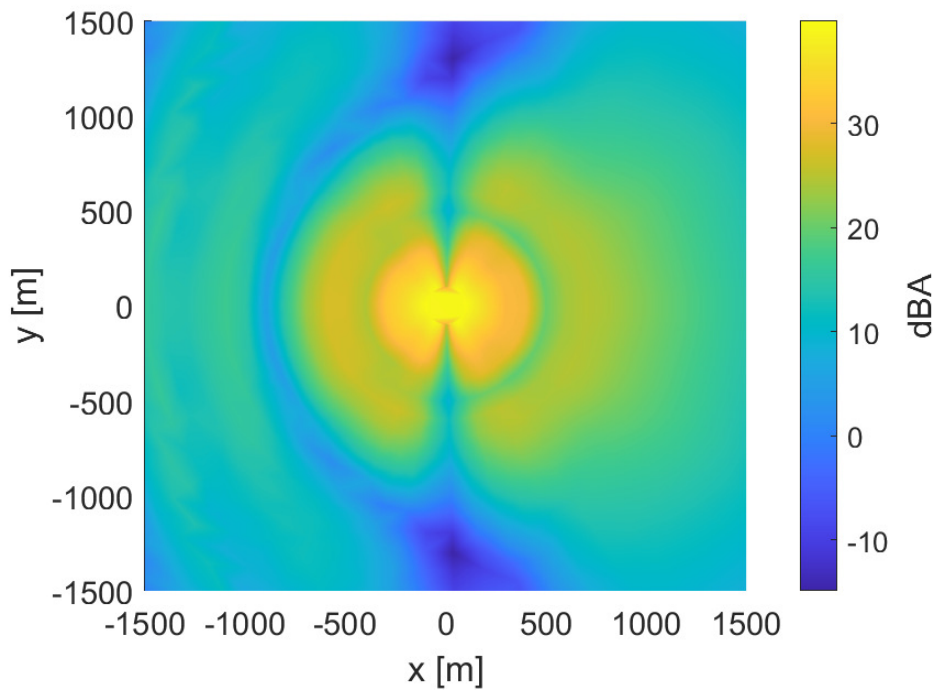


Figure 6.15: Sound pressure level around a wind turbine for the center frequency of 1000 Hz in case of a stable atmosphere.

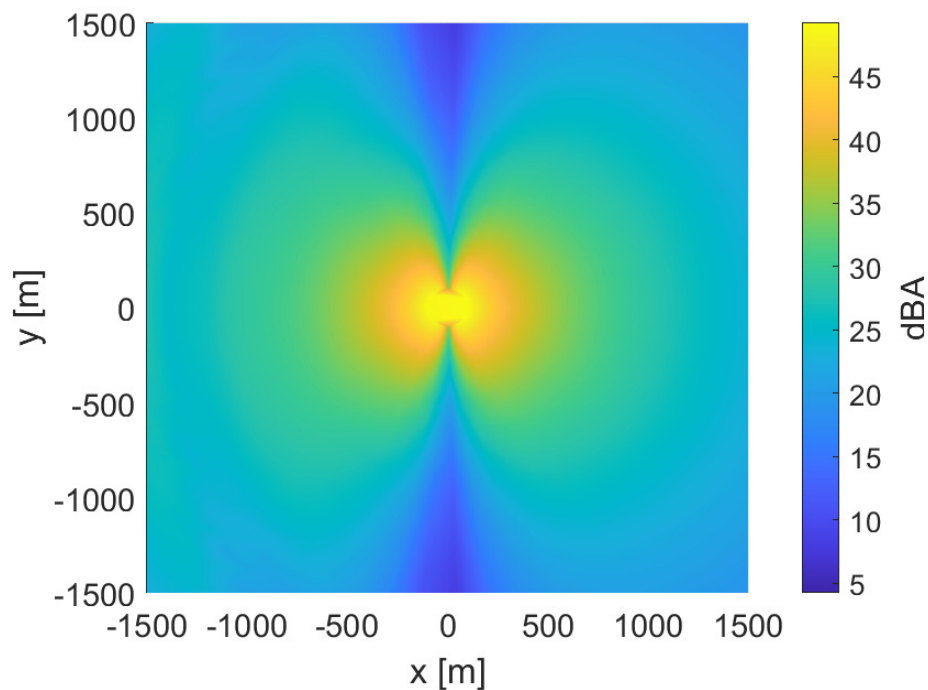


Figure 6.16: Overall sound pressure level around a wind turbine in case of a stable atmosphere.

profile and differences in the source data.

Figure 6.18 displays the overall sound pressure level for five different azimuth angles for a stable, a unstable and a neutral atmosphere. The results for the different atmospheres nearly completely overlap. From this, it can be concluded that the atmospheric conditions do not have a significant influence on the overall sound pressure level around a wind turbine for distances up to approximately 1500 meters.

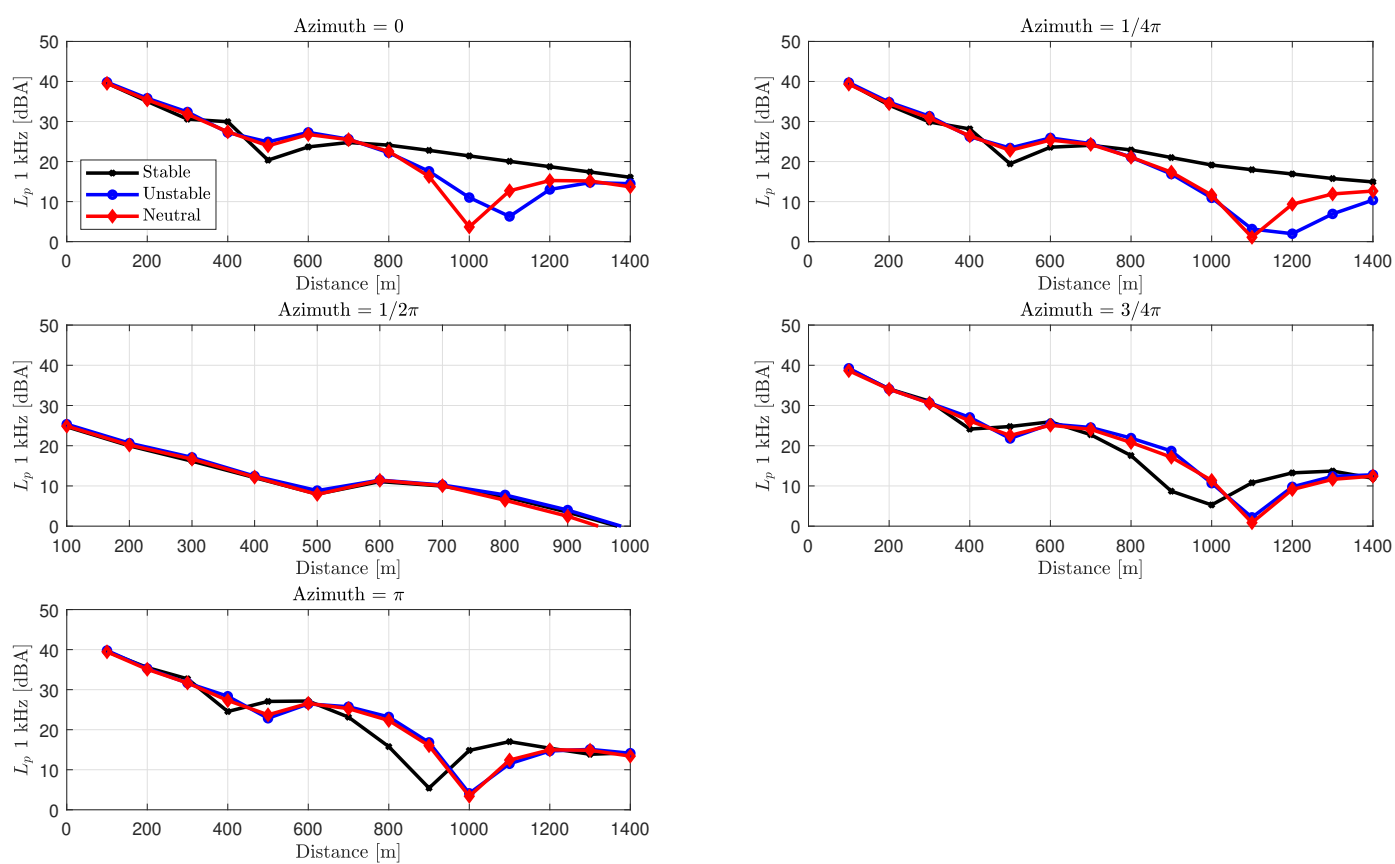


Figure 6.17: Sound pressure level against distance for different azimuth angles for the center frequency of 1000 Hz.

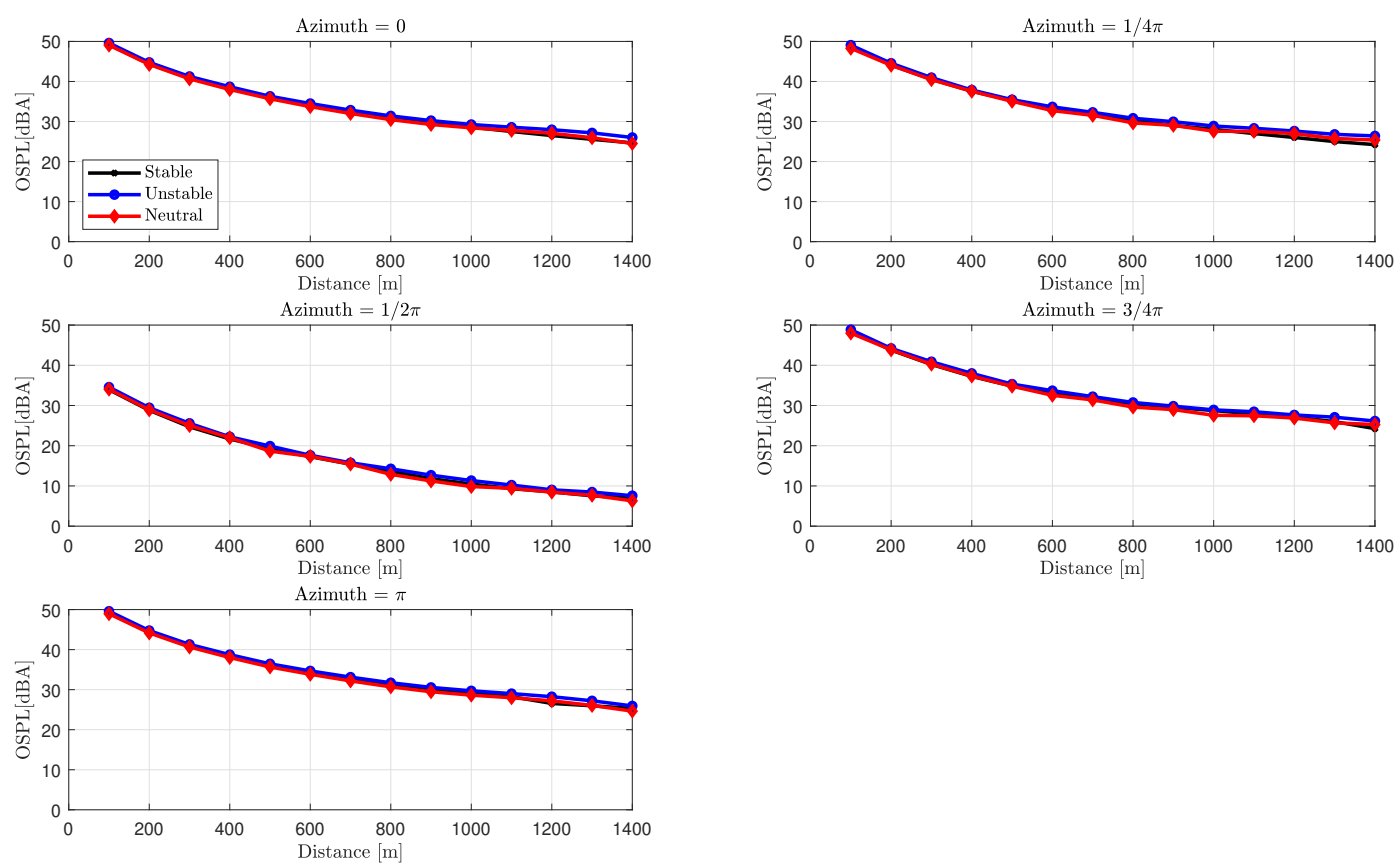


Figure 6.18: The overall sound pressure level plotted against radial distance from the wind turbine for different azimuth angles.

Chapter 7

Analyzing horizontal gradients with the Harmonoise model

The Harmonoise model is only applicable in a layered atmosphere, where the speed of sound is described as a lin-log function with respect to height (see section 4). This lin-log function is linearized to describe ray paths as circular arcs. The radius of the ray paths is used to perform a conformal mapping, which maps the circular ray paths to straight ray paths and curves the ground with them. However, in some cases, the speed of sound might also be dependent on propagation direction; thus, in those cases, the speed of sound is a function of height and distance instead of height only. The current Harmonoise model is not able to include horizontal speed gradients, and one can only make use of ray tracing methods or PE methods.

This chapter proposes a method that can enable the Harmonoise model to incorporate horizontal sonic gradients. The method is tested on 3 cases with a sound speed profile in the form of

$$c_{eff}(x, z) = c_0 + a(x)z. \quad (7.1)$$

Thus, the sound speed profile is now a function of x and z .

7.1 Relevance of horizontal sonic gradients

A situation where horizontal sonic gradients may become important is when there is a variation in topology along the propagation distance. For example, consider a wind turbine placed close to a lake. The sound waves emitted by this turbine will first travel over the relatively flat water surface of the lake, and afterward, the sound waves will travel over land. This land can be a grain field, urban area, etc., which are all characterized by different surface roughness. Suppose the land is a grain field. A grain field has a surface roughness of about 0.4 m, whereas calm water has a roughness of about 0.0002 m [1]. With Monin-Obukhov theory, the corresponding effective sound speeds are calculated in the case of a stable atmosphere and a wind speed of 8 m/s at hub height. The different ground surfaces could also have an impact on the heat flux, but this is neglected here. The results are shown in figure 7.1. The two corresponding sound speed profiles in the figure are clearly different, and thus horizontal sonic gradients exist in this example. Other horizontal sonic gradients can occur as a result of obstacles that influence the wind profile and thus the effective sound speed profile.

7.2 Proposed method

The Harmonoise model uses conformal mapping to map ray paths to straight lines while curving the ground. This method is known as the curved ground analogy (see section 4.4.1). In other words, the method uses the curvature of a ray to curve the ground. It was found in chapter 4 that in the case of a vertical linear sonic profile, the rays are circular arcs with radius

$$R = \frac{c}{g \cos \theta}. \quad (4.37)$$

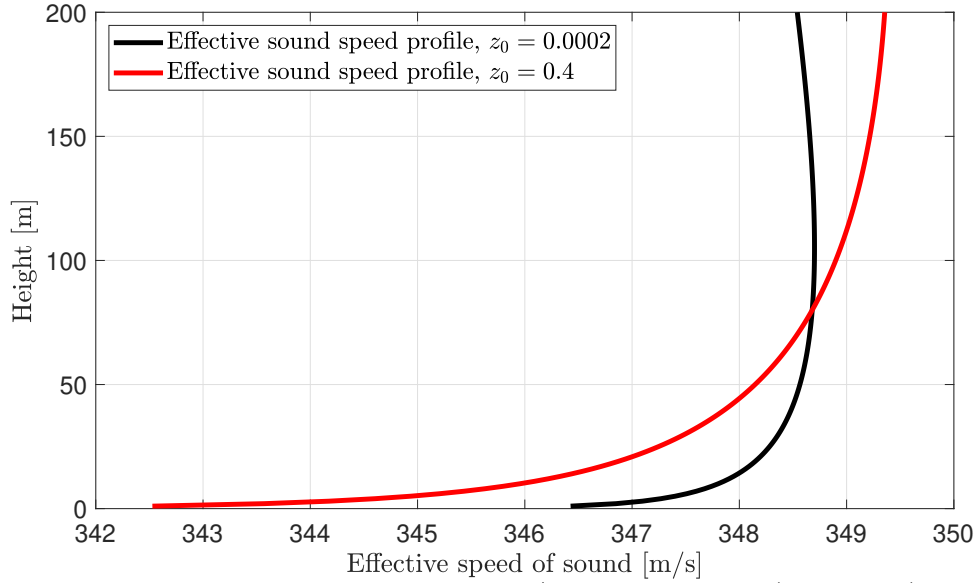


Figure 7.1: Effective sound speed profile with $U_0 = 8$ m/s over a grain field ($z_0 = 0.4$ m) and still water ($z_0 = 0.0002$ m).

This equation shows that the radius is dependent on the elevation angle, meaning that rays, leaving at a different angle from the source, have a different curvature and thus a different ray path. This is a problem since only one ray path can be used to curve the ground. However, for nearly horizontal propagation, the radii of the rays are only slightly different, and thus good results can be obtained. The conformal mapping used by the Harmonoise model uses the curvature of the ray with an elevation angle of 0 degrees from the source.

The question arises if this method can also be used in the case of a more complex sonic gradient. At the end of reference [34], it was suggested that non-constant gradients might be described by a variable curvature, thus varying the amount of curvature at different locations of the ground profile. To demonstrate this idea, consider a source placed in an xz plane at $(0, 5)$ m. The sound profile up to 37.5 m is described by $c_{eff} = c_0 + 0.05z$ meaning that there is a sonic gradient of 0.05 1/s. After 37.5 m, the sonic gradient is increased to 0.2 1/s, indicating that the sound profile changes to $c_{eff} = c_0 + 0.2z$. The ray path with elevation angle zero is computed, in this case, by “gluing” together two circular ray paths. Figure 7.2 shows this case. The ray path for constant sound speed gradient (red dotted line) is also shown in the figure, with the gradient being 0.2 1/s everywhere. The curvature of these ray paths can be used for the curved ground analogy. Figure 7.3 shows the corresponding curved ground for the ray paths of figure 7.2 in the case that the initial ground is flat. For this case, the receiver is placed at $(75 \text{ m}, h_r)$.

For this example, the source-receiver configuration is not taken into account. Ideally, the direct ray between the source and receiver is used as the curvature for the ground instead of the ray path with an elevation angle of zero from the source. However, in the case of a complex sound speed profile, it is not possible to compute the direct ray path analytically. If $h_s + h_r \ll d$, the propagation is nearly horizontal and the curvature of the ray path computed with a zero-degree elevation angle will be close to the curvature of the direct ray path. Therefore, this is a limitation of this approach.

7.3 Implementation

The method described in the previous part is implemented in the Matlab code. This is done by using a variable radius of curvature in the conformal mapping. The result of this is that a different mapping is used for every ground point, which takes into account the different curvature of the ray along the propagation direction.

A problem with this method arises from the fact that in the conformal mapping of the Harmonoise model, a correction is made to account for the source and receiver heights. This could be done because, for only a linear vertical sonic gradient, the direct ray path can be approximated analytically. If the same

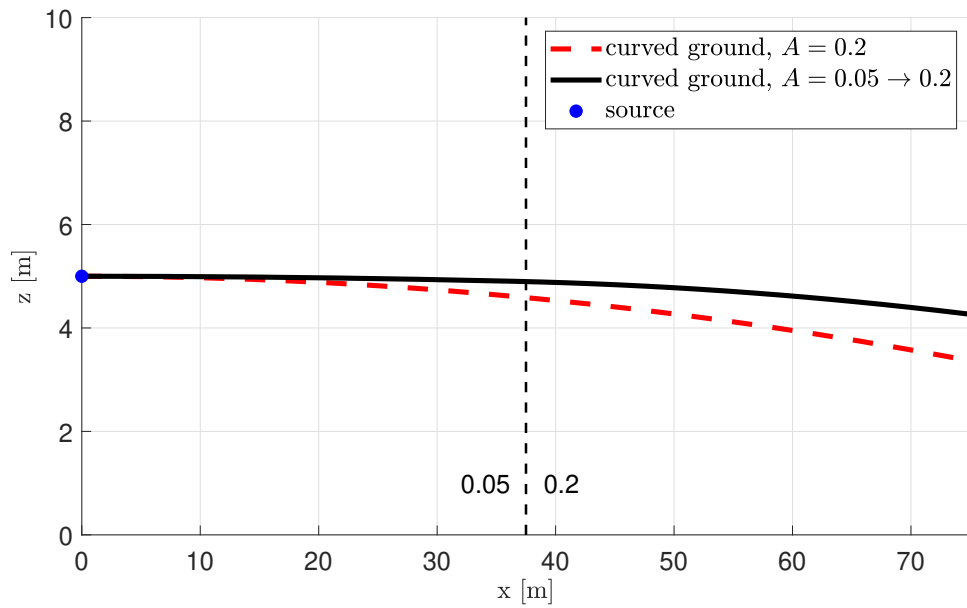


Figure 7.2: A ray path with a sound speed discontinuity at the interface ($x = 37.5$ m). The ray path for a constant gradient of 0.2 in the whole domain is shown by the red dotted line for comparison.

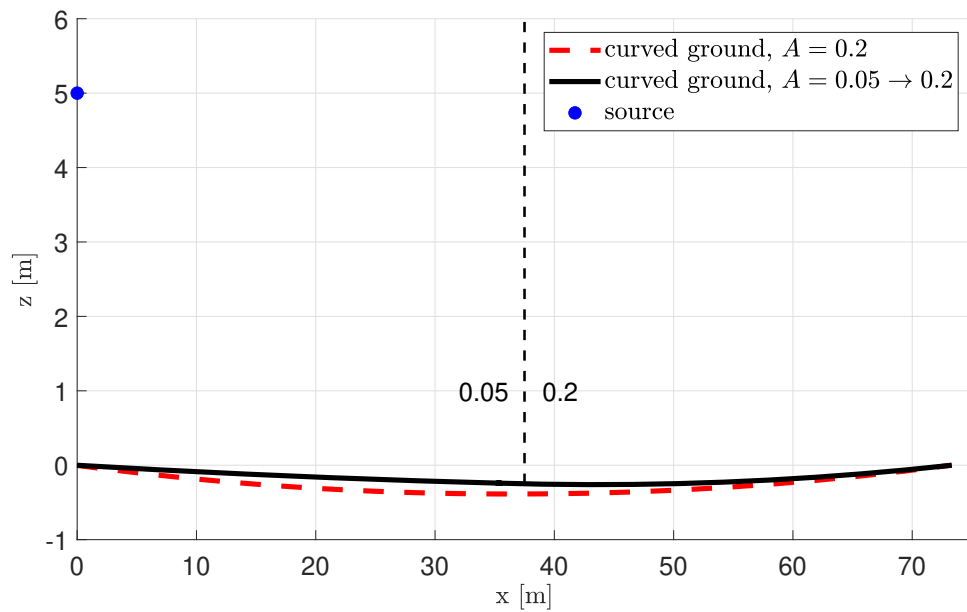


Figure 7.3: A flat ground curved with the curvature of the rays represented in figure 7.2.

approach is used in the case of variable curvature, a smooth ground profile is not guaranteed. Therefore, the conformal mapping is modified in such a way that the source and receiver heights are not taken into account. In future work, the source and receiver heights could be introduced again in a different fashion to possibly obtain slightly more accurate results. The new conformal mapping becomes

$$w = x + iz \quad \rightarrow \quad w' = x' + iz' \quad (7.2)$$

$$w' = \frac{C(x)(w - w_0)}{C(x) + (w - w_0)} \quad (7.3)$$

with,

$$w_0 = \frac{x_0 + x_N}{2} + i \frac{z_0 + z_N}{2}, \quad (7.4)$$

$$C(x) = iC_0(x) \quad (7.5)$$

$$C_0(x) = 2R(x). \quad (7.6)$$

This mapping is expected to work for flat and non-flat ground. The difference between the new conformal mapping and the one presented in section 4 is that the source and receiver heights are neglected ($h_s = h_r = 0$) and that the radius of curvature $R(x)$ is now a function of the x -coordinate. In this work, the proposed mapping is tested in three cases. In the future, an error analysis study could be done on this implementation by computing the phase differences between ray paths and the angle of incidence of a ray path before and after the transformation.

7.4 Results

The variable conformal mapping is applied to three cases. In all cases, $h_s = 0.75$ m, $h_r = 5$ m, $z_0 = 0.1$ m, $c_0 = 340$ m/s and $d = 75$ m. The parameters for the sound speed profile in all cases are:

Case E₁: $A = 0.05$ 1/s for $x = 0$ to 37.5 m and $A = 0.2$ 1/s for $x = 37.5$ to 75 m.

Case E₂: $A = 0.2$ 1/s for $x = 0$ to 37.5 m and $A = 0.05$ 1/s for $x = 37.5$ to 75 m.

Case E₃: $A(x) = \frac{0.2}{75}x$, i.e. a linear variation from $A(0) = 0$ to $A(75) = 0.2$ 1/s.

The results of these cases will be compared to two reference solutions. The first one is generated by ATMOS and will be referred to as GFPE. The second is calculated with the Harmonoise model using the average vertical sonic gradient. For example, in case E₁, the vertical sonic gradient is 0.05 for the first half and 0.2 for the second half, the reference case will thus be computed for a constant vertical sonic gradient of 0.125. This reference solution will be referred to as REF_B.

Figure 7.4 shows the results of case E₁. The result is in close agreement with the GFPE solution. The average sonic gradient solution REF_B also corresponds well with the GFPE solution. Figure 2 depicts the differences between the GFPE and Harmonoise solutions, as well as between the REF_B and GFPE solutions. The difference between the Harmonoise solution with variable sound speed gradient and the GFPE solution does not exceed 1 dB, while the difference of REF_B is 2.5 dB at some points. However, the low-frequency results are slightly better approximated by REF_B.

In case E₂, the vertical sonic gradients for the first and second halves of the propagation path are switched. Figure 7.6 shows the results. Again, both solutions agree well with the GFPE solution. The difference between both solutions and the GFPE solution is displayed in figure 7.7. The Harmonoise solution with the variable conformal mapping agrees overall slightly better than REF_B. In contrast with case E₁, the low frequencies are now better described by the new Harmonoise solution, but the improved accuracy compared to REF_B around 1200 Hz is reduced.

The final case is a linearly varying horizontal gradient instead of a sudden change at an interface. Figure 7.8 shows the results. In this case, the average sonic gradient is 0.1 1/s instead of 0.125 1/s. The solutions for the average sonic gradient and the horizontal sonic gradient are again in good agreement with the solution of the GFPE. The error for case E₃ is displayed in figure 7.9. At low frequencies, both solutions are very close to the solution of the GFPE. However, for this case, REF_B has an error of almost 4 dB at

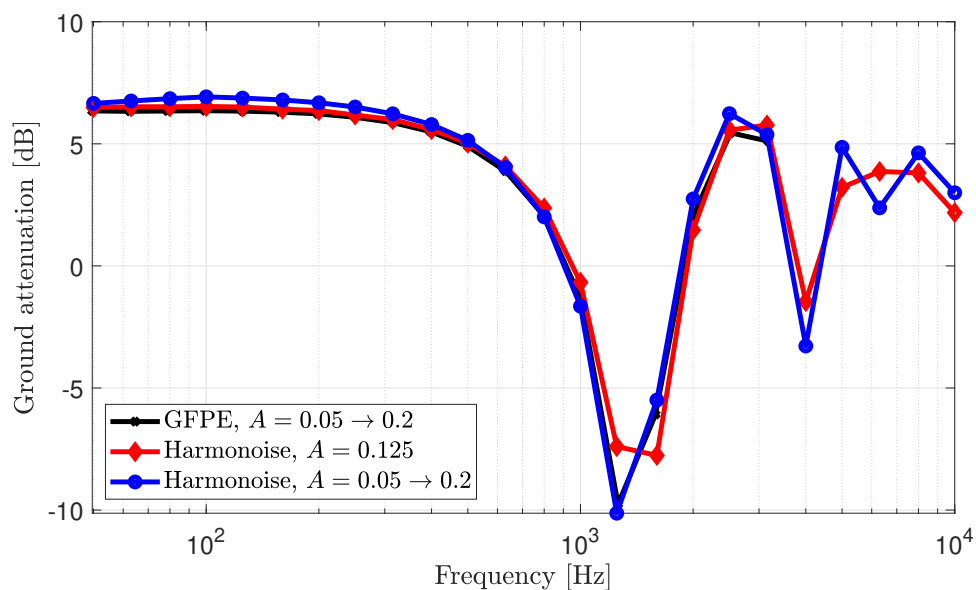


Figure 7.4: Ground attenuation for case E_1 computed with the GFPE solver ATMOS and the Harmonoise model using a variable conformal mapping. As a reference result the average vertical sonic gradient solution (REF_B) computed by the Harmonoise model is included.

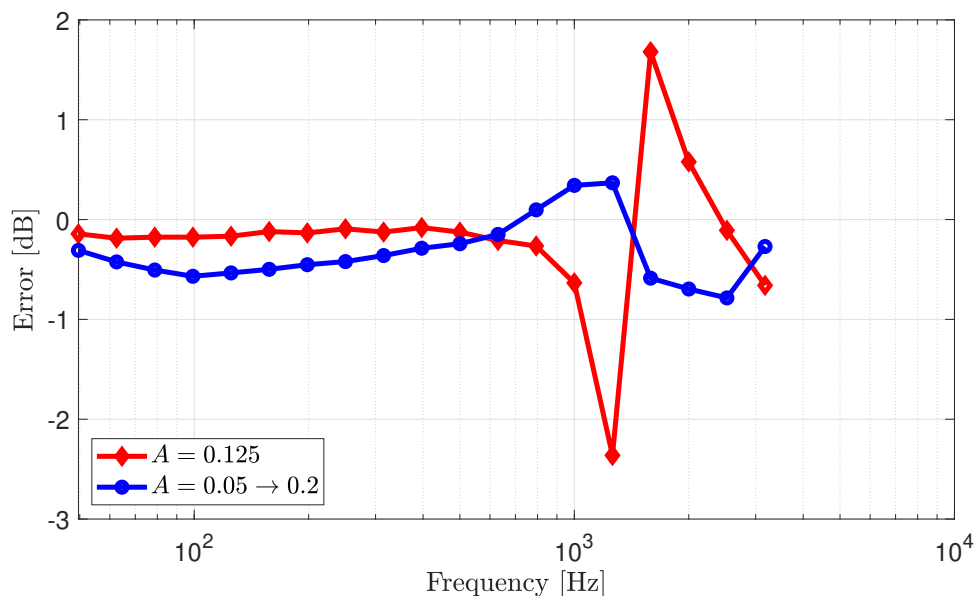


Figure 7.5: The difference of the Harmonoise model with a variable conformal mapping and the GFPE solution for case E_1 . Also the difference between the GFPE solution and the average vertical sonic gradient solution is shown.

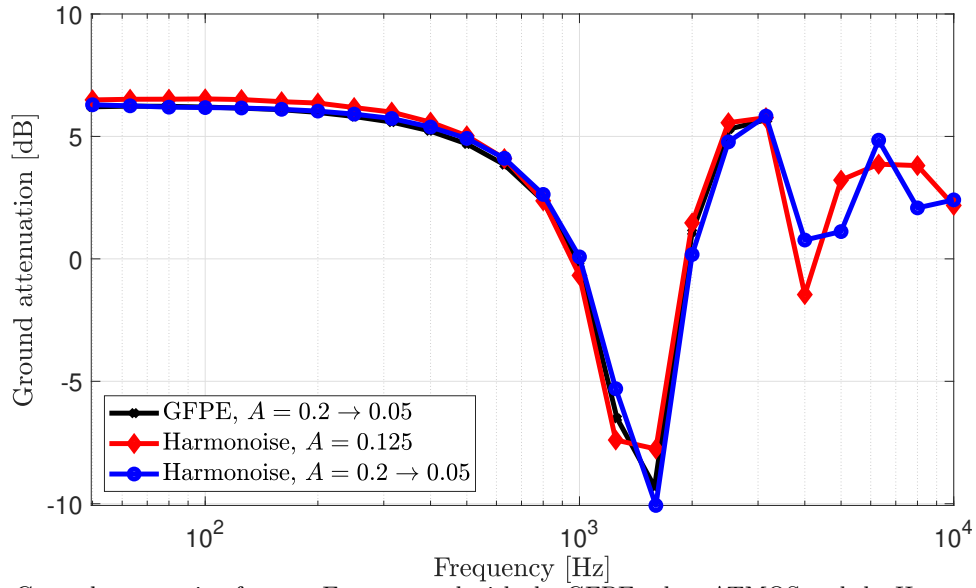


Figure 7.6: Ground attenuation for case E_2 computed with the GFPE solver ATMOS and the Harmonoise model using a variable conformal mapping. As a reference result the average vertical sonic gradient solution (REF_B) computed by the Harmonoise model is included.

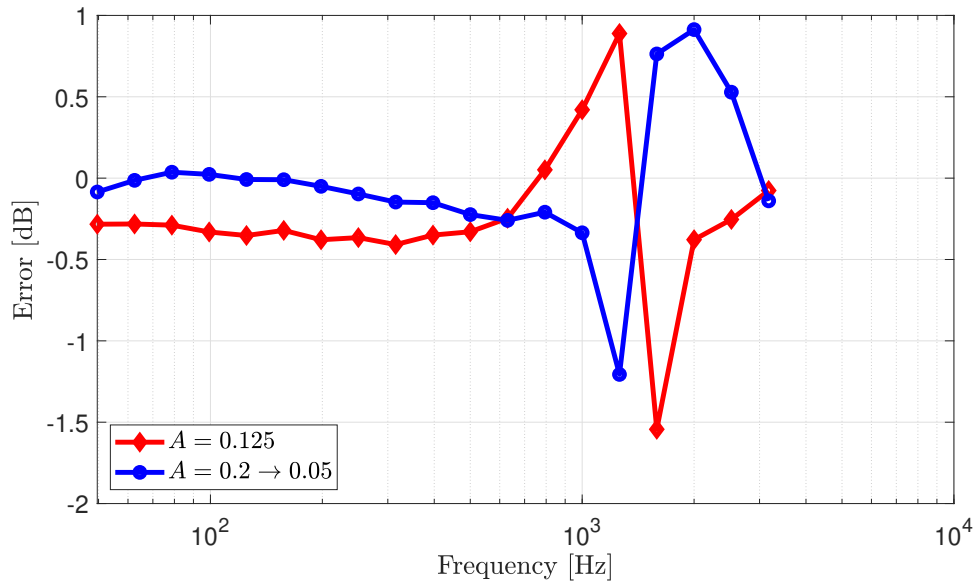


Figure 7.7: The difference of the Harmonoise model with a variable conformal mapping and the GFPE solution for case E_2 . Also the difference between the GFPE solution and the average vertical sonic gradient solution is shown.

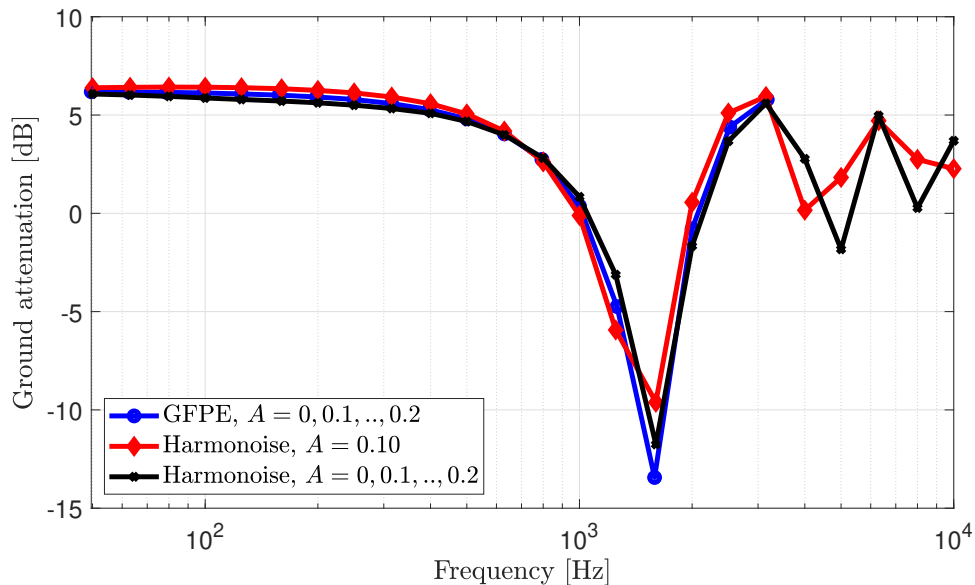


Figure 7.8: Ground attenuation for case E_3 computed with the GFPE solver ATMOS and the Harmonoise model using a variable conformal mapping. As a reference result, the average vertical sonic gradient solution (REF_B) computed by the Harmonoise model is included.

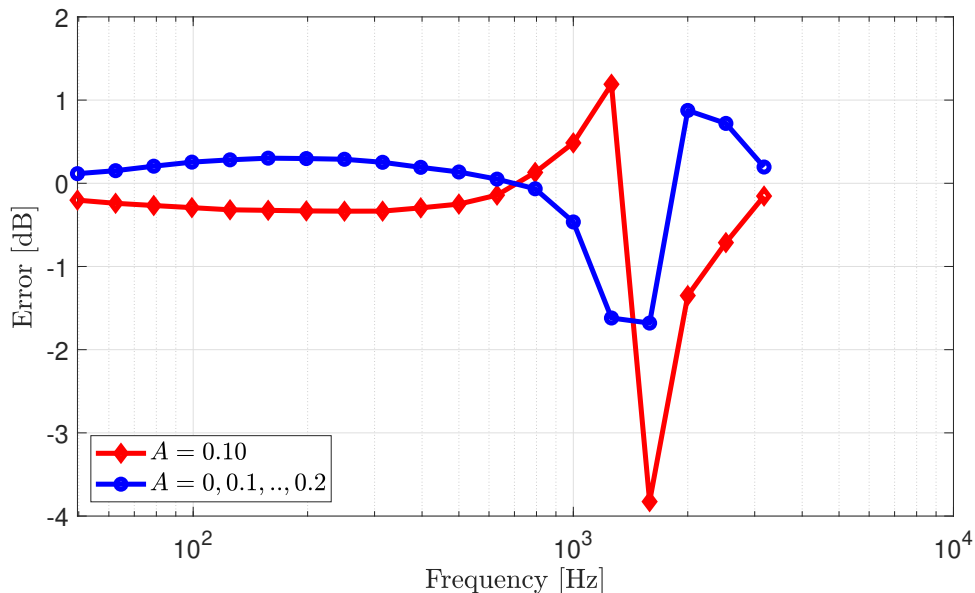


Figure 7.9: The difference of the Harmonoise model with a variable conformal mapping and the GFPE solution for case E_3 . Also the difference between the GFPE solution and the average vertical sonic gradient solution is shown.

approximately 1600 Hz, while the solution obtained with the variable conformal mapping remains well within 2 dB of the parabolic equation solution at all frequencies.

From these three cases, it can be concluded that in an atmosphere with a horizontal dependency on sound speed, ground attenuation can be accurately predicted by using a variable conformal mapping. It was also clear that a good prediction of the ground attenuation can be made by using the average vertical sonic gradient with a constant conformal mapping. However, in all cases considered, the variable conformal mapping produced slightly more accurate results than the constant conformal mapping with the averaged sonic gradient.

The cases considered are very similar to case C_1 of section 5.1.3. The only difference is that there is now a horizontal sonic gradient. Therefore, it is interesting to compare the accuracy of that case with the accuracy of the cases with a horizontal gradient. Case C_1 has a maximum error of 0.8 dB, while the largest error for the three cases in this section is approximately 1.6 dB. This shows that the overall error increases with respect to just a vertical sonic gradient. This is likely due to the fact that in the presence of horizontal gradients, the ray path is more dependent on elevation angle, and thus the system as a whole can be approximated less accurately by considering the curvature of one single ray.

This section showed the potential of using a variable ground curvature for the improvement of several cases and might also be of use to improve the prediction of vertical logarithmic sound speed profiles. The method should be validated further by applying it to a wider variety of scenarios, like non-flat ground, different distances, and different source and receiver height configurations.

Discussion & Conclusion

The Harmonoise model's ability to account for a moving atmosphere with temperature gradients is researched in this study. It is a potential improvement over the commonly used engineering model for wind turbine noise, the ISO9613-2 [18], which cannot predict the effect of a moving atmosphere with a temperature profile. It was found that the Harmonoise model can accurately describe these effects in cases of linearly dominant wind and temperature profiles. However, in the case of logarithmic profiles, the accuracy of the Harmonoise model was found to be limited. After that, the Harmonoise model was used in combination with a semi-analytical Amiet source model to study the sound propagation of a wind turbine in different conditions of atmospheric stability. This method enabled the generation of sound maps with low computational cost while capturing potential deviations due to different atmospheric stabilities. The influence of different atmospheric stabilities on the overall sound pressure level was found to be negligible, but the spectral noise content was affected. Finally, a method to include horizontal sonic gradients with the Harmonoise model was presented. This method demonstrates the possibility of improving results by modifying the ground profile. In the future, such an approach could possibly be used to improve the accuracy of vertical gradients. The results from chapters 5 and 6 are discussed below. The discussion of chapter 7 can be found at the end of that chapter.

The observation that the Harmonoise model cannot correctly predict logarithmic sound speed profiles was also a conclusion of [19], but, in that study, only low sources were considered. To evaluate the origin of the error, we have to look at the expected behavior of refraction due to logarithmic profiles. A logarithmic sound speed profile is characterized by large gradients at low altitudes and small gradients at high altitudes. Therefore, the ray paths will experience more refraction while traveling through the lower parts of the atmosphere. Because of this, the ray path does not follow the path of a circular arc anymore, which the Harmonoise model assumes. This causes a different path length, which explains the frequency shift between the Harmonoise results and the reference results that were seen in section 5.1. One can argue that the ray path traveling through a logarithmic sound speed profile is better described by a circular path than a straight path, indicating that it is an improvement compared to the assumption of no refraction. Also, since linear profiles are predicted with high accuracy (± 0.6 dB) the accuracy improves if the profile becomes more linearly dominated.

The overall sound pressure level around a wind turbine was shown to have the source's directivity pattern, with limited influence from atmospheric stability and propagation direction, up to 1500 meters. A few other studies looked into the effect of atmospheric stability on the overall sound pressure level. Two of them [60, 61] took on-site measurements near a wind turbine operating in a relatively flat area. They measured sound pressure levels while also monitoring wind shear. The conclusion of both studies was that atmospheric stability has no significant influence on overall sound pressure levels. A plausible reason for this is that a wind turbine is a high source, and the effects of the atmospheric stability only become relevant at further distances from the turbine, where the sound levels are already very low. An interesting finding of this work that deviated from previous literature was the fact that the sound propagation direction does not influence the overall sound pressure level. The presented overall sound pressure level sound map in section 6.4 shows almost perfect symmetry around the rotation plane of the wind turbine. This indicates that sound levels for upwind and downwind propagation are expected to be similar. Most models only consider the downward propagation direction because, generally, those are the conditions with the highest sound levels due to downward refraction. The fact that the overall sound pressure levels in this work are fairly similar between upwind and downwind conditions is due to the fact that the upwind conditions are not yet in the shadow region, indicating that both a direct ray and a reflected ray arrive. Not many studies have been performed on the effect of wind direction on the sound propagation in the case of wind turbine noise. One study did experimental measurements around

a wind turbine and found that sound levels upwind are 6-7 dBA lower than sound levels downwind at 1000 meters away from the turbine and 3-4 dBA at 500 meters [62]. In the study, they established that the emitted sound levels by the source in upwind and downwind directions were similar, thus the result can only be explained by propagation effects. This finding contradicts the results found in this work. One reason for this could be that the study conducted experimental measurements on a real-world site where topology can play a role. A small valley between the source and receiver was mentioned in the study, which could explain the difference. Another reason could be due to the limited accuracy of the Harmonoise model, although attenuation levels independent of wind direction close to the source can also be seen in figure 4.20 of [13].

The overall sound pressure level was not found to be influenced by atmospheric conditions, but the 1/3 octave band spectrum was found to be influenced by them. For a center frequency of 1000 Hz in a stable atmosphere, clear interference patterns were found that varied with the propagation direction. For a lower frequency of 63 Hz, this interference pattern is not observed, and the directivity pattern is again similar to the source. By comparing the noise spectrum for 5 different azimuth angles from downwind to upwind for 1000 Hz in a stable, unstable, and neutral atmosphere, it was found that the sound pressure levels can vary up to 15 dB at certain locations, while the overall sound pressure level only varies up to 3 dB. With the Harmonoise model's error in evaluating logarithmic profiles in mind, the actual value per frequency band is expected to shift. However, the distinct character of the noise spectrum as a result of atmospheric conditions persists.

A limitation of this work is the possible oversimplification of situations. The presence of barriers, different ground surfaces, and turbulence could have an effect on the effects caused by refraction. Also, due to uncertainty in the source model, uncertainty in the Harmonoise model, and the simplifications that were mentioned above, actual sound levels around a wind turbine could vary a lot in realistic situations. Comparing predicted sound levels to extensive on-site measurements is the best way to see if they are reasonable. However, in general, the atmospheric conditions around a wind turbine are very uncertain. Thus, it is hard to reproduce sound levels from experimental measurements.

To summarize, the following conclusions were found

- Overall sound pressure levels around a wind turbine are not much affected by atmospheric stability.
- The 1/3 octave sound pressure level is affected by atmospheric stability and wind direction.
- The Harmonoise model cannot accurately capture logarithmic profiles but can accurately capture linear profiles.
- Noise maps could be generated using aeracoustic coupling of the Harmonoise method and a semi-analytical Amiet method with low computational cost.
- More complex sonic gradients can potentially be approximated by using a variable conformal mapping.

Recommendations

This research found that atmospheric stability does not influence the overall sound pressure level but does affect the spectral noise content. Future research could examine the effect of the spectral noise content on the perceived sound levels by residents in the case of wind turbine noise. It could very well be the case that the stability of the atmosphere influences the level of annoyance experienced by residents.

The emphasis of this research was on sound speed gradients in the atmosphere. However, the method used for the wind turbine simulation could be applied in different circumstances. The next step could be to apply this method to different situations, e.g., a more complex ground surface.

Finally, the Harmonoise model was validated for several conditions. An improvement to the Harmonoise model could be made in terms of accuracy in the case of logarithmic sound speed profiles. Future research could try to make corrections to the modified ground profile, similar to what was done in chapter 7.

Bibliography

- ¹ C.H. Hansen, C.J. Doolan, and K.L. Hansen. *Wind Farm Noise: Measurement, Assessment, and Control*. Wiley Series in Acoustics Noise and Vibration. Wiley, 2017.
- ² Jeremy Orlof. Conformal transformations. *M.I.T. free course*.
- ³ How many wind turbines in the netherlands? <https://longreads.cbs.nl/the-netherlands-in-numbers-2022/how-many-wind-turbines-in-the-netherlands/>. Accessed: 2023-01.
- ⁴ North sea energy outlook establishes framework conditions for future growth of offshore wind energy. <https://www.government.nl/latest/news/2020/12/04/north-sea-energy-outlook-establishes-framework-conditions-for-future-growth-of-offshore-wind-energy>. Accessed: 2023-01.
- ⁵ Nathalie Dällenbach and Rolf Wüstenhagen. How far do noise concerns travel? exploring how familiarity and justice shape noise expectations and social acceptance of planned wind energy projects. *Energy Research & Social Science*, 87:102300, 2022.
- ⁶ L Gooijer and MG Mennen. Klimaataakkoord: effecten van nieuwe energiebronnen op gezondheid en veiligheid in nederland, 2021.
- ⁷ Vincent Harmsen Janine Bakker and Marco de Lange. Windmolenlawaai, 2022.
- ⁸ Phuc D. Nguyen, Kristy L. Hansen, Bastien Lechat, Peter Catchside, Branko Zajamsek, and Colin H. Hansen. Benchmark characterisation and automated detection of wind farm noise amplitude modulation. *Applied Acoustics*, 183:108286, 2021.
- ⁹ Chiu Chun-Hsiang, Shih-Chun Lung, Nathan Chen, and Jing-Shiang Hwang. Effects of low-frequency noise from wind turbines on heart rate variability in healthy individuals. 02 2021.
- ¹⁰ Irene van Kamp and Frits van den Berg. Health effects related to wind turbine sound: An update. *International Journal of Environmental Research and Public Health*, 18:9133, 08 2021.
- ¹¹ Jenni Radun, Henna Maula, Pekka Saarinen, Jukka Keränen, Reijo Alakoivu, and Valtteri Hongisto. Health effects of wind turbine noise and road traffic noise on people living near wind turbines. *Renewable and Sustainable Energy Reviews*, 157:112040, 2022.
- ¹² <https://www.who.int/europe/news-room/fact-sheets/item/noise>. Accessed: 2023-2.
- ¹³ E.M. Salomons. *Computational Atmospheric Acoustics*. Springer Netherlands, 2012.
- ¹⁴ S. Könecke, J. Hörmeyer, T. Bohne, and R. Rolfes. A new base of wind turbine noise measurement data and its application for a systematic validation of sound propagation models. *Wind Energy Science Discussions*, 2022:1–30, 2022.
- ¹⁵ Guillaume Dutilleux, Jérôme Defrance, David Ecotière, Benoit Gauvreau, Michel Bérengier, Francis Besnard, and Emmanuel Duc. Nmpb-routes-2008: The revision of the french method for road traffic noise prediction. *Acta Acustica united with Acustica*, 96:452–462, 05 2010.
- ¹⁶ K.J. Marsh. The concawe model for calculating the propagation of noise from open-air industrial plants. *Applied Acoustics*, 15(6):411–428, 1982.
- ¹⁷ B. Plovsing. Nord2000. Comprehensive Outdoor Sound Propagation Model. Technical report, Delta report, 2001.

-
- ¹⁸ Miloud Benmedjahed and Rachid Maouedj. Acoustic impact Assessment for the wind farm; using ISO 9613-2 Standard Method. In *Proc. of ICIREP2018, Spain.*, 4 2020.
- ¹⁹ Erik Salomons, Dirk Van Maercke, Jérôme Defrance, and Foort De Roo. The Harmonoise sound propagation model. *Acta Acustica united with Acustica*, 97(1):62–74, 2011.
- ²⁰ D.T. Blackstock. *Fundamentals of Physical Acoustics*. A Wiley-Interscience publication. Wiley, 2000.
- ²¹ Oleg Godin, Dmitry Mikhin, and S.Y. Molchanov. Effective sound speed approximation in the acoustics of moving media. *Izvestiya - Atmospheric & Oceanic Physics*, 29:179–186, 01 1993.
- ²² National Research Council. *Low-Frequency Sound and Marine Mammals: Current Knowledge and Research Needs*. The National Academies Press, Washington, DC, 1994.
- ²³ A.D. Pierce. *Acoustics – An Introduction to its physical principles and applications*. Acoustical Society of America, 1991.
- ²⁴ William C. Lane. *The interference of two coherent wave sources*. Michigan State University, 2000.
- ²⁵ F.B. Jensen, W.A. Kuperman, M.B. Porter, and H. Schmidt. *Computational Ocean Acoustics*. Modern Acoustics and Signal Processing. Springer New York, 2011.
- ²⁶ Keith Attenborough, Kai Ming Li, and Kirill Horoshenkov. *Predicting Outdoor Sound*. Taylor and Francis, 2007.
- ²⁷ Philippe Blanc-Benon. Outdoor sound propagation modelling in complex environments: Recent developments in the parabolic equation method. 10 2006.
- ²⁸ Kenneth Gilbert and Michael White. Application of the parabolic equation to sound propagation in a refracting atmosphere. *The Journal of the Acoustical Society of America*, 85:630–637, 02 1989.
- ²⁹ Jérôme Defrance, Erik Salomons, Ingrid Stuijt, Dietrich Heimann, Birger Plovsing, G.R Watts, Hans Jonasson, Xuetao Zhang, Eric Premat, Isabelle Schmich-Yamane, François-Edern Aballéa, Marine Baulac, and Foort Roo. Outdoor Sound Propagation Reference Model Developed in the European Harmonoise Project. *Acta Acustica united with Acustica*, 93:213–227, 03 2007.
- ³⁰ Dirk Van Maercke and Jérôme Defrance. Development of an Analytical Model for Outdoor Sound Propagation Within the Harmonoise Project. *Acta Acustica united with Acustica*, 93:201–212, 2007.
- ³¹ Eric W. Weisstein. Point-line distance–3-dimensional. From MathWorld–A Wolfram Web Resource. <https://mathworld.wolfram.com/Point-LineDistance3-Dimensional.html>.
- ³² Patrice Boulanger, Tim Waters-Fuller, Keith Attenborough, and Kai Ming Li. Models and measurements of sound propagation from a point source over mixed impedance ground. *The Journal of the Acoustical Society of America*, 102:1432–1442, 09 1997.
- ³³ D. C. Hothersall and J. N. B. Harriott. Approximate models for sound propagation above multi-impedance plane boundaries. *The Journal of the Acoustical Society of America*, 97(2):918–926, 1995.
- ³⁴ M. Almgren. Simulation by using a curved ground scale model of outdoor sound propagation under the influence of a constant sound speed gradient. *Journal of Sound and Vibration*, 118(2):353–370, 1987.
- ³⁵ Erik Foort de Roo Salomons. IMAGINE – Reference and Engineering Models for Aircraft Noise Sources. Technical report, IMAGINE Project., 01 2017.
- ³⁶ H. E. Bass, L. C. Sutherland, A. J. Zuckerwar, D. T. Blackstock, and D. M. Hester. Atmospheric absorption of sound: Further developments. *The Journal of the Acoustical Society of America*, 97(1):680–683, 1995.
- ³⁷ Rufin Makarewicz. Is a wind turbine a point source? (1). *The Journal of the Acoustical Society of America*, 129(2):579–581, 2011.
- ³⁸ B. Cotté. Coupling of an aeroacoustic model and a parabolic equation code for long range wind turbine noise propagation. *Journal of Sound and Vibration*, 422:343–357, 2018.

- ³⁹ David Ecoti re. Can we really predict wind turbine noise with only one point source? 6th International Meeting on Wind Turbine Noise, 04 2015.
- ⁴⁰ R. K. Amiet. Acoustic radiation from an airfoil in a turbulent stream. *Journal of Sound and Vibration*, 41:407–420, 1975.
- ⁴¹ Roy K. Amiet. Noise due to turbulent flow past a trailing edge. *Journal of Sound and Vibration*, 47(3):387–393, 1976.
- ⁴² Robert H Schlinker and Roy K Amiet. Helicopter Rotor Trailing Edge Noise. Technical report, NASA Contractor Report 3470, 1981.
- ⁴³ Michel Roger and St ephane Moreau. Broadband Self-Noise from Loaded Fan Blades. *AIAA Journal*, 42(3):536–544, 2004.
- ⁴⁴ St ephane Moreau and Michel Roger. Back-scattering correction and further extensions of Amiet’s trailing-edge noise model. Part II: Application. *Journal of Sound and Vibration*, 323(1-2):397–425, 2009.
- ⁴⁵ Yannick Rozenberg, Michel Roger, and St ephane Moreau. Rotating blade trailing-edge noise: Experimental validation of analytical model. *AIAA Journal*, 48(5):951–962, 2010.
- ⁴⁶ Korcan Kucukcoskun, Julien Christophe, Christophe Schram, and Michel Tournour. Broadband scattering of the turbulence- interaction noise of a stationary airfoil : experimental validation of a semi-analytical model. *International Journal of Aeroacoustics*, 12(1):85–104, 2013.
- ⁴⁷ Korcan Kucukcoskun, Julien Christophe, and Christophe Schram. Competing broadband noise mechanisms of a generic low-speed axial fan including acoustic scattering. *FAN 2015 - International Conference on Fan Noise, Technology and Numerical Methods*, 2015-April:1–12, 2015.
- ⁴⁸ M. Koch R. Sanjose and Moreau S. Large-eddy simulation and broadband acoustic prediction of an helicopter rotor in hover. *28th AIAA/CEAS Aeroacoustics Conference, Southampton, 2022*, 2022.
- ⁴⁹ Yuan Tian and B. Cott e. Wind turbine noise modeling based on Amiet’s theory: Effects of wind shear and atmospheric turbulence. *Acta Acustica united with Acustica*, 102(4):626–639, 2016.
- ⁵⁰ Cansev K uukosman. *Semi-analytical approaches for the prediction of the noise produced by ducted wind turbines*. PhD thesis, TU Delft University, 2019.
- ⁵¹ Franck Bertagnolio, Helge Aa Madsen, Andreas Fischer, and Christian Bak. A semi-empirical airfoil stall noise model based on surface pressure measurements. *Journal of Sound and Vibration*, 387:127–162, 2017.
- ⁵² Samuel Sinayoko and Jeremy Hurault. On predicting wind turbine noise and amplitude modulation using Amiet’s theory. In *6th International Conference on Wind Turbine Noise*, number April 2015, pages 1–15, 2015.
- ⁵³ A. P. C. Bresciani, U. Boatto, S. Le Bras, P. Bonnet, and L. D. de Santana. Influence of blade deflections on wind turbine noise directivity. *Journal of Physics: Conference Series*, 2257(1):012012, apr 2022.
- ⁵⁴ Michael Goody. Empirical spectral model of surface pressure fluctuations. *AIAA Journal*, 42(9):1788–1794, 2004.
- ⁵⁵ Yannick Rozenberg, Gilles Robert, and St ephane Moreau. Wall-pressure spectral model including the adverse pressure gradient effects. *AIAA Journal*, 50(10):2168–2179, 2012.
- ⁵⁶ Mark Drela. Xfoil: An analysis and design system for low reynolds number airfoils. In Thomas J. Mueller, editor, *Low Reynolds Number Aerodynamics*, pages 1–12, Berlin, Heidelberg, 1989. Springer Berlin Heidelberg.
- ⁵⁷ Maxime Malbois. Etude de la g en eration et de la propagation du bruit d’une  olienne. *D epartement a eroacoustique, facult e de g enie de l’Universit e de Sherbrooke*, 2022.

-
- ⁵⁸ Christophe J., Le Bras S., Chavez R., Vidal J., Panjwani B., and Samseth J. Application of the coupled atmospheric- aeroacoustic simulation platform to a wind farm benchmark. *UPWARDS Deliverable D4.5*, 2022.
- ⁵⁹ Yasuaki Okada, Koichi Yoshihisa, Kazuki Higashi, and Naoto Nishimura. Horizontal directivity of sound emitted from wind turbines. *Acoustical Science and Technology*, 37:239–246, 09 2016.
- ⁶⁰ J. Cooper, T. Evans, and V. Alamshah. Influence of non-standard atmospheric conditions on turbine noise levels near wind farms. *InterNoise*, 01 2014.
- ⁶¹ T. Evans and J. Cooper. Effects of different meteorological conditions on wind turbine noise. pages 446–454. *Proceedings of Acoustics*, 01 2013.
- ⁶² Tom Evans and Jonathan Cooper. Influence of wind direction on noise emission and propagation from wind turbines. *Proceedings of Acoustics*, 2012.
- ⁶³ Ameya Sathe, J Mann, Julia Gottschall, and Michael Courtney. Estimating the systematic errors in turbulence sensed by wind lidars. Technical report, RISO National Laboratory, 10 2010.
- ⁶⁴ A. L’Espérance, J. Nicolas, D.K. Wilson, D.W. Thomson, Y. Gabillet, and G. Daigle. Sound propagation in the atmospheric surface layer: Comparison of experiment with FFP predictions. *Applied Acoustics*, 40(4):325–346, 1993.
- ⁶⁵ Matlab curve-fitting toolbox. <https://nl.mathworks.com/products/curvefitting.html>. Accessed: 2022-10-8.
- ⁶⁶ R.J. Urick. *Principles of Underwater Sound*. Peninsula Publishing, 1983.
- ⁶⁷ Val Schmidt. raytrace, MATLAB Central File Exchange., 2022.
- ⁶⁸ E. van der Weide. Lecture notes FNM. 2021.
- ⁶⁹ François-Edern Aballéa and Jérôme Defrance. Single and multiple reflections in plane obstacle using the parabolic equation method with a complementary kirchhoff approximation. *Acta Acustica united with Acustica*, 93:22–30, 01 2007.
- ⁷⁰ Jennifer L. Cooper and David C. Swanson. Parameter selection in the green’s function parabolic equation. *Applied Acoustics*, 68(4):390–402, 2007.

Appendix A

Atmospheric absorption

In accordance with ANSI/ASA S1.26(2014), the atmospheric absorption attenuation parameter α , which represent the attenuation per meter in dB, can be calculated using [1]

$$\begin{aligned} \alpha = 8.686f^2 \left\{ \right. & \left. 1.84 \times 10^{-11} \left(\frac{\bar{p}_a}{p_r} \right)^{-1} \left(\frac{T}{T_r} \right)^{1/2} \right. \\ & + \left(\frac{T}{T_r} \right)^{-5/2} \times \left[0.01275e^{-2239.1/T} \left(\frac{f_{ro}}{f_{ro}^2 + f^2} \right) \right. \\ & \left. \left. + 0.1068e^{-3352/T} \left(\frac{f_{rN}}{f_{rN}^2 + f^2} \right) \right] \right\} \quad (\text{dB/m}), \end{aligned} \quad (\text{A.1})$$

where T is the ambient atmospheric temperature in Kelvin, T_{ref} is the reference temperature, p_a the ambient atmospheric pressure, p_r the reference pressure,

$$f_{ro} = \left(\frac{p_a}{p_r} \right) \left[24 + \left(\frac{(4.04 \times 10^4 h)(0.02 + h)}{0.391 + h} \right) \right] \quad (\text{A.2})$$

and

$$f_{rN} = \left(\frac{T}{T_r} \right)^{-1/2} \left(\frac{p_a}{p_r} \right) \left\{ 9 + 280he^{-4.170[(T/T_r)^{-1/3}-1]} \right\} \quad (\text{A.3})$$

where h is the molar concentration of water vapor which may be calculated from the relative humidity, h_{rel} by

$$h = h_{rel} \left(\frac{p_{sat}}{p_r} \right) \left(\frac{p_a}{p_r} \right)^{-1} \quad (\text{A.4})$$

with

$$\frac{p_{sat}}{p_r} = 10^V \quad (\text{A.5})$$

and

$$V = -6.8346 \left(\frac{273.16}{T} \right)^{1.261} + 4.6151. \quad (\text{A.6})$$

Appendix B

Analytical solution in a homogeneous atmosphere above a fully reflecting plane

Let us consider a source above a fully reflecting plane in a homogeneous atmosphere (no refraction). In that case, exactly two rays reach the receiver: the direct ray and one reflected ray. With the imaginary source method, the path length of the reflected ray can be calculated by placing a source mirrored by the plane beneath the actual source (see figure B.1).

The pressure at the receiver is now given by the combination of the direct wave and the reflected wave [13]

$$p_c = S \frac{\exp(ikr_1)}{r_1} + QS \frac{\exp(ikr_2)}{r_2}, \quad (\text{B.1})$$

where r_1 is the direct ray's path length and r_2 is the reflected ray's path length, which is $r_s + r_r$ in the figure. The two terms in equation B.1 represent the direct ray and the reflected ray, respectively. In the case of a fully reflective ground, Q is set to 1.

The ground attenuation is the relative sound pressure level which was defined as

$$\Delta L = 10 \log_{10} \left(\frac{|p_c|^2}{|p_{\text{free}}|^2} \right) \quad (2.36)$$

where p_c is defined by equation B.1 and $p_{\text{free}} = S \frac{\exp(ikr_1)}{r_1}$.

The 1/3 octave band spectrum can be calculated by

$$\Delta L(f_c) = 10 \log_{10} \left(\frac{1}{N} \sum' 10^{\Delta L(f)/10} \right). \quad (2.37)$$

where the number of frequencies per band should be reasonably large.

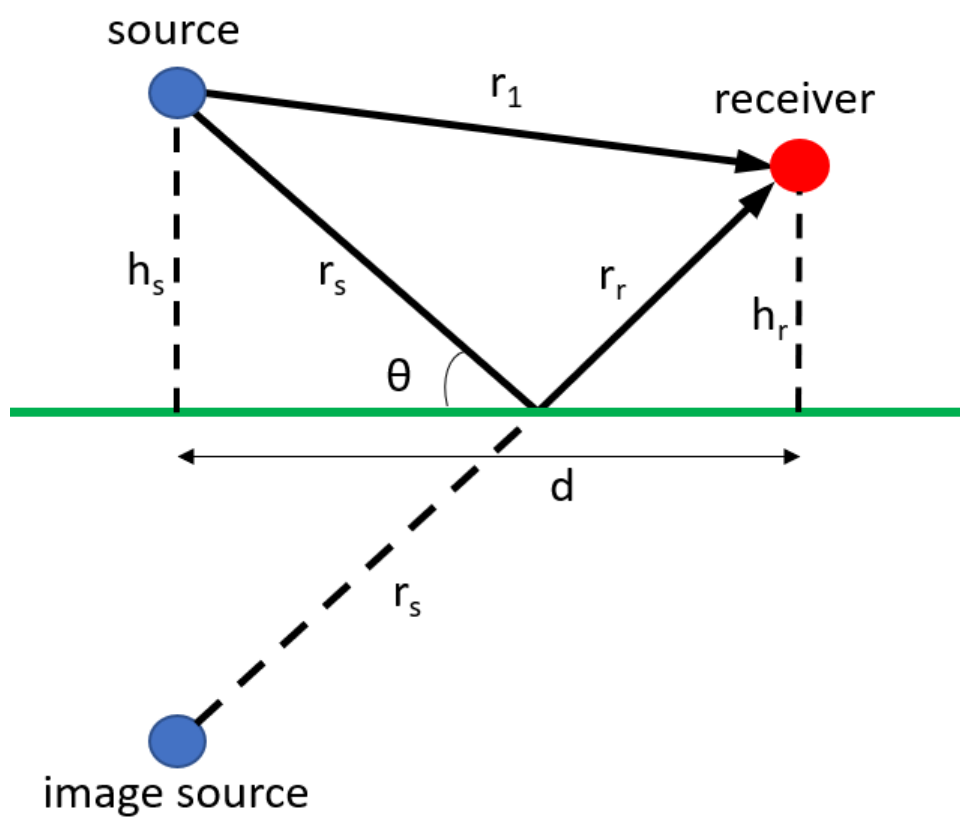


Figure B.1: Image source method used to calculate the ground attenuation for a non-refracting atmosphere.

Appendix C

Sound speed profiles in the atmosphere

The speed of sound is a function of temperature and wind. Temperature and wind profiles can vary significantly over time in the earth's atmosphere. Usually, one can identify three types of atmospheric conditions: stable, unstable, and neutral. These conditions, in combination with the actual magnitude of the wind speed at a certain height, the temperature at ground level, and the "roughness" of the ground, can be used to predict the wind and temperature profiles. In this section, a formulation is introduced to predict the wind and temperature profiles for different atmospheric stabilities. From these profiles, the effective sound speed can be obtained.

The lower part of the earth's atmosphere is directly influenced by its surface and is called the atmospheric boundary layer. These surface effects include friction forces caused by moving air and heat transfer from the ground to the atmosphere. Earth's atmospheric boundary layer can be divided into two different regions: the surface, or the Prandtl layer, and the Ekman layer. Above these layers exists the free atmosphere, which can be thought of as a layer that is not influenced by the ground. The surface layer is valid up to approximately 100 meters, which is the region of relevance in this report. Although the Ekman layer can be irregular and hard to predict, the surface layer is quite predictable. The latter is done by the Monin-Obukhov similarity theory, as described at the end of this section.

C.1 Surface layer

The wind profile is a vector with three components, the direction at which this vector points is called the wind direction. The wind direction is usually a function of height, but in the surface layer this variation is small. Therefore, the vertical component of the wind profile is approximated as zero. This report only looks at 2D propagation. The coordinate system is chosen in such a way that the wind direction will consist of a horizontal vector with only one component. Although the vertical component of the wind is small, the variation in wind velocity with respect to height is not small. Friction slows air at the earth's surface to approximately 0 m/s. As a result, wind velocity increases with height. One parameter that influences the wind velocity variation with height is the surface roughness parameter, z_0 . This parameter varies from 0.002 to 2 meters depending on the type of surface, where 0.002 m is a very flat surface like still water and 2 m is a very rough surface like a landscape with tall buildings.

Two important parameters of the temperature profile are the decrease of pressure with height and heat exchange between the air and the ground. The pressure decreases with height, which causes a decrease in temperature. The temperature drop due to the drop in pressure can be approximated with the adiabatic gas approximation [13]

$$\alpha_0 \equiv \frac{dT}{dz} = -\frac{\gamma - 1}{\gamma} \frac{\rho T}{\bar{p}} g, \quad (\text{C.1})$$

where z is the height [m], T the temperature [K], γ the adiabatic index [-], ρ the air density [$\frac{kg}{m^3}$], g gravitational acceleration [$\frac{m}{s^2}$] and \bar{p} is the atmospheric pressure [Pa]. Filling in some standard quantities for air $\rho = 1.2 \frac{kg}{m^3}$, $\bar{p} = 10^5$ Pa, $T = 300$ K, $g = 9.81 \frac{m}{s^2}$, $\gamma = 1.4$ leads to $\alpha_0 \approx -0.01$ meaning that every

100 meters the temperature drops with approximately 1 degree. Humidity can cause deviations from this value, but the changes are small enough to be neglected.

We define the potential temperature as [13]

$$\theta \approx T - \alpha_0 z. \quad (\text{C.2})$$

This equation describes the temperature with respect to height caused by the pressure decrease.

Another factor that influences the temperature is the heat exchange between the air and the ground. During the day, the surface of the earth heats up because of solar radiation, and during the night, the ground gets cooled. This leads to a decrease in potential temperature with height during the day and an increase with height during the night. The latter can lead to a temperature inversion, where the actual temperature increases with height. This effect is heavily influenced by cloud cover, wind speed, and time. The heat exchange between the ground and the air is determined by various transport processes. One of these transport processes is caused by buoyance and gravity. Warmer air expands and thus rises in the atmosphere, causing it to transport heat to higher altitudes. The upward movement of air is accompanied by the downward movement of cooler air in the atmosphere. This causes the air to go in circles, which can be seen as turbulent eddies. Another transport process is caused by atmospheric turbulence. In that case, the air is mixed by wind velocity fluctuations.

To distinguish the various cases of heat exchange between the ground and air, the atmosphere can be classified as unstable, stable, or neutral. During the day, when the ground is heated and heat is transferred from the ground to the air, the atmosphere is considered unstable. When the heat transfer is close to zero, the atmosphere is classified as neutral. And during the night, when heat is transferred from the air to the ground, the atmosphere is considered stable. Thus, in an unstable atmosphere, there is a positive heat flux. In a neutral atmosphere, there is almost no heat flux. And in a stable atmosphere, there is a negative heat flux.

C.2 Similarity theory

From empirical relations of dimensionless quantities, relations for the wind and temperature profiles are derived. These relations are called similarity relations and are a good approximation for the surface layer.

The equations for the wind and potential temperature profiles are [13]

$$\begin{aligned} \bar{u}(z) &= \frac{u_*}{\kappa} \left[\ln \frac{z}{z_0} - \psi_w \right] \\ \bar{\theta}(z) &= \theta_0 + \frac{\theta_*}{\kappa} \left[\ln \frac{z}{z_0} - \psi_t \right] \end{aligned} \quad (\text{C.3})$$

with

$$\theta_* = \frac{-(w'\theta')_s}{u_*} \quad (\text{C.4})$$

where $w'\theta'$ represents the vertical heat flux with the eddies evaluated near the ground surface. u_* is the friction velocity, θ_* the temperature and $\kappa = 0.41$ the von Karman constant. The dimensionless quantities ψ_w and ψ_t are functions of height and Obukov length L which will be defined by equation C.8

$$\begin{aligned} \psi_w &= 2 \ln \frac{1+x}{2} + \ln \frac{1+x^2}{2} - 2 \arctan x + \frac{\pi}{2} & \text{for } L^{-1} < 0 \\ \psi_w &= -5z/L & \text{for } L^{-1} > 0 \end{aligned} \quad (\text{C.5})$$

$$\begin{aligned} \psi_t &= 2 \ln \frac{1+x^2}{2} & \text{for } L^{-1} < 0 \\ \psi_t &= -5z/L & \text{for } L^{-1} > 0 \end{aligned} \quad (\text{C.6})$$

with $x = (1 - 16z/L)^{1/4}$.

These relations are called the Businger-Dyer relations. Later some corrections were made that slightly improved the approximation of the stable atmosphere [13]

$$\begin{aligned} \psi_w &= \psi_t = -5z/L & \text{for } z/L \leq 0.5 \\ \psi_w &= \psi_t = -7 \ln(z/L) - \frac{4.25}{z/L} + \frac{0.5}{(z/L)^2} - 0.852 & \text{for } z/L > 0.5. \end{aligned} \quad (\text{C.7})$$

For a neutral atmosphere ψ_t and ψ_w are zero.

The Obukhov length is defined by:

$$L = -\frac{\bar{\theta} u_*^3}{\kappa g (w'\theta')_s}. \quad (\text{C.8})$$

The Obukov length can be regarded as a measure of stability. For $L < 0$ the atmosphere is considered unstable, for $0 > L > 500$ the atmosphere is stable where close to 0 is highly stable and close to 500 almost neutral, and when $L > 500$ the atmosphere is neutral [63].

To generate the profiles, the roughness length, stability criterion, heat flux or Obukhov length, the temperature of the surface, and wind velocity at a certain height need to be prescribed. A first approximation of u_* can then be determined by assuming neutral conditions at first and calculating it with the prescribed wind velocity using the formula C.3. Then iterate several times until u_* remains stable. Afterwards, θ_* can be determined with equation C.4 and equation C.8 [64].

Figure C.1 shows the wind velocity, temperature, and effective sound speed profile for an unstable, stable, and neutral case. It can be seen that in the stable case, the temperature rises for the first few meters, this is called temperature inversion. The effective sound speed profile in the stable case has the greatest gradients, implying the largest refraction. The effective sound speed profile in the unstable case has both positive and negative gradients, indicating upward and downward refraction.

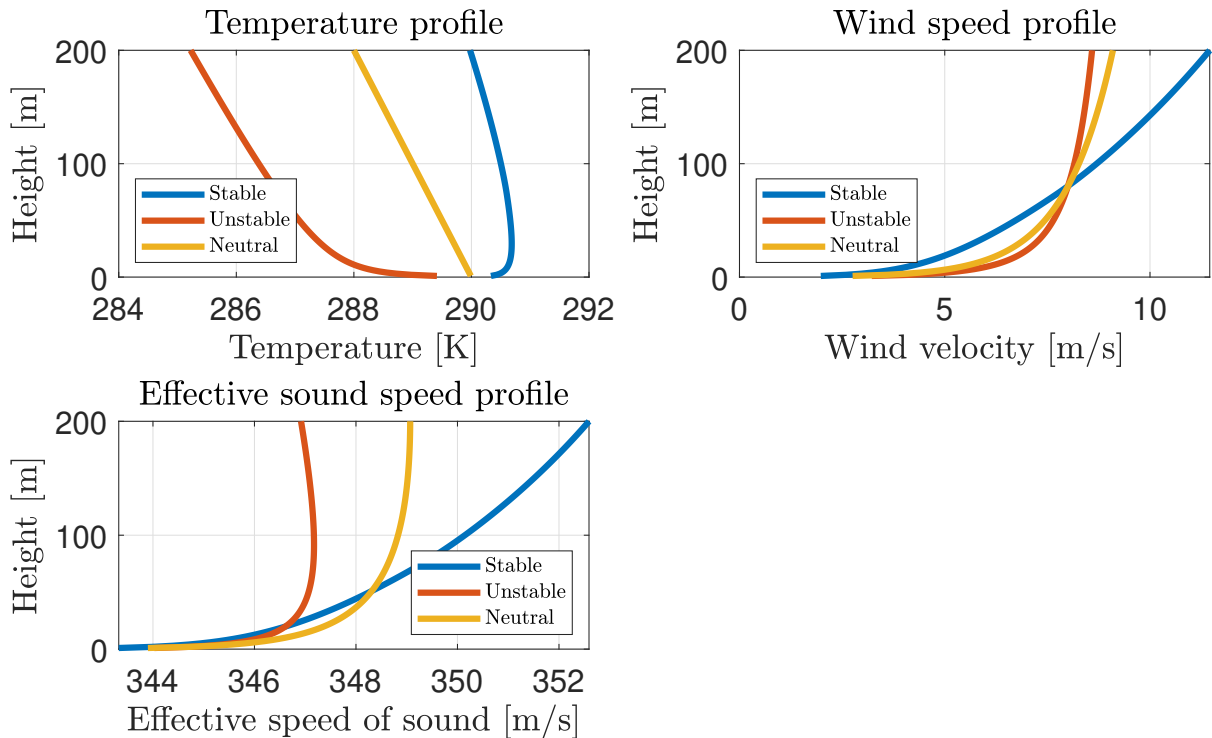


Figure C.1: Temperature, velocity and effective sound speed profiles for a stable, an unstable and neutral atmosphere. Generated with $U = 8$ m/s at 80 meter, $z_0 = 0.1$, $T_s = 290K$ and Obukhovs lengths of 145,-86 and infinity respectively

The Harmonoise model takes as input a lin-log sound speed profile. Therefore, a calculated sound speed profile by similarity theory is fitted into a lin-log profile. The fitting is performed with the Matlab curve-fitting toolbox. The toolbox uses a combination of non-linear regression algorithms and can be used to fit data in a log-lin formula [65]. The fit is rather good, with only a tiny deviation from the actual curve. Figure C.2 shows the fitted lin-log profile on a sound speed profile that is generated with similarity theory for a stable case.

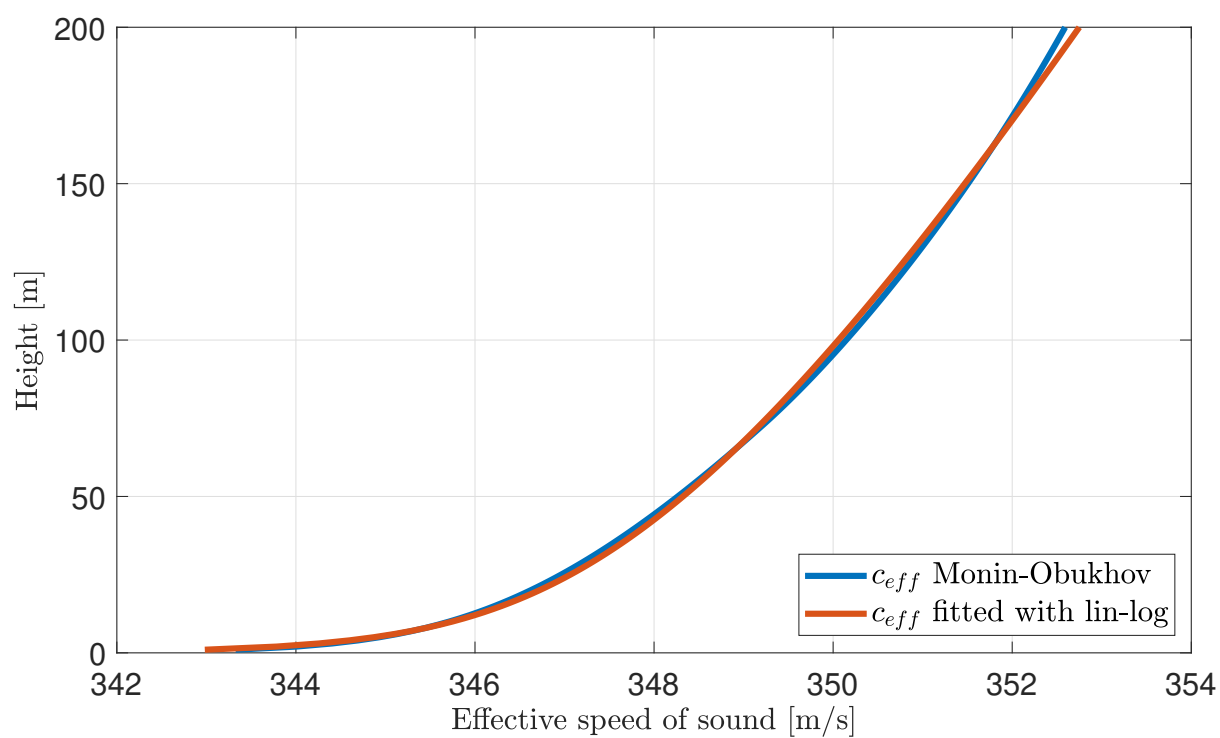


Figure C.2: Effective sound speed profile in case of a stable atmosphere fitted for the equation $c_{eff} = c_0 + Az + B \log(1 + \frac{z}{z_0})$.

Appendix D

Ray paths

Let us consider a sound source that produces a pressure wave with an arbitrary wavefront. The wavefront is a line in space where the amplitude and phase of the pressure are equal. For a plane wave, this is along a plane in space, but it could also be, for example, a curved front in the case of a spherical wave. If this wavefront exists in a fluid at rest, its propagation direction is \mathbf{n} , which is the vector perpendicular to the front. The velocity of the wavefront is c . Now let us consider that the fluid gets a velocity \mathbf{v} , because of this the propagation direction of the wavefront is not necessarily \mathbf{n} anymore for a stationary observer. We define $\mathbf{x}_P(t)$ as a point that moves along with the wavefront (see figure D.1), this can only be the case if the velocity of the point is a combination of the speed of the wavefront and the speed of the fluid [23]:

$$\frac{d\mathbf{x}_P}{dt} = \mathbf{v}(\mathbf{x}_P, t) + \mathbf{n}(\mathbf{x}_P, t) c(\mathbf{x}_P, t) = \mathbf{v}_{\text{ray}}. \quad (\text{D.1})$$

The path that the point $\mathbf{x}_P(t)$ makes is called a ray path. For inhomogeneous media \mathbf{n} changes along the ray path, thus the sound wave refracts (see section 3.1.4). A way to compute ray paths in case of a layered atmosphere is discussed below.

D.1 Tracing ray paths in a layered atmosphere

The atmosphere is called a layered atmosphere if the sonic gradient can be regarded as a function of height only [13]. It can be shown that for a linear sound speed gradient, all ray paths in the layered atmosphere are circular arcs. This can be done by connecting two arbitrary points in space with an arc, assuming linear sound speed gradients, and forcing the arc to be a ray by satisfying Snell's law (see [66]). The radius of the ray is defined by [1, 66]

$$R(q) = \frac{-c(q)}{g(q) \cos \theta(q)} \quad (\text{D.2})$$

where $R(q)$ is the radius of the circular ray path, $c(q)$ is the speed of sound in layer number q , $g(q)$ is the gradient of layer number q and $\theta(q)$ is the angle with which the ray enters the layer. The speed of sound profile in the atmosphere can be approximated by piece-wise linear gradients. Under that assumption, rays travel through a layer as a circular arc described by equation D.2. The ray path can be traced by determining the paths in all layers of the atmosphere.

Figure D.2 shows the ray path for a single layer. The gradient of this layer can be calculated by

$$g(q) = \frac{c(q+1) - c(q)}{dz}, \quad (\text{D.3})$$

where $c(q+1)$ is the speed of sound in layer number $q+1$ and dz is the vertical step length. From figure D.2 one can obtain the following relation for dx and dz [67]

$$dx(q) = R(q) [\sin(\theta(q+1)) - \sin(\theta(q))] \quad (\text{D.4})$$

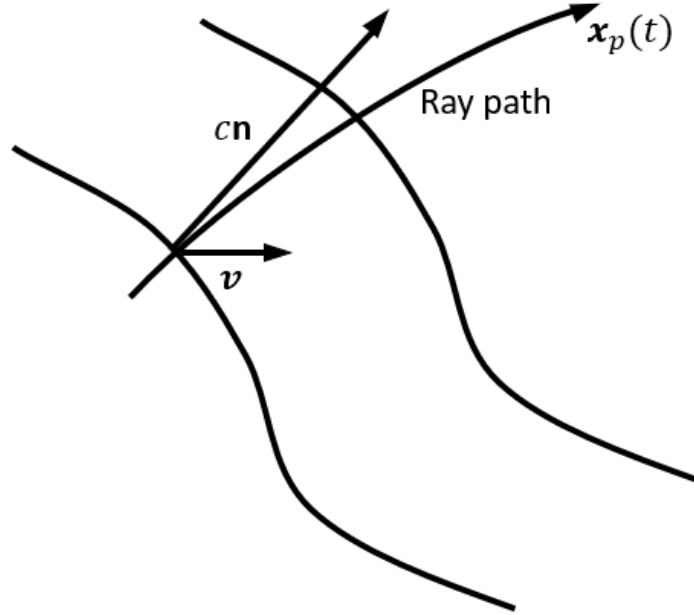


Figure D.1: Two wavefronts occurring at different times. The variable $\mathbf{x}_p(t)$ is a point that moves along with the wavefront. The path of the function $\mathbf{x}_p(t)$ is called a ray path.

$$dz(q) = R(q) [\cos(\theta(q)) - \cos(\theta(q+1))]. \quad (\text{D.5})$$

Equation D.5 can be used to obtain the relation for the exiting angle of the ray after a step dz

$$\theta(q+1) = \arccos\left(\cos(\theta(q)) - \frac{dz(q)}{R(q)}\right). \quad (\text{D.6})$$

After this, the dx and the $R(q)$ can be determined for the next layer, and thus with equations D.2, D.4 and D.6 the ray path can be found by iteration. The only thing that still needs to be considered is that a ray has a turning point. The turning point is found when θ becomes zero. After the turning point, the ray travels in the opposite vertical direction. This can be accounted for by flipping the sign of the vertical step.

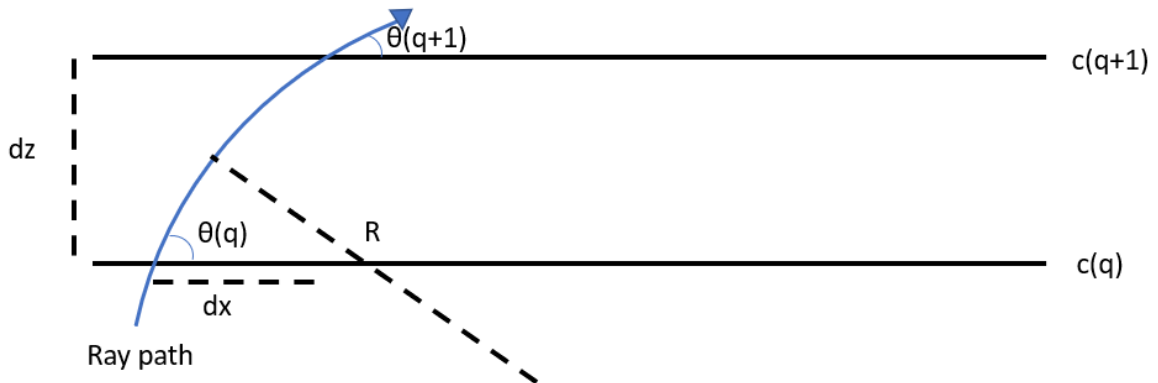


Figure D.2: Ray path through a single layer of the atmosphere under the assumption of piece-wise linear approximation of the sound speed profile.

Appendix E

Parabolic equation method

The parabolic equation method (PE) computes the sound field by solving a parabolic equation. This appendix starts by showing how a parabolic equation can be derived from the wave equation and what a parabolic equation is. After that, several numerical methods for solving parabolic equations are discussed. Finally, the parabolic equation solver ATMOS, which uses one of these numerical methods, is described. The description focuses on practical use rather than detailed mathematics.

E.1 Derivation of the narrow angle parabolic equation

By the use of the axisymmetric approximation the 3D Helmholtz equation reduces to [13]

$$\frac{\partial^2 q_c}{\partial r^2} + \frac{\partial^2 q_c}{\partial z^2} + k_{\text{eff}}^2 q_c = 0, \quad (\text{E.1})$$

where the quantity q_c is related to the complex pressure via $q_c = p_c \sqrt{r}$ and $k_{\text{eff}} = w/c_{\text{eff}}$.

The solution of equation E.2 is written in the form of

$$q(r, z) = \psi(r, z) \exp(ik_a r), \quad (\text{E.2})$$

where k_a is the wave number at the ground surface. As r increases, the factor $\exp(ik_a r)$ oscillates rapidly, resembling a plane wave moving in the positive r direction. However, the function $\psi(r, z)$ changes slowly as r increases.

Substituting equation E.2 into equation E.1 gives [13]

$$\frac{\partial^2 \psi}{\partial r^2} + 2ik_a \frac{\partial \psi}{\partial r} + \frac{\partial^2 \psi}{\partial z^2} + (k_{\text{eff}}^2 - k_a^2) \psi = 0 \quad (\text{E.3})$$

The variable ψ usually varies slowly with r , thus we neglect the second derivative obtaining

$$2ik_a \frac{\partial \psi}{\partial r} + \frac{\partial^2 \psi}{\partial z^2} + (k_{\text{eff}}^2 - k_a^2) \psi = 0, \quad (\text{E.4})$$

where ψ is a function depending on r and z . This equation is only valid for elevation angles up to approximately 10° [13]. By using a slightly different derivation, a parabolic equation that is valid for larger elevation angles can also be derived. Very large elevation angles still remain a limitation.

E.2 What is a parabolic equation?

Differential equations can be a challenge to solve, and the way to solve them is dependent on the type of differential equation. Consider the most general form of a partial differential equation [68]

$$L(u) = a_{ij} \frac{\partial^2 u}{\partial x_i \partial x_j} + b_i \frac{\partial u}{\partial x_i} + cu = r(x_1, x_2, \dots, x_n) \quad (\text{E.5})$$

It turns out that the character of the PDE is determined by its highest derivative such that the coefficient a_{ij} is the one that should be looked at. The character is determined by the eigenvalues of the coefficient matrix a_{ij} . With these eigenvalues three categories of PDE's can be distinguished:

- Elliptic: $\lambda_i \neq 0 \forall i$, and all λ_i 's have the same sign.
- Hyperbolic: $\lambda_i \neq 0 \forall i$, and the sign of one eigenvalue differs from the others.
- Parabolic: One zero eigenvalue, all other $\lambda_i \neq 0$ and the same sign.

In order to characterize this PDE we look at the highest derivative. For equation E.4 this result in coefficient matrix:

$$A = \begin{pmatrix} 1 & 0 \\ 0 & 0 \end{pmatrix} \quad (\text{E.6})$$

It is trivial to see that for this matrix the eigenvalues are 0 and 1, implicating that it is a parabolic equation.

E.3 General approach of the parabolic equation method

In the previous part, it was shown that the Helmholtz equation can be transformed into a parabolic equation. Thus, solving this parabolic equation is an approximation of the wave equation in the frequency domain. The computation of a whole frequency spectrum requires the computation of every single frequency in the spectrum. An assumption that is often used is the axisymmetric approximation (this was also done in Appendix E.1). By using the axisymmetric approximation, variations that correspond with a variation in azimuth angle are neglected.

The parabolic equation is solved in a rectangular grid, in the vertical rz plane. The horizontal spacing is dr and the vertical spacing is dz . The grid has a finite height, to eliminate reflection from the top of the grid, an absorbing layer is placed at the top of the grid as a boundary condition. The boundary condition for the ground is a complex impedance depending on the type of ground surface. The source is described by a starting function of complex pressure. This starting function is extrapolated over the whole grid in the positive r direction.

Two widely used methods for the extrapolation are the Crank-Nicolson Parabolic Equation (CNPE) method and the Green function Parabolic Equation (GFPE) method. The CNPE method is slightly more accurate in situations with large elevation angles and large sound speed gradients, but the GFPE method can use a coarser grid and is therefore faster [13].

E.3.1 Advantages and limitations of the parabolic equation method

The PE method can obtain accurate results for a non-layered atmosphere with a non-homogeneous ground surface. Also, the effect of turbulence can be included in the PE method. This makes the method widely applicable to a large variety of situations.

Three limitations can be identified by looking at Appendix E.1. First of all, the parabolic equation is not valid for large elevation angles. Also in the derivation of the parabolic equation, the effective sound speed approximation is used for the description of a moving medium (see the k_{eff} term in equation E.1). This imposes a constraint on the elevation angle as well (see section 2.3.1). Finally, consider equation E.2 again. With this equation, the solution is written only in terms of a forward-traveling wave, neglecting potential back scattering. Back scattering can often be neglected, but when a barrier is present near the source, the energy reflected back should be taken into account.

The use of the PE method usually requires a large computational cost. All frequencies in the spectrum have to be computed, and the computational cost increases with increasing frequency and problem size. In the case of wind turbine noise, this can computational cost can be considerable, which makes use for 3D situations not feasible.

E.4 Green functions parabolic equation(GFPE)

The GFPE method is often used for atmospheric sound propagation, because of a decrease in computational time with respect to the CNPE method. Gilbert and Di [28] developed the formulation of the

Green's functions parabolic equation for a step in the r direction as

$$\begin{aligned} \psi(r + dr) = & e^{\left(\frac{i dr (\delta k)^2}{2k_0}\right)} \left(F^{-1} \left[\left(\tilde{\psi}(r, k') + R(k') \tilde{\psi}(r, -k') \right) e^{i dr (\sqrt{k_0^2 - k'^2} - k_0)} \right] \right. \\ & \left. + 2i\beta \tilde{\psi}(r, \beta) e^{i dr (\sqrt{k_0^2 - \beta^2} - k_0)} e^{-i\beta z} \right) \end{aligned} \quad (\text{E.7})$$

where k is a wavenumber dependent on range and height, and ψ is the pressure with the cylindrical spreading removed. $\beta = \frac{k_0}{Z_g}$ is the surface wave pole, Z_g is the normalized ground impedance, $R(k)$ is the plane-wave reflection coefficient, and $\tilde{\psi}$ is the spatial Fourier transform of ψ . The inverse Fourier transform is indicated by F^{-1} . The three terms in equation E.7, represent the direct wave $(\tilde{\psi}(r, k') e^{i dr (\sqrt{k_0^2 - k'^2} - k_0)})$, the specular reflected wave $(R(k') \tilde{\psi}(r, -k') e^{i dr (\sqrt{k_0^2 - k'^2} - k_0)})$ and the surface wave $(2i\beta \tilde{\psi}(r, \beta) e^{i dr (\sqrt{k_0^2 - \beta^2} - k_0)} e^{-i\beta z})$.

E.5 ATMOS

ATMOS is an in-house code of the CTSB which uses the GFPE method to compute the sound field. The method is developed to also incorporate back scattering problems and had been verified with numerous examples [69]. In this report ATMOS is used as a reference tool to verify the results of Harmonoise.

E.5.1 Parameters

To do accurate computations with the GFPE method, appropriate parameter selection is important. Important parameters are the extrapolation steps dz and dr but also the maximum range r_{max} , the attenuation layer height Z_{attn} and the attenuation layer thickness A . The relationship among these parameters is not well understood [70]. For example, in the case of a constant sound speed, dr could be large. However, making dr large requires shifting the other parameters as well. The dz has to be small to correctly capture the vertical oscillation in the pressure field due to interference from the direct and reflected paths. Also, the surface wave can oscillate quickly.

Salomons [13] proposes as a rule of thumb to use about 10 samples per wavelength in the dz direction but the dr direction could be up to 0.02 samples per wavelength (note that this implies that a finer grid is necessary with higher frequency). However, this is not a guarantee of success for all cases.

Appendix F

Conformal mapping

A conformal map is a function that locally preserves angles but not necessarily lengths. Conformal maps can be used to solve problems where the geometry is inconvenient by mapping the geometry into a more convenient one. In the case of the Harmonoise model, it is used to transform the problem of refracting rays into a more convenient problem with only straight rays.

To explain conformal mapping, consider two curves $\gamma_1(t)$ and $\gamma_2(t)$ that intersect at point z_0 . The angle between the curves at point z_0 can be found by computing the tangent vector of the curves at point z_0 , which are defined as $\gamma_1'(t_0)$ and $\gamma_2'(t_0)$. These curves are mapped by the following function

$$w = f(z) \tag{F.1}$$

where $f(z)$ is a mapping function that, for example, converts the point z_0 to the point w_0 . Figure F.1 depicts this case.

In the figure, the two tangent vectors are scaled and rotated by the same amount. The rotation and scale factor can be local, meaning that at another point, they might be different. The angle between the two transformed tangent vectors is the same as the angle between the tangent vectors before the transformation. Conservation of angles is a key property in conformal mapping.

A mapping function consists of (a combination) of four different transformations:

- translation: $F(z) = z + b$
- rotation: $F(z) = e^{iaz}$
- magnification: $F(z) = 2z$
- inversion: $F(z) = 1/z$

Important properties of inversion are the following [2]:

- Any line not through the origin is mapped to a circle through the origin

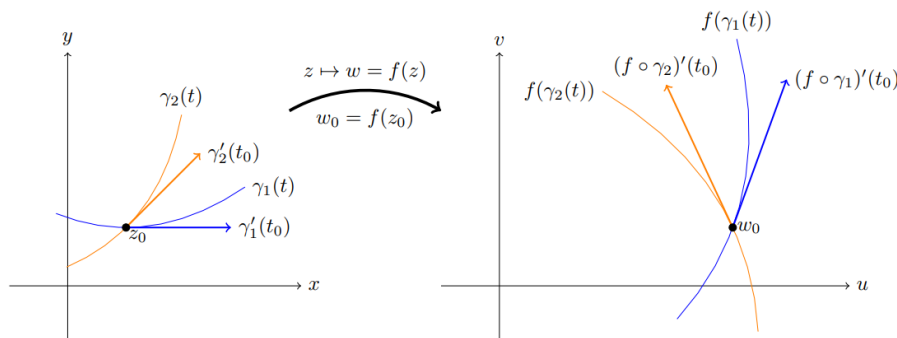


Figure F.1: Illustration of the conformal mapping of two curves. Figure taken from [2]

- Any line through the origin is mapped to a line through the origin
- Any circle not through the origin is mapped to a circle not through the origin
- Any circle through the origin is mapped to a line not through the origin

Thus, inversion maps lines and circles to lines and circles. This property is important and can be used to map circular ray paths into straight lines.

A well-known type of conformal mapping is called fractional linear transformations, which are also known as Mobius transforms. These transforms have functions in the form of

$$T(z) = \frac{az + b}{cz + d}, \tag{F.2}$$

where a, b, c, d are complex constants and $ad - bc \neq 0$. The functions map the complex plane onto itself, meaning that the input is a complex number and a complex number is returned. The value of a, b, c , and d determines the behavior of the mapping and should be chosen to fit the desired properties.